ATOMISTIC SIMULATIONS OF BONDING, THERMODYNAMICS, AND SURFACE PASSIVATION IN NANOSCALE SOLID PROPELLANT MATERIALS

A Dissertation

by

KRISTEN SMITH WILLIAMS

Submitted to the Office of Graduate Studies of
Texas A&M University
in partial fulfillment of the requirements for the degree of

DOCTOR OF PHILOSOPHY

August 2012

Major Subject: Materials Science and Engineering

Atomistic Simulations of Bonding, Thermodynamics, and Surface Passivation in Nanoscale Solid Propellant Materials

Copyright 2012 Kristen Smith Williams

ATOMISTIC SIMULATIONS OF BONDING, THERMODYNAMICS, AND SURFACE PASSIVATION IN NANOSCALE SOLID PROPELLANT MATERIALS

A Dissertation

by

KRISTEN SMITH WILLIAMS

Submitted to the Office of Graduate Studies of
Texas A&M University
in partial fulfillment of the requirements for the degree of

DOCTOR OF PHILOSOPHY

Approved by:

Chair of Committee,	Tahir Cagin
Committee Members,	Raymundo Arroyave
	Eric Petersen
	Joseph Ross
	Jairo Sinova
Interdisciplinary Chair,	Ibrahim Karaman

August 2012

Major Subject: Materials Science and Engineering

ABSTRACT

Atomistic Simulations of Bonding, Thermodynamics, and Surface Passivation in Nanoscale Solid Propellant Materials. (August 2012)
Kristen Smith Williams, B.S, Jacksonville State University
Chair of Advisory Committee: Dr. Tahir Cagin

Engineering new solid propellant materials requires optimization of several factors, to include energy density, burn rate, sensitivity, and environmental impact. Equally important is the need for materials that will maintain their mechanical properties and thermal stability during long periods of storage. The nanoscale materials considered in this dissertation are proposed metal additives that may enhance energy density and improve combustion in a composite rocket motor. Density Functional Theory methods are used to determine cluster geometries, bond strengths, and energy densities.

The ground-state geometries and electron affinities (EAs) for $Mn_xO_y^-$: $x = 3, 4, y = 1, 2$ clusters were calculated with GGA, and estimates for the vertical detachment energies compare well with experimental results. It was found that the presence of oxygen influences the overall cluster moment and spin configuration, stabilizing ferrimagnetic and antiferromagnetic isomers. The calculated EAs range from 1.29-1.84 eV, which is considerably lower than the 3.0-5.0 eV EAs characteristic of current propellant oxidizers. Their use as solid propellant additives is limited.

The structures and bonding of a range of Al-cyclopentadienyl cluster compounds were studied with multilayer quantum mechanics/molecular mechanics (QM:MM) methods. The organometallic Al-ligand bonds are generally 55-85 kcal/mol and are much stronger than Al-Al interactions. This suggests that thermal decomposition in these clusters will proceed via the loss of surface metal-ligand units. The energy

density of the large clusters is calculated to be nearly 60% that of pure aluminum. These organometallic cluster systems may provide a route to extremely rapid Al combustion in solid rocket motors.

Lastly, the properties of COOH-terminated passivating agents were modeled with the GPW method. It is confirmed that fluorinated polymers bind to both Al(111) and Al(100) at two Al surface sites. The oligomers HCOOH, CH_3CH_2COOH, and CF_3CF_2COOH chemisorb onto Al(111) with adsorption energies of 10-45 kcal/mol. The preferred contact angle for the organic chains is 65-85°, and adsorption energy weakens slightly with increasing chain length. Despite their relatively weak adsorption energies, fluorinated polymers have elevated melting temperatures, making them good passivation materials for micron-scale Al fuel particles.

DEDICATION

To my dearest husband, I am blessed to have shared this journey with you.

ACKNOWLEDGMENTS

There are many who have been instrumental in my academic journey, thus far. I owe my gratitude firstly to my committee chair and adviser, Prof. Tahir Cagin for many years of patience and guidance. He has challenged me with different projects, sent me to conferences, and helped me develop my research skills. I would like to thank the members of my graduate advisory committee for their time in reading and marking this dissertation and for conducting my final exam. Members' feedback from the Ph.D. candidacy exam was particularly helpful in identifying deficiencies and defining the broader scope and impact of the work. This dissertation would not have been possible without Prof. Joe Hooper. He suggested materials to read, answered technical questions, and co-authored several key papers. Parts of the dissertation work were completed at the Naval Warfare Center–Indian Head, MD, during internships sponsored by the Office of Naval Research. Finally, the experimental spectroscopy data in Chapter 5 was supplied by Kit Bowen at Johns Hopkins.

I acknowledge the National Science Foundation IGERT program and the Department of Defense STEP Program, both of which supported me at different phases in my graduate studies. I will always be grateful to my undergraduate mentors: Profs. Jan Gryko, Nouredine Zettili, and Carl Gagliardi, each of whom contributed to my early development as a researcher and influenced my decision to pursue graduate studies. Special thanks to Jan Gerston for academic advisement and motivational support. My time in graduate school has been enriched by worshipping at Covenant Presbyterian Church, a caring family of faith who have provided friendship and constant moral support. I am grateful for the support of my parents, Tim and Sally Smith, who always encouraged me to set high goals and inspired me in childhood with many trips to the rocket museum. Most of all, I would like to thank my husband, Matt Williams, who has spent many late nights alone with our children, Sarah and Corbin.

NOMENCLATURE

AFM	Antiferromagnetic
Al_2O_3	Aluminum oxide, or alumina
AP	Ammonium perchlorate
DFT	Density Functional Theory
CAD/PAD	cartridge-activated device/propellant-activated device
CDA	Charge decomposition analysis
CMDB	composite-modified double-base propellant
CO	carbon monoxide
CO_2	carbon dioxide
Cp	cyclopentadienyl, C_5H_5
Cp^*	pentamethyl-cyclopentadienyl, $C_5[CH_3]_5$
DDT	Deflagration-to-detonation transition
EA	Electron affinity
EDA	Energy decomposition analysis
eta- (η-)	Hapticity
fM	Ferrimagnetic
FM	Ferromagnetic
g	Gravity of earth; 9.81 m/s^2 or 32.2 ft/s^2
GGA	Generalized gradient approximation
GPW	Gaussian plane wave method
GTO	Gaussian type orbital
HEDM	High-energy-density material
HOF	Heat of formation
HOMO	Highest occupied molecular orbital
H_2O	water
I_{sp}	Specific impulse

LDA	Local density approximation
LUMO	Lowest unoccupied molecular orbital
M	Multiplicity, $M = S + 1$
NBO	Natural bond order
NO	nitric oxide
NO_2	nitrogen dioxide
PES	photoelectron spectroscopy
psi	pounds per square inch, or lb/in^2
QM:MM	Quantum mechanics/molecular mechanics
R	Molar gas constant; 8.314 $J/k \cdot mol$
S	Net cluster spin moment
SAM	Self-assembled monolayer
SCF	Self-consistent Field
STO	Slater type orbital
STP	Standard Temperature and Pressure
TD-DFT	Time-dependent DFT
TNT	trinitrotoluene
UFF	Universal force field
VDE	Vertical detachment energy

GLOSSARY

Action time	The total burning time or time over which a rocket motor produces thrust
Blasting gelatin	Nitroglycerin mixed with 8% nitrocotton
Ballistite	60/40 mix of nitroglycerine/nitrocellulose. Invented by Alfred Nobel in 1887
CMDB	Double-base propellant modified by the addition of AP and Al
Cordite	Smokeless propellant made from nitrocellulose, nitroglycerine, and petroleum jelly extruded into cords; first produced in the United Kingdom in 1889
Critical diameter	Minimum diameter required for propagation of a stable detonation wave
Detonation	Supersonic explosive reaction that propagates a shockwave through the material; Propagation of a detonation wave is sustained by accompanied chemical reactions that release large amounts of energy
Dynamite	Nitroglycerine adsorbed in kieselguhr, a soft, sedimentary rock that is easily crumbled into powder
Energetic	Possessing large amounts of stored chemical energy
Free-standing	Composite propellant grain containing a thermoplastic binder and a firm structure
Fume off	Uncontrollable evolution of large quantities of gas and heat from an energetic material
Functional	A mathematical function whose argument is also a function
Grain	Final product of a solid propellant in its mixed state; processed to the desired shape via casting or extrusion

Hapticity	Measure of the number of ligand atoms participating in a central metal-ligand bond (e.g. one Fe atom bound equidistant to a phenyl ring would have η-6 hapticity)
Isomags	Magnetic or spin isomers with comparable binding energies and identical spins but different distributions of local moments
Mesa effect	Characteristic of certain propellant additives in which burn rate decreases with increasing pressure
Oxygen balance	Measure of a compound's ability to fully oxidize hydrocarbon fuel; a positive oxygen balance produces combustion products of H_2O (in the form of steam) and CO_2, with excess oxygen reacting to form NO; a negative oxygen balance indicates insufficient oxygen content, and the gaseous combustion products are H_2 and CO; perfect oxygen balance is preferable because it ensures non-toxic combustion products or fumes
Specific impulse	Pounds of thrust generated by a rocket motor when 1 pound of propellant is burned in 1 second; given by the equation $I_{sp} = F/(dm/dt)$
STP	Standard temperature and pressure; 273 K (0° Celsius) and 1 atm pressure
Thixotropic	The property exhibited by certain gels of becoming fluid when stirred or shaken and returning to the semisolid state upon standing
VDE	The energy required to excite one electron from a state with principal quantum number n to state $n \pm 1$, with no change in the azimuthal (l), magnetic (m_l) or spin projection (m_s) quantum numbers
Web thickness	Distance between the internal burning surface and outer

	periphery of a propellant grain; burning rate equals web thickness divided by action time
Worm-holing	Propellant failure mechanism caused by radiation-induced ignition of fuel particles below the grain surface

TABLE OF CONTENTS

Page

Page

LIST OF TABLES

TABLE Page

TABLE Page

LIST OF FIGURES

FIGURE Page

FIGURE Page

FIGURE Page

1. INTRODUCTION

Solid propellants are one class of energetic materials whose primary use is imparting motion to an object; applications include small firearms, cannons, missiles, and solid rocket motors. The performance of a solid propellant is a complex, multiscale problem because combustion is influenced by grain geometry, composite mix ratio, and chemistry of the individual components. Engineering new propellants requires optimization of several factors. For example, The National Research Council has highlighted the need for "energetic materials that are insensitive (i.e., resistant to accidental explosion) and that offer higher energy densities and the ability to tailor energy release for different uses."[1] Nanotechnology for energetics has been identified as a key research area; in nanocomposites, for example, nanoparticle size, morphology, and surface chemistry are just a few of the important factors in determining how the energetic material will perform in a real-world application.

As an example, passivated nanoscale Al-based clusters may be promising novel propellant additives. Similar materials, such as nanoscale aluminum powders, have been extensively studied for these applications.[1] The justification is that smaller dimension aluminum leads to enhanced rates of combustion. However, aluminum powders are extremely air-sensitive and will oxidize rapidly, creating oxide shells that inhibit full consumption of the metallic fuel. A different approach is organic passivation of the nanoscale aluminum metal that both protects from unwanted oxidation and enhances the rate of combustion.

The nanoscale materials considered in this dissertation are proposed metal additives that will enhance energy density and improve combustion in a composite rocket motor. First-principles methods are used to estimate bonding strength, heats of formation and combustion, and energy densities of nanoscale oxidizers and

This dissertation follows the style of *The Journal of Chemical Physics*.

fuel additives. The goal is to expound on previous computational work, while also providing insight that will guide future synthetic chemistry efforts related to new propellant materials.

The benefit of using a theoretical approach is the "improved ability to predict and select new materials," in particular, those with "extreme properties" that would be costly or unsafe to study in a laboratory setting.[1] A disadvantage of theory is the dubious prediction of stable nanoclusters which are neither easily synthesized nor well-suited for use in a composite. For example, first-principles results on an isolated nanocluster cannot predict its miscibility, diffusion, grain boundary effects or other properties related to the mixing process. With these limitations in mind, this dissertation evaluates potential propellant materials by comparing their calculated properties with those of other commonly-used propellant materials. The specific materials studied were metallic nanoclusters composed of manganese or aluminum, and the primary issues addressed were cluster geometry and bonding, accurate thermodynamics, and surface passivation.

The remainder of this dissertation is structured as follows: Chapter 2 provides background information on solid propellants following the discussions by Warren,[2] Taylor,[3] and Hartman and Morrow.[4] This chapter also includes a brief description of propellant ignition and combustion, drawing from the works of Glassman,[5,6] Vilyunov and Zarko,[7] and, most recently, Beckstead.[8,9] Chapter 3 contains a literature review of the studied materials, discusses issues related to nanoscale propellant additives, and provides motivation for the proposed dissertation project. Chapter 4 outlines the computational methodology used in the dissertation research, and Chapters 5-7 contain all research results. Finally, Chapter 8 summarizes the most important findings of the dissertation project and connects these findings with engineering design principles for future propellant materials.

2. BACKGROUND

2.1 Energetic Materials

Energetic materials include explosives, propellants and pyrotechnics. Propellants are used for three primary tasks: firing a projectile from a gun at high velocity (i.e., canons, firearms, etc.), powering a rocket motor, or generating gas for actuation of a mechanical device (CAD/PAD). The latter are employed in launching torpedos, starters for airplane engines, submarine guns, pilot ejection systems, fire extinguishers, car jacks, and life jackets. Pyrotechnics are used in fireworks, incendiary devices, smoke screens, and flares. Propellants are classified as "energetic" because they have large amounts of stored chemical energy which, once released can be used to do mechanical work. Energetic materials can be solid-phase mixtures or singular energetic compounds, such as trinitrotoluene (TNT).

In addition to chemical energy, another defining characteristic of energetic materials is thermal stability. Ideally, the energetic parent compound should have a large, positive ΔE compared with its decomposition products, and the molecule must exist in a metastable state with a high activation energy of initiation. This activation barrier must be large at ambient conditions and crossed only by the application of heat or an appropriate catalyst. Weakening of the activation barrier under normal aging conditions is therefore one factor related to long-term stability of an energetic material. The thermal stability of an energetic material can be quantified by measuring loss of weight, evolution of gas (e.g. NO_2) or changes in acidity or composition versus temperature (or time, if long-term storage is important).

The chemical energy in an energetic material is released either through deflagration (burning) or detonation. Deflagration is the rapid thermal decomposition of material at or above its surface. As a material deflagrates, heat is conducted from the flame front back to the surface, causing the combustion reaction to self-propagate. The typical velocity of combustion normal to the reacting surface is $\approx$ 1-2 cm/sec.

Detonation, however, is decomposition of a high explosive that causes a detonation wave to propagate through the material at a speed of $\approx$ 5-10 km/s. Hence, the primary difference between propellants and explosives is the rate of energy release. Under certain conditions, propellants will detonate (deflagration-to-detonation transition, or DDT), but they have critical diameters on the order of 5 feet, which is quite large compared to that of an explosive, which can be less than one centimeter. DDT is undesirable because propellants are generally designed to burn slowly. This slow burn produces very hot gases that pressurize the combustion chamber and, when released through a nozzle, cause the thrust that propels the rocket forward. This application demands that deflagration be controlled, repeatable, and predictable.

Propellants and explosives contain similar ingredients with comparable amounts of stored chemical energy. In both types of materials, oxidizer and fuel can be present within a single molecule or premixed in a composite formulation. Hence, the true distinction between propellants and explosives is kinetic (how the reaction is initiated) rather than thermodynamic (how much energy is released). Deflagration and detonation are both self-sustained, exothermic reactions which are initiated by local application of energy, i.e. heat or mechanical impact. Under standard conditions of temperature and pressure, thermal ignition can be achieved by chemical reaction, flame, friction or an electrically-heated wire. Deflagration is most often initiated by thermal means, but detonation requires a physical blow or shock, which can be supplied on cue by a detonator. This device contains an initiator material, such as mercury fulminate, lead azide, lead styphnate or tetrazine. Initiation can also occur by hot spots in the material, which are produced by adiabatic compression of small air pockets. Once initiated, explosive reactions are driven by large free energy of the molecule, rapidity of the energy release, and accelerating effects of the decomposition products. Explosive reactions can therefore be autocatalytic, especially when nitric acid is produced. This can be undesirable if an auto-catalyzed reaction leads to "fume off," where large quantities of gas and heat are evolved uncontrollably. A

common preventative tool is addition of a stabilizer which reacts with nitric acid. More about stabilizers is discussed in §2.2.2.

Combustion consumes propellant at a pressure of $P \approx 300 - 5000$ psi, while doing little more than scorching the surrounding material (i.e. the rocket motor casing is not destroyed). Detonation, on the other hand, generates a shock wave at typical peak pressures up to 725 psi, which does considerably more damage. In consideration of the differences between propellants and explosives—reaction velocities and pressures, and initiation mechanisms—Taylor[3] appropriately refers to propellants as "low explosives."

The combustion process which takes place in a rocket motor cannot extract oxygen from the air, as occurs in combustion engines. Hence, solid propellant systems must carry their own source of oxygen. This adds mass to the composition, thereby reducing the inherent amount of fuel and the resulting energy output. While the energy production of solid propellants is lower than that of open-air combustion processes, propellants are well-suited for providing high power at short intervals and for use in environments with little or no atmospheric oxygen. All gases needed for propulsion are produced within the rocket motor; solid propellants can therefore be employed in space, at high altitudes or under water. The combustion of a solid propellant releases large amounts of gas at high pressure and temperature, gas which can do work via expansion. Hence, the most important characteristics of a propellant formulation are the amount of heat liberated, the temperature of the combustion reaction, the volume of gas produced, and the oxygen balance (dictates which gases are produced and their relative amounts).

2.2 Solid Propellants

2.2.1 History

The earliest recorded use of propellants was by the Chinese in the seventh century.[7] The oldest modern propellant is gunpowder or black powder, which is a mixture of charcoal, sulfur, and potassium nitrate. Gunpowder was known to the ancient Chinese, Hindu, and Arab civilizations, and its use in Europe was first documented in the early fourteenth century. In addition to its use as a propellant, gunpowder has also been used in blasting explosives, ignition delays, land mines, and building demolition. Gunpowder has a specific impulse, I_{sp} of 40-80 seconds, which is low compared with the $I_{sp} > 200$ seconds of modern compositions. Nitrocellulose, or guncotton was introduced by Vieille in 1886; it is made by nitrating cellulose fibers (e.g., soaking in nitric acid) to a concentration of 11-14% nitrogen. Nitrocellulose with nitrogen content less than 12% is called colloxylin, while that with more than 12% nitrogen is called pyroxylin. Alfred Nobel invented the first double-base propellant—which he called ballistite—by dissolving nitroglycerin into guncotton.[1] For rocketry applications, gunpowder and guncotton were superseded by cordite during World War II.

2.2.2 Standard Formulations

Modern propellants are classified into two main types: homogeneous and composite. Nitrocellulose-based propellants are examples of homogenous monopropellants in which a single material contains both the oxidizer and fuel needed for combustion. Homogenous propellants are often referred to as colloidal propellants because of the molecular structure of nitrocellulose. These propellants can be formulated with or

[1]In addition to this, Alfred Nobel made other significant contributions to the class of energetic materials. He invented dynamite and blasting gelatin and discovered mercury fulminate, the first initiator material.[3]

TABLE 2.1. Typical homogenous propellant ingredients. Adapted from Ref. 2.

Material	% Composition
basic ingredients	50-99
stabilizers	1-2
plasticizers	0-50
darkening agents	0-0.2
ballistic agents	0-3
other additives	0-2
solvents	0-40

without a solvent, and the final product is referred to as the propellant "grain." Since removal of the solvent is more difficult for large grains, solvent-less propellants are more common in large missiles. Homogeneous propellants can contain multiple combustible ingredients; single-, double-, and triple-base formulations contain one, two, and three energetic materials, respectively. Cordite is an example of a homogeneous, double-base propellant composed of nitrocellulose, nitroglycerin, and petroleum jelly. Table 2.1 lists the common ingredients and percent compositions for typical homogenous solid propellants.

Thermal decomposition of nitrocellulose begins with breaking of the O-NO_2 bond in the nitric ester groups. This process has an activation energy of only 45 kcal/mol, and the released NO_2 groups can further react, releasing heat that leads to self-accelerating ignition. Hence, the decomposition of nitrocellulose is unavoidable, especially at elevated temperatures. Stabilizers are chemical ingredients which are added to extend service life; they can retard nitrocellulose destruction by reacting with the nitric oxide decomposition products. The best stabilizers are therefore nitric oxide absorbers, alkaline substances (such as soda ash), and drying agents. The latter two promote alkalinity and dryness, which enhance thermal stability. A common additive to catalyze ignition is ferrous oxide (FeO). Plasticizers are frequently added

to improve mechanical properties and facilitate the extrusion process. Nitroglycerin, for example, is a commonly-used explosive plasticizer. Darkening agents, such as carbon black, are added to prevent "worm-holing," a failure mechanism caused by radiation-induced ignition of fuel particles below the grain surface. Ballistic agents and other additives are often used to improve performance related to burning and smoke production. In general, additives are used to improve physical properties, modify burn rate, assist in manufacturing, enhance stability during storage, suppress exhaust flash or inhibit ignition in sub-surface layers of the grain.

Homogenous propellants take on the physical characteristics of their base materials and are generally thermoplastics. They can be processed into a number of different grain shapes via extrusion, solvent casting or slurry casting. The former method requires the use of a solvent or high temperature to keep the material mechanically pliable. This is how discrete double-base charges are extruded into cord shapes (hence the name Cordite). In the casting process, however, a mould is filled with nitrocellulose powder and a nitroglycerine mixture is slowly added. The powder swells and gelatinizes with applied heat. Slurry casting involves thixotropic mixtures that contain large amounts of solid ingredients.

Composite propellants are heterogenous mixtures (black powder is one example) in which the fuel and oxidizer are separate solid phases. The oxidizer is often a finely-ground inorganic crystal which is held together with a polymer binder. A typical composite propellant contains 65-88% oxidizer, 8-14% binder, and up to 5-22% additives; these types of formulations are primary candidates for the nano-additives considered in this dissertation work. The oxidizer drives combustion, while the binder—some type of plastic, resinous, or elastomeric hydrocarbon—serves as fuel. A very common additive in composite propellants is aluminum powder, which has a high heat of oxidation, serves as added fuel and improves burning characteristics. The heats of reaction for aluminum with various oxidizing agents are listed

TABLE 2.2. Heats of reaction for aluminum with various oxidizing agents. Adapted from Ref. 3.

Reactants	ΔH_{rxn}(cal/g)
Al + O_2	7000
Al + $KClO_4$	2400
Al + KNO_3	1800
Al + Fe_3O_4	800

in Table 2.2. Clearly, solid oxidizers reacting with aluminum do not release as much energy as oxidation with air.

Some common binders used in propellants are polystyrene, hydroxyl-terminated polybutadiene (HTPB), vinyl polymers, asphalt, and even nitrocellulose. These polymers have good mechanical properties at low temperature and resist flow at high temperatures. Since the mechanical properties of a polymer are determined by structure and concentration of the repeat unit and crosslink density, both thermoplastics and elastomers make suitable binders. The former gives the propellant grain a firm structure; such grains are said to be "free-standing," and can be extruded into almost any desired shape. Elastomeric binders, on the other hand, are better suited for formulations that will be cast directly into the motor casing. Furthermore, case-bondable propellant compositions must be either plastic or elastic over the whole operating temperature range. This is because motor casings are typically made of steel, which has a lower coefficient of thermal expansion. Otherwise, under temperature variation, stress between the steel casing and the charge would cause the grain to crack or separate. Double-base propellants are unique in that the nitrocellulose chains do not crosslink. Hence, their mechanical strength depends on the concentration and rigidity of the nitrocellulose fibers.

While the physical properties of composite propellants are largely determined by the binder, the combustion properties are directly related to the chosen oxidizer. As

the name suggests, oxidizers provide oxygen (or halogens) which readily burns the fuel in a rocket motor according to the simplest combustion reaction:

$$\text{fuel} + \text{O}_2 \longrightarrow \text{H}_2\text{O} + \text{CO}_2 + \Delta H_\text{c}. \tag{2.1}$$

Materials which can serve as oxidizers include nitrates, chlorates, perchlorates, permanganates, chromates, peroxides, and metallic oxides. The most common oxidizers are potassium perchlorate, $KClO_4$, ammonium perchlorate, NH_4ClO_4, and ammonium nitrate, NH_4NO_3. Each of these materials gives a different burn rate, flame temperature, and level of smoke production, and the oxidizer/binder formulation is usually chosen to maximize desired (minimize undesired) combustion properties. Metallic oxidizing agents, such as Fe_3O_4, TiO_2 or MnO_2, do not produce very high heats of reaction (see Table 2.2) but are advantageous for some applications because they do not produce N- or Cl-containing gases upon combustion.

The three most common oxidizers have unique advantages and disadvantages. Ammonium nitrate gives longer burn times and produces no smoke or toxic combustion products, making it especially useful in safety compositions for blasting in coal mines where methane often mixes with air. It is also fairly inexpensive and readily available due to high demand from the agricultural industry. Disadvantages of this material are its low oxidation potential and its five metastable crystalline forms. Specifically, ammonium nitrate undergoes a solid-state phase change at 89.8°F (≈ 32°C). The accompanied expansion in volume is large enough to crack the grain, leading to non-uniform burning. This is a common failure mechanism for NH_4NO_3-based composite propellants in long-term storage.

Potassium perchlorate has a much higher oxidation potential than ammonium nitrate and is nonhygroscopic. Nevertheless, its use as an oxidizer is limited due to its toxic and corrosive Cl-containing combustion products. In addition, the smoke generated from burning $KClO_4$-based composite propellants is heavy in hydrochloric acid particulates. Ammonium perchlorate, however, produces no smoke and, despite

its low oxidation potential, generally out-performs both potassium perchlorate and ammonium nitrate.

Clearly, intelligent propellant design requires achieving the proper balance of fuel and oxidizer to provide the necessary burn characteristics. Some important considerations for new formulations include physical properties of the polymer binder, composition (relative amount of each component), and thermal diffusivity of the product material.

2.2.3 Propellant Ignition and Combustion

Ignition in solid propellants is defined by two steps: (1) the initiation of chemical reactions in the material combined with (2) the beginning of the combustion process. Prior to ignition, the propellant exists in some initial, non-reacting state; after successful ignition, steady-state combustion proceeds unquenched until all available fuel is spent. This complex physical-chemical process depends on the kinetic barrier of initiating chemical reactions, flame propagation across the propellant surface, inhomogeneity of the thermal field, and the dynamics of gas flow over the surface. Furthermore, the conversion from ignition to developed combustion depends on the radiant flux (applied heat) and length of time of radiant heating. Simply applying a stronger external stimulus is not adequate because excessive heat may simply scorch the material without leading to proper combustion.

The first step of ignition requires breaking the conditions of thermal equilibrium in the surface layer. Under the influence of an external stimulus (i.e., heat source), exothermic chemical reactions occur on the surface which self-accelerate until thermal equilibrium is destroyed. The chemical kinetics of the reactions that lead to ignition are complex, depending on heat and mass transfer and the intensity of the external stimuli. Classical thermal ignition theory states that thermal equilibrium in the surface will be broken (and ignition will occur) when the heat generated due to chemical reactions equals that lost due to thermal transport.

If ignition is associated with more than one competing chemical reaction—and the reaction rates between them differ by at least two orders of magnitude—the criteria for ignition will be determined by the fastest reaction, i.e., the one with the highest reaction rate. In aluminum particles, for example, complete combustion of all available fuel is limited by a growing shell of metal oxide. This is unavoidable because surface oxidation of unpassivated aluminum particles is highly exothermic and will occur at temperatures well below T_{ig}. Vilyunov and Zarko[7] describe the growth rate of the oxide layer by an Arrhenius law of the form

$$k_{\mathrm{ox}} = \frac{d\delta}{dt} = \frac{z}{\delta} e^{(-E_{\mathrm{ox}}/RT)}, \tag{2.2}$$

where δ is the thickness of the oxide film, E_{ox} is the activation energy for metal oxidation, and z is a constant prefactor. The oxidizing agent (usually atomic oxygen) is simultaneously transported to the metal surface by either molecular or convective diffusion through alumina. The changing concentration of oxygen, ϕ through the alumina shell is described by Fick's second law:

$$\frac{d\phi}{dt} = D \frac{\partial^2 \phi}{\partial x^2}, \tag{2.3}$$

where the diffusion coefficient, D also follows an Arrhenius law,

$$D = D_0 e^{(-E_{\mathrm{D}}/RT)}. \tag{2.4}$$

The controlling factor in Al particle ignition is therefore the relative magnitudes of k_{ox} and D. According to the principle of equiaccesible surfaces,[7] an effective rate constant to describe the two-factor process in Al ignition would be

$$k_{\mathrm{eff}} = \frac{k_{\mathrm{ox}} D}{k_{\mathrm{ox}} + D}. \tag{2.5}$$

In the kinetic domain, diffusion of oxidizer occurs more rapidly than oxide growth (D$\gg k_{\mathrm{ox}}$) and $k_{\mathrm{eff}} = k_{\mathrm{ox}}$. In the opposite case (when D$\ll k_{\mathrm{ox}}$), the effective reaction rate is controlled by the rate of oxygen diffusion, $k_{\mathrm{eff}} = D$. In bulk aluminum, diffusion-limited oxidation is only an issue for oxide thicknesses greater than 1 micron. However, oxide layers as small as 2-6 nm can inhibit ignition in nano-scale particles.[10] In the presence of a passivating oxide shell, therefore, particle ignition can only occur if the diffusion rate of oxidizer through the shell increases, as it would during a phase change. Hence, ignition of passivated aluminum particles requires the alumina shell to melt before oxidizer can successfully diffuse to the metallic surface.

Vilyunov and Zarko[7] suggest an ignition model for aluminum particles based on the following criteria: (i) the protective metal oxide shell (Al_2O_3) is nonvolatile and indissoluble in aluminum, and (ii) aluminum metal itself is nonvolatile (T_{boil}(Al) $> T_{\mathrm{melt}}(Al_2O_3)$). Hence, the controlling process for ignition is melting of Al_2O_3, and and the bulk ignition temperature of aluminum is $T_{\mathrm{ig}} \approx T_{\mathrm{melt}}(Al_2O_3) \approx 2000°C$.

Micro- and nano-scale aluminum particles ignite more easily than the bulk, due partially to cracks in the passivating oxide shell. Cracking can occur due to mechanical stresses from an impending shock wave, phase changes in the alumina layer, or thermal expansion and density differences during rapid heating. Once the Al_2O_3 shell is fractured, local ignition can occur at the site of a crack or other defect due to intense oxidation of exposed metal prior to melting of the full shell. For this reason, ignition temperatures of small-scale Al particles are scattered, and values ranging from 470-2000°C have been reported.[7] Gaseous inclusions are another type of defect that promote metal boiling during ignition. This can cause hot jets of Al or Al_2O_3 to be ejected. Very small Al particles will even fragment at high irradiation intensities. Defects are related to particle size, properties of the oxide shell, and purity of the metal, and they clearly play an important role in the ignition of Al particles.

Glassman is credited with the earliest studies on ignition and combustion of metallic particles.[5,6] He proposed that metallic combustion should mimic that of

hydrocarbon droplets and burn time, t_b for a droplet of diameter D_0 should be governed by the D_0^2 law:

$$t_b = \frac{D_0^2 \pi D \rho}{4\dot{m}}, \tag{2.6}$$

where ρ is particle density, and $\dot{m}$ is the mass burning rate, given by

$$\dot{m} = -4\pi r^2 \rho \frac{dr}{dt}. \tag{2.7}$$

This law assumes the droplet is spherical and regresses uniformly during combustion. Glassman further supposed that ignition and combustion should depend on the melting and boiling points of both the metal and its oxide. According to this reasoning, he proposed that ignition of Al particles requires melting of the oxide shell, and the subsequent combustion achieves steady-state when the interior Al is at its boiling point, $T_{\text{boil}} \approx 2800°\text{C}$. Once developed, Al combustion occurs in the vapor phase because the boiling point of aluminum metal is lower than that of Al_2O_3 ($\approx 3000°\text{C}$). The vaporized metal burns homogeneously with gas-phase oxidizer at some distance from the propellant surface. As in hydrocarbon droplets, Al combustion is controlled by gas-phase diffusion of fuel and oxidizer. Steady-state combustion of Al produces a diffusion flame which is is driven by the fuel-oxidizer concentration gradient, and the flame front is several diameters larger than the initial metallic particles. The flame temperature is generally greater than the boiling point of Al, and ignition occurs in the range of 1700-2200 K.

Despite these similarities, the D_0^2 law of hydrocarbon droplet combustion cannot be readily extended to Al particles because of several factors. First, the combustion of Al—and the heat released thereof—is dominated by condensation of gaseous Al_2O_3. The liquid Al_2O_3 then deposits onto the particle surface, forming an oxide 'cap' that distorts the gas flow around the particle and prevents the particle surface from regressing uniformly as it burns. Hence, the entire spherical surface area is not

available for combustion and the exponent of D_0^n is reduced. The increasing fraction of deposited oxide reduces the burn rate and lowers the flame temperature toward the melting temperature of Al_2O_3, $T_{\text{melt}} \approx 2000°\text{C}$. Furthermore, unlike hydrocarbon droplets, Al particles do not burn out completely. Toward the end of combustion, the burgeoning oxide cap can cause jetting or fragmentation of the particle. While the majority of Al is burned within 1.0-1.5 milliseconds, the residual oxide cap is quite large and continues to radiate heat up to 6.5 milliseconds after metallic combustion has ceased. Consumption of metallic fuel occurs early in the combustion process, as universal burn times can range from <1 second up to 20 minutes.

The effect of the oxide cap on burn time was first modeled with a modified D_0^n law:

$$t_b = \frac{0.67 D^{1.5}}{a_k^{0.9}}, \tag{2.8}$$

with a_k accounting for the relative concentration of oxidizer (CO_2 or H_2O) in the gas. In a review of ten experimental studies, Beckstead clarified the D_0^n of Al combustion as it relates to temperature and pressure.[8] He evaluated the burn time of aluminum fuel particles with a range of initial diameters, $D_0 = 15 - 760\mu\text{m}$. At the micron-scale, he determined that burn time depends on particle diameter according to the relationship $t_b \propto D_0^n$, with n ranging from 1.2 for large particles to 1.9 for smaller ones. He further predicted that the burn rate exponent equals two at the moment of ignition and decreases to one at particle burnout, a phenomenon due strictly to the increasing fraction of Al_2O_3 covering the molten Al sphere. Beckstead's main conclusion was a modified empirical equation for burn time which is a function of pressure, initial temperature, and effective oxidizer concentration:

$$t_b = \frac{a D^n}{x_{\text{eff}} P^{0.1} T_0^{0.2}}. \tag{2.9}$$

Ignition and combustion in resinous and polymeric materials is different from that in pure metals. As mentioned previously, ignition of nitrocellulose begins with scission of the O-NO_2 bond and subsequent self-reaction between NO_2 groups and the nitrocellulose molecules. The ignition of double-base propellants is very similar, except that volatile nitric compounds begin to evaporate during heating. This leads to a higher concentration of gas-phase reactions at lower temperatures. Intense heat applied to a polymer, on the other hand, causes thermal decomposition of the entire network (i.e., cross-linking and covalent bonds are destroyed) and evaporation of monomers occurs. Hence, the ignition of pure polymers is described by a gas-phase model in which the controlling exothermal reactions occur between the gaseous decomposition products.

In summary, ignition in composite propellants depends on the thermal stability and kinetic barriers of each component: polymer binder, oxidizer, and metallic particle. This is clearly a complex process, which involves chemical reaction kinetics and physical transformations (evaporation, boiling, etc) of the propellant material. Nevertheless, simple models can be constructed by assuming the grain is a homogeneous material with local inhomogeneities that are smaller than the thickness of a heated layer. This thickness is given by $l \approx \sqrt{\alpha t_{\mathrm{ig}}}$.[7] Since the typical thermal diffusivity of a composite propellant is $\sim 10^{-3}$ cm^2/s and most ignition times are ~ 0.1 second, a safe estimate for the thickness of a heated layer in ignition is $l \approx 10\mu$m. Therefore, heterogenous mixtures (i.e., composites) can be modeled as homogeneous if mixture components are smaller than 10 microns and are distributed uniformly throughout the grain.

2.2.4 Propellants Applied to Solid Rocket Motors

The utility of a solid rocket propellant material is measured by its calorimetric value, or heat produced per gram, and the volume of combustion gases that are produced. Combustion gases can include N_2, H_2, CO, CO_2, and H_2O(g), depending

on the oxygen balance of the solid material. The gas volume produced is determined by molar amounts from a balanced decomposition reaction (assuming 100% yield). In a solid rocket motor, the rate of gas production is determined by the nature of the propellant, the geometrical form of the grain, and the venting area of the combustion vessel. The thrust produced by a jet of gas is given by

$$F = \bar{v}_e \dot{w} + (P_e - P_a)A_e, \tag{2.10}$$

where $\bar{v}_e$ is the exit velocity of the jet, $\dot{w}$ is the time-derivative of mass, A_e is the area of the exit cone, and P_e and P_a are the exit and atmospheric pressures, respectively. If the exit and atmospheric pressures are equivalent, Eq. (2.10) reduces to

$$F = \bar{v}_e \dot{w} \tag{2.11}$$

$$\frac{F}{\dot{w}} = \bar{v}_e = g I_{sp} \tag{2.12}$$

$$\tag{2.13}$$

where g is the acceleration due to gravity, and I_{sp}—the specific impulse—is the thrust produced by burning one pound of propellant in one second. Typical modern, high-performance propellants have $I_{sp} \approx 250 - 270$ seconds. Furthermore, I_{sp} is directly proportional to the square of heat of combustion, $I_{sp} \propto \sqrt{T_c}$ and indirectly proportional to the square root of the mean molecular weight of the combustion gases produced, $I_{sp} \propto 1/\sqrt{\bar{M}}$.[3] Hence, the most efficient propellants have high heats of combustion and produce gases of low average molecular weight. The temperature of a chemical reaction is directly related to the energy it produce; yet the overall specific impulse is a ratio of thrust to propellant weight. Careful engineering of rocket motors thus requires balancing the need for maximum thrust (via energy output) with minimal material weight.

Another important property of solid rocket propellants is that they burn at a uniform rate across all of the exposed surface. This is especially challenging for aluminized propellants because molten Al will agglomerate on the surface of the regressing propellant. For the purposes of controlled burning, the exterior surface of the propellant grain is prevented from burning by either directly bonding that surface to the motor casing (case bonded) or by coating it with an inhibitor material (cartridge loaded). This ensures that localized ignition occurs on the interior of the grain and combustion proceeds across the exposed pattern in the center. One disadvantage is that grains permanently bonded to the casing cannot be removed once spent.

The burn rate of a solid rocket propellant is a function of reaction pressure in the rocket motor chamber, material temperature, and the flow rate of produced gases parallel to the surface. Typical pressures in solid rocket motors range from 500-3000 psi. At low pressure and constant temperature, burn rate is given by Vieille's Law:

$$r = aP_c^n, \tag{2.14}$$

where n is the rate of burning index and $a = a(T)$ is the temperature coefficient of the rate of burning. Proper function of the rocket requires that $n < 1$. If $n > 1$, the rate of gas produced will be larger than the rate of gas removed through the exit nozzle. Hence, any increase in pressure would cause the rocket to burst, while a decrease in pressure would cause burnout.

Hartman and Morrow[4] note that ignition in solid rocket propellants occurs in three steps: (1) exposure to flame—via a pyrotechnic or hot gas igniter—until the temperature of the propellant surface reaches it autoignition point, (2) flame propagation across the surface, and (3) filling of the rocket motor chamber with combustion gases until the steady-state pressure has been reached. The rate of propellant consumption is given by

$$\frac{dm}{dt} = r\rho A_b, \tag{2.15}$$

where r, the burning rate, is a function of pressure, composition, gas-flow across the surface, and configuration and size of the grain. Depending on grain geometry, burning in a solid rocket motor can be regressive, neutral or progressive. During neutral burning, the grain's available surface area remains constant. Regressive and progressive burning cause the surface area of the propellant to decrease and increase, respectively.

The heats of combustion for solid rocket propellants range from 2-6 kJ/g. One element of propellant design focuses on increasing the available energy density. Attempts have been made to synthesize new high-energy-density (HED) materials or energetic polymers with nitro or azide groups in the chain backbone. At present, the most successful method to increase energy release is the addition of metallic fuels, such as Al, which is very dense and has a high heat of combustion. The temperature on the burning surface is around 573 K for double-base propellants, but this is elevated to 773-1273 K for aluminized compositions. The flame temperature is even hotter, ranging from 1500-6000 K. Table 2.3 compares the properties of the most common propellant classes: double base, CMDB, and composite. We see that adding AP and Al to a double base formulation increases the density, flame temperature, I_{sp}, burn rate, and n. Hence, all properties of CMDB propellants are improved over standard DB, with the exception of n, which should actually be minimized for better performance. Composite propellants with polymer binders instead of DB ingredients are a compromise in this area: a PVC/AP/Al formulation, for example, provides a higher flame temperature and I_{sp} without elevating burn rate or n.

Depending on the application, operating temperatures for solid rocket motors can range from -60 to 65°C, and pressures in the motor can exceed 1000 psi. These conditions can induce heavy mechanical loads, particularly in case bonded grains. Hence, solid rocket propellants must have high modulus, increased toughness, and

TABLE 2.3. Properties of typical solid rocket propellants. DB: double base; AP: ammonium perchlorate; Al: aluminum; PVC: polyvinyl chloride. Data taken from Ref. 4.

Propellant	Metal content (wt%)	Density (lb/in^3)	Flame temperature (°F)	I_{sp} (sec)	Burning rate (in/s)	Pressure exponent, n[a]
DB	0	0.058	4100	220-230	0.45	0.30
DB/AP/Al	20-21	0.065	6500	260-265	0.78	0.40
PVC/AP/Al	21	0.064	5600	260-265	0.45	0.38

[a]From Eq. (2.14).

high strain capability at both low and high temperatures. In addition to energy release and operating conditions, other engineering aspects to consider in rocket motor design include the strength and elasticity of the motor body and the density of the grain. Specifically, the latter can cause non-uniform burning if gaps or inclusions of air are present in the final grain. Most military rockets are produced to have a service life of ten years, but much of that time is often spent in munitions storage. Under normal storage conditions, rocket propellants are subject to thermal and oxidative aging. The most common failure mechanisms for solid propellants are autoignition from self-heating, loss of strain capability and subsequent cracking, heightened sensitivity to initiation, or mechanical damage from temperature cycling. Over the last 2-3 decades, material sensitivity and environmental impact have gained importance, as well.[4]

To summarize, effective solid rocket propellant materials must

i. be capable of self-sustained burning without additional oxygen from the air,

ii. burn in a controlled, layer-by-layer manner (i.e. no "worm-holing"),

iii. evolve as much heat energy as possible,

iv. produce low-$\bar{M}$ gases,

v. have $n < 1$ and a low $a = a(T)$,

vi. be safe to make, handle, and use, and

vii. remain chemically stable during long periods of storage.

3. LITERATURE REVIEW

3.1 Mn-containing Oxidizers

As discussed in Chapter 2, molecular additives are often used to improve Al combustion and decomposition of the oxidizer material.[11] Recent studies have focused on metallic nanoclusters, which have the benefits of high surface-to-volume ratios and large energy densities. Transition metal oxide nanoparticles, for example, have been shown to catalyze the thermal decomposition of ammonium perchlorate (AP) by decreasing the activation energy required for thermal decomposition. A study of Cr, Fe, Cu, and Mn oxides found that the most pronounced catalytic effect on AP combustion came from Mn_2O_3,[12] and the MnO_4^- cluster has been identified as a super-oxidizer that will bind with nanoscale Al and thereby reduce the amount of unreacted Al during combustion.[13] Furthermore, the reaction of manganese oxide with Al (the reducing agent) is similar to that for thermite:

$$3MnO_2 + 4Al \longrightarrow 2Al_2O_3 + 3Mn. \tag{3.1}$$

For this reaction to occur in the solid phase, however, the temperature cannot exceed 1000°C, well below the flame temperature of typical solid rocket propellants (see Table 2.3). Bulk Mn has $T_{\text{boil}} \approx 2000$°C. In a solid rocket motor, therefore, the combustion products of Eq. (3.1) will be gaseous Mn and Al_2O_3, with the latter condensing to form an oxide cap.

When selecting oxidizer materials for solid propellant formulations, a key design characteristic is oxidation potential. For aluminized formulations, heats of reaction, ΔH_{rxn} are dominated by reaction of the oxidizer with Al metal. Oxidation potential is roughly correlated with electron affinity (EA), and Table 3.1 ranks some common oxidizers according to their electron affinities. Clearly, perchlorate has a large electron affinity and subsequently high oxidation potential, and it is frequently used

TABLE 3.1. Electron affinities (EA) of several oxidizers. Data from the NIST Chemistry WebBook.[14]

Oxidizer	EA (eV)
$[ClO_4]^-$	5.25
$[MnO_4]^-$	4.80
$[NO_3]^-$	3.94
Cl^-	3.61
O_3	2.10
$[OH]^-$	1.83
O_2	0.448

in propellant formulations (e.g., NH_4ClO_4 and $KClO_4$). The design of new oxidizer materials has centered on synthesizing 'super-oxidizers' or 'super-halogens' with exceptionally high EAs.

As defined by Gutsev and Boldyrev,[15] super-halogens are a type of super-oxidizer with chemical formula $[MX_{k+1}]$, where M is a main-group or transition metal, and X is an electronegative atom, such as a halogen or oxygen. Because k is the maximum valence of M, the number of X atoms exceeds the oxidization state of M. One of the defining characteristics of a super-halogen is a large electron affinity (EA) which exceeds that of the pure halogen (or oxygen). This is due to collective effects; namely, the excess electron on a super-halogen anion will become delocalized over the available halogen atoms. This elevates the energy required to detach the electron, leading to high electron binding energies and increased cluster stability against photoionization. $Mn_xCl_y^-$ clusters, for example, possess EAs in the range of 4-6 eV, which are larger than that of pure Cl (3.61 eV).[16] The enhanced stability of the cluster anion arises from two effects: the aforementioned delocalization of the extra electron and preservation of the high-spin, d^5 configuration on the central Mn. Hence, $Mn_xCl_y^-$ clusters are salts with both magnetic and super-oxidizing properties.

Theoretically, Mn-oxide super-halogens with a high oxygen-balance (i.e., MnO_6 or MnO_7) might perform as well as perchlorates and speed up reaction rates during metallic combustion. This has prompted investigation into the synthesis and characterization of Mn-oxide clusters,[17–22] with the desire of synthesizing Mn-based super-oxidizers.

One critical aspect of designing Mn-based materials is that Mn clusters display an array of stable magnetic states. With an electronic configuration of $3d^5 4s^2$, Mn has a half-filled d shell which gives rise to a magnetic moment of 5 μ_B per atom. The coupling between Mn atoms is relatively weak, allowing for a wide variation in magnetic properties and significant sensitivity to impurities at the molecular scale. Dopants like oxygen cause significant changes in bonding, overall moments, and spin orientation. Numerous theoretical and experimental studies have examined the magnetic structure in pure manganese clusters.[18,23–29] The magnetic ordering of the Mn_2 dimer is very sensitive to interatomic separation,[18,23,26] while clusters containing 3-5 Mn atoms are all predicted to have ferromagnetic ground-states with magnetic moments of $\sim$5 μ_B/atom.[23,27,28] Mn_6 and Mn_7 are ferrimagnetic,[28,30] and there is a distinct transition from high- to low-spin configurations in Mn_n clusters with $n \geq 7$.[28] In all anionic clusters, Mn_n^- $(n = 2 - 8)$, the preferred ordering is ferromagnetic.[29]

The addition of a single oxygen into certain bare Mn clusters has also been considered.[17–21] Previous work on Mn_2O^- employed experimental negative-ion photoelectron spectroscopy (PES) and *ab initio* calculations to study the effect of oxygen on the magnetic properties of the Mn_2 dimer.[17] It was found that the presence of one additional O atom both strengthens cluster binding energy and alters the Mn-Mn magnetic coupling. In bare Mn_2 with $d_{\text{Mn-Mn}} \geq 3.06$ Å, the high-spin state with $S = 10$ is preferred,[23,26] and the low-spin state with $S = 0$ is $\sim$5 eV higher in energy.[18] The addition of oxygen reduces this gap, leading to nearly degenerate ferromagnetic and antiferromagnetic states in the Mn_2O^- anion.[17] Both isomers of

Mn_2O^- contribute to peak broadening in the experimental PES and must be included in calculations to accurately reproduce the spectral peak positions and shapes.

Mn_5O^- and Mn_6O^- were studied by Jones *et al.* using a combination of negative-ion PES and quantum calculations.[19] They found that the ferromagnetic states of Mn_5 and Mn_6 are destabilized by the addition of oxygen, and the overall magnetic moment is reduced compared to pure Mn_n clusters. Another conclusion of this work was the identification of several nearly-degenerate "isomags." Akin to structural isomers, isomags are magnetic isomers with comparable binding energies and identical spins but different distributions of local moments. Because of weak magnetic exchange interactions between Mn moments, there is a small barrier to spin reorientation which is strongly affected by changes in Mn-Mn interatomic separation and atomic composition.[18,26,31] As a result, Mn_5O^- and Mn_6O^- display a number of magnetic isomers, each with a subset of possible isomags.[19] The authors further conclude that the presence of multiple peaks in the PES spectra can only be accounted for by including contributions from all isomers and their corresponding isomags. Reasonable agreement between theory and the experimental vertical detachment energies in the PES spectra were observed, though for Mn_5O^- and Mn_6O^- a constant energy shift was required to accurately reproduce the experimental peaks. More accurate first-principles calculations are needed to identify the most stable Mn-O cluster geometries and their EAs.

3.2 Al-cyclopentadienyl Clusters

Nanometer scale Al is attractive as a route to increasing oxidation rates and potentially lowering the ignition threshold of solid propellant formulations. This has led several authors to pursue surface passivation of aluminum nanoparticles with organic functional groups.[10,32–35] As an example of such a material, H. Schnöckel and coworkers have previously synthesized a 50-atom Al cluster surrounded by cy-

clopentadienyl Cp* ($C_5[CH_3]_5$) ligands.[36] The metal-ligand (M-L) interaction on the exterior of the cluster consists of η^5 bonds between the Al^+ and the $[Cp^*]^-$ rings.

A reliable method to synthesize Al(I) compounds has been implemented by Schnöckel *et al.* (Refs. 37–40). The organic ligands they choose are commonly found in metallocenes; for example, Cp (C_5H_5) and Cp* readily bond with both transition metals[41] and main-group elements[42–45] in a variety of hapticities (η^1, η^2, η^5).[45,46] Others have observed these clusters while studying the formation and dissolution of metals and propose that their formation occurs because of an energy barrier along the path connecting Al nanoclusters and solid metallic Al.[47,48] They are able to kinetically "trap" these clusters at low temperatures where they are stable enough for x-ray crystallographic analysis and NMR spectroscopy.[49]

Bonding in main-group metallocenes, ECp (E = Li–Cs, B–Tl) and ECp_2 (E = Be–Ba, Zn, Si–Pb), has been analyzed in terms of both the molecular orbital (MO) correlation diagram and energy decomposition analysis (EDA).[44,50,51] The MO diagram of half-sandwich complexes shows that the a_1 and e_1 valence *p* orbitals of E^+ have the correct symmetry to overlap with the filled a_1 and e_1 orbitals of Cp^-. The higher-lying, unfilled e_2 orbitals of Cp^- do not participate in bonding. This differs from transition metal metallocenes, in which filled *d* orbitals possess the correct symmetry to overlap with the anti-bonding orbitals of the ligand, i.e., so called "π backbonding." Another interesting characteristic of half-sandwich metallocenes is the duel character of the M-L bond. EDA reveals that the M-L interaction is neither entirely ionic nor covalent; rather, some fraction of the attractive interaction can be attributed to an electrostatic interaction (ionic) while the other results from covalent orbital interactions. In AlCp, for example, the M-L bond is 64.6% ionic and 35.4% covalent. Furthermore, the qualitative picture of bonding given by the MO diagram is confirmed by EDA; the E_2 contribution to the total orbital interactions is only 5.1%, with the remaining 94.9% split equally between bonding MOs with A_1 and E_1 symmetry.[50,51]

The study of larger aluminum clusters builds on a large body of work on low-valence aluminum coordination complexes.[37–40,52] A number of these clusters, such as the tetramers $Al_4Cp^*_4$ and $Al_4(C_5Me_4H)_4$, crystallize into low-symmetry solid state structures and have been observed via x-ray crystallographic analysis and NMR spectroscopy.[49,53] Attempts to isolate similar compounds with unmethylated Cp (C_5H_5) ligands have generally been unsuccessful due to their tendency to disproportionate to aluminum metal and higher-valence compounds such as $AlCp_3$.[38,53] Currently very little is known about the stability or decomposition of the larger aluminum-cyclopentadienyl compounds which contain a significant mass fraction of aluminum.

Bonding in Al-η^5 species has been studied extensively since the first successful experimental synthesis of a stable molecular Al(I) compound.[52] Computational studies on these materials are limited and mainly restricted to work on aluminum metallocenes. Early Hartree-Fock calculations by Ahlrichs and coworkers[54] examined basic AlCp as well as Al_4Cl_4, Al_4F_4, and Al_4Cp_4. A limitation of this work was the substitution of H for the methyl groups, effectively modeling Cp^* with Cp. Furthermore, no correlation effects were included, and with their methodology Al_4Cp_4 was found to be unstable with respect to decomposition into monomers. A number of later works considered the simple Al metallocenes in the context of examining trends in a broader range of main-group metallocenes or similar organometallics.[45,50,55,56] In recent years Huber and Schnöckel have performed density functional theory calculations in support of their x-ray diffraction and ^{27}Al NMR studies of larger aluminum-Cp type clusters.[53,57] They proposed that the large clusters such as $Al_{50}Cp^*_{12}$ may serve as a type of barrier state that prevents the smaller compounds from spontaneously decomposing to metallic aluminum and trivalent aluminum species. Expanded computational studies of these materials are highly desirable to elucidate their reactivity, stability, and potential combustion properties, which are important issues for energetics applications.

3.3 Carboxyl-terminated Polymer Coatings

Carboxylic acid self-assembled monolayers (SAMs) have become important alternatives to traditional SAMs based on alkanethiols or alkoxysilanes[58] and have been used as passivating coatings for nano-Al propellant additives.[10,34,59] As discussed in a recent review by Jadhav,[58] *n*-alkanoic acid SAMs have been studied on a variety of surfaces for use as lubricants, corrosion-resistant materials, and catalysts. Furthermore, carboxylic acids can be use to build uniform SAMs in 2-D (thin films) and 3-D (surface of nanoparticles) structures. The latter are particularly useful in the prevention of nanoparticle agglomeration or surface oxidation.

The inherent reactivity of Al(111) and Al(100) with carboxylic acids is somewhat different from that of transition metal surfaces. Ma and Zaera[60] have characterized the reactions of carboxylic acids with oxygen-rich transition metal surfaces in terms of acid-base reactions, where the surface oxygen atoms act as strong Brønsted bases and transfer protons to form the conjugate bases (carboxylates). Clean Al surfaces, however, have a high affinity for reaction with O.[61] For example, it is known that the hydroxyl O-H bond of methanol is easily broken, and that methanol will readily adsorb onto Al(111) as a methoxy anion $[OCH_3]^-$.[62]

Carboxylic acids also bind to Al(111) in their anionic states. The simplest alkanoic acid—formic acid, HCOOH—reacts with the clean Al(111) surface to form a monolayer of adsorbed formate. This adsorption reaction is preceded by scission of the O-H bond and continues until the surface is fully saturated. Crowell[63,64] showed that the preferred adsorption configuration is bridge bonding (binding at two surface Al sites). Heavy exposure levels of formic acid cause a multilayer coating to form, in which molecular acid condenses on top of the adsorbed formate layer. This causes additional features to appear in the IR spectra: most notably, an OH scissoring mode at 975 cm^{-1} and a stretching mode around 2640 cm^{-1}, which is attributed to H-bonding, $\nu(OH\cdots O)$, between adjacent formic acid dimers. At increased layer concentration, Crowell found the IR spectrum of the HCOOH/Al(111) system com-

pared well with that of crystalline formic acid. In terms of thermal stability, the formic acid layers on Al(111) condense at low temperatures (120-130 K) and desorb around 170 K. Between 500-700 K, formate decomposes and 'cracks' into desorption products such as H_2 and C_2H_2. This also generates atomic C, O, and H which can adsorb onto the surface or diffuse into the lattice.

The adsorption of acetic acid, CH_3COOH, on Al(111) has many similarities to formic acid.[65] Acetic acid also undergoes O-H bond scission to form a full monolayer of adsorbed acetate, with bridge bonding of COO^- moieties preferred. Higher concentration levels lead to the development of a physisorbed multilayer of condensed acetic acid above the bound formate surface. As with formic acid, the acetic acid molecules in the condensed layer interact as dimers, and the $\nu(OH\cdots O)$ mode due to H-bonding is detected at 2740 cm^{-1}. The acetic acid layer condenses at 120 K and remains thermally stable until about 167 K. After molecular desorption of the top-most layer, further heating leads to thermal decomposition of the bound formate molecules. Decomposition products begin to adsorb onto the surface at 200 K, and full thermal decomposition is achieved between 500-700 K. Unlike formic acid, however, thermal stability is directly related to monolayer concentration. At low exposures, molecular desorption occurs at temperatures close to 123 K. In a study of thermal stability of acetic acid adsorbed on Al(111), Chen[65] found that increasing the acetic acid surface coverage decreases the decomposition rate. His assertion is that attractive interactions between adsorbates raise the activation energy for thermal decomposition, thereby enhancing stability of the acetate monolayer. Furthermore, Zhong and Adams[66] have confirmed via DFT calculations that the energetically-preferred configuration of acetic acid on Al(111) is a bridging motif, and they find bonding in the bridge motif to be over three times stronger than that in a monodentate (single surface Al site) motif.

Beyond simple formic and acetic acids, there have been numerous studies of long-chain alkanoic acids on both Al and Al_2O_3. Brown conducted the earliest experiments

on alkanoic acids adsorbed onto γ-alumina.[67,68] He studied oligomers $C_nH_{n+1}COOH$ with $n = 0, 1, 2, 3, 7$ and concluded that short chains ($n \leq 11$) universally have trans stereochemistry, i.e., their backbones have regular zig-zag patterns, with no rotation about the C-C bond. Additional studies have looked at self-assembly of long-chain fatty acids on Al_2O_3 (Refs. 69–73 and the references therein.)

In addition to forming interesting SAMs, carboxylate-terminated molecules are excellent burn rate modifiers for propellants. For example, lead salicylate and lead stearate are catalysts that produce "mesa" effects in the combustion of a solid propellant.[4] Specifically, they cause a region of pressures in which burn rate actually *decreases* with increasing pressure. The benefit of adding modifiers like these is a rapidly accelerating burn rate in the post-mesa pressure region. In the area of metallic fuels, Al nano-clusters passivated with fluorinated oligomer chains have been successfully synthesized experimentally,[10,34,59,74] but no theoretical work has been done to clarify whether surface coverage truly results from covalent bonding or simply physical deposition.

4. COMPUTATIONAL METHODOLOGY

The method employed in this dissertation is electronic structure theory—more specifically, Density Functional Theory (DFT).[75,76] DFT is a theory describing the groundstate properties of a system of electrons (viz. atoms composed of bound electrons). The motion of electrons in their bound state is described by quantum mechanics, beginning with the most-fundamental equation—the time-dependent Schrödinger equation:

$$i\hbar\frac{\partial\Psi(\vec{r},t)}{\partial t} = \mathbf{H}\Psi(\vec{r},t), \tag{4.1}$$

where $\hbar = h/2\pi$ is the reduced Planck's constant, $\mathbf{H}$ is the Hamiltonian, and $\Psi(\vec{r},t)$ is a wavefunction that gives the probability amplitude of finding an electron at position $\vec{r}$ at time t. The first simplifying assumption is that electrons in atomic orbitals move non-relativistically (valid for $\alpha Z \ll 1$) and can therefore be described by the Hamiltonian

$$\mathbf{H} = -\frac{\hbar^2}{2m}\nabla^2 + V(\vec{r},t). \tag{4.2}$$

If we then assume that the electrons are moving in a time-independent potential, $V(\vec{r},t) = V(\vec{r})$ and $\Psi(\vec{r},t) = \psi(\vec{r})f(t)$. Substituting these expressions into Eq. (4.1) and using separation of variables, we find

$$\begin{aligned}
i\hbar\frac{\partial\left(\psi(\vec{r})f(t)\right)}{\partial t} &= \left[-\frac{\hbar^2}{2m}\nabla^2 + V(\vec{r})\right]\psi(\vec{r})f(t) && (4.3)\\
i\hbar\frac{\partial f(t)}{\partial t}\psi(\vec{r}) &= \left[-\frac{\hbar^2}{2m}\nabla^2\psi(\vec{r}) + V(\vec{r})\psi(\vec{r})\right]f(t) && (4.4)\\
\frac{i\hbar}{f(t)}\frac{\partial f(t)}{\partial t} &= \frac{1}{\psi(\vec{r})}\left[-\frac{\hbar^2}{2m}\nabla^2\psi(\vec{r}) + V(\vec{r})\psi(\vec{r})\right] && (4.5)\\
E\psi(\vec{r}) &= \left[-\frac{\hbar^2}{2m}\nabla^2 + V(\vec{r})\right]\psi(\vec{r}) && (4.6)
\end{aligned}$$

(4.7)

Hence, we have reduced Eq. (4.1) to an eigenvalue problem of the form $E\psi(\vec{r}) = \mathbf{H}_{\vec{r}}\ \psi(\vec{r})$. The fundamental assumption of DFT is that the groundstate properties of a system of electrons can be fully described by the groundstate electronic density, i.e., $E_0 = E_0[\rho_0(\vec{r})]$, and

$$\mathbf{H}\psi_0(\vec{r}) = E_0[\rho_0(\vec{r})]\psi_0(\vec{r}). \tag{4.8}$$

$E_0[\rho_0(\vec{r})]$ is called the Kohn-Sham energy of the system, and $\psi_0(\vec{r})$ is the Kohn-Sham wavefunction. The Kohn-Sham energy can be expanded as

$$E[\rho(\vec{r})] = T[\rho(\vec{r})] + V_{n-e}[\rho(\vec{r})] + V_{e-e}[\rho(\vec{r})] + E_{XC}[\rho(\vec{r})], \tag{4.9}$$

where T is the kinetic energy of a non-interacting electron, V_{n-e} is the nuclei-electron Coulombic attraction, V_{e-e} is the electron-electron Coulombic repulsion, and E_{XC} is an exchange-correlation energy which corrects for all other non-classical $e-e$ interactions. Hohenberg and Kohn[75,76] showed that the constructed energy functional, $E_0[\rho_0(\vec{r})]$, will have its minimum value for the correct choice of $\rho_0(\vec{r})$. More explicitly, the eigenvalue, $E_0[\rho_0(\vec{r})]$ that satisfies Eq. (4.8) will be the groundstate energy of the electronic system.

Nevertheless, the exact form of $E[\rho(\vec{r})]$ is unknown, and parameterization of E_{XC} involves fitting to experimental data. The most widely-used approximations to E_{XC} are the Local Density Approximation (LDA) and Generalized Gradient Approximation (GGA). LDA assumes that the effective exchange-correlation potential depends strictly on $\rho_0(\vec{r})$, neglecting its spatial variation. This approach is good for modeling solids but overestimates bond strengths in molecules. GGA, on the other hand, is often called 'non-local' because it incorporates terms based on $\rho_0(\vec{r})$ and $\nabla\rho_0(\vec{r})$. This gives more accurate geometries and vibrational frequencies for isolated molecules.

Recall that the eigenvector of Eq. (4.8) is $\psi_0(\vec{r})$, the Kohn-Sham wavefunction. The estimated mathematical form of $\psi_0(\vec{r})$ is different depending on the electronic system to be modeled. In solids, for example, the potential is assumed to be periodic and $\psi_0(\vec{r})$ is generally represented by the product of a plane wave with a periodic Bloch function:

$$\psi_{n\vec{k}}(\vec{r}) = e^{i\vec{k}\cdot\vec{r}} u_{n\vec{k}}(\vec{r}), \tag{4.10}$$

where $u_{n\vec{k}}(\vec{r})$ has the same periodicity as the potential. Molecular systems, on the other hand, are written as linear combinations of atomic orbitals (LCAO method):

$$\psi(r,\theta,\phi) = \sum_s c_s \chi_s = \sum_s c_s \left[R_{nl}(r) Y_l^m(\theta,\phi)\right], \tag{4.11}$$

where Y_l^m are Laplace's spherical harmonics, and n, l and m are the principle, azimuthal, and magnetic quantum numbers. Most LCAO basis sets are based on Slater type orbitals (STO) or Gaussian type orbitals (GTO), although these are often modified to better describe hybridization, excited states or other properties of the valence orbitals.

All calculations on Mn-oxide clusters with unpaired electrons (i.e. multiplicity $M > 1$) were performed with spin-unrestricted DFT using the PBE functional[77–79] for both exchange and correlation. A large aug-cc-pvdz basis set was used, and all simulations were performed using Gaussian 09.[80] Global energy minima for all clusters were found by considering a large number of possible configurations and oxygen locations. This methodology was validated by successfully reproducing previous structures and VDEs for Mn_2O^-(Ref. 17).

One critical aspect of calculations on Mn-oxide clusters is a careful description of the magnetic ordering. Cluster multiplicity M is herein defined as $M = S + 1$, where S is the sum of individual atomic moments in units of $\mu_B/2$. For example, the spin moment on a single Mn atom is $5/2$ μ_B arising from the five unpaired d

electrons. Hence, in our designation, $S = 5$ and $M = 6$ for Mn. We consider all possible spin isomers for each cluster, identifying them by the following naming convention. Ferromagnetic (FM) indicates that all Mn magnetic moments are parallel (i.e., a high-spin cluster). Antiferromagnetic (AFM) indicates that equal numbers of Mn moments are aligned in the opposite direction, and the net cluster moment is $S = 0$. Finally, fM indicates ferrimagnetic ordering (low-spin). This arises when more moments are aligned parallel than anti-parallel; the result is a reduced, but non-zero spin moment. Only clusters with AFM or fM ordering can have multiple non-degenerate isomags. These are treated with a multistep approach, in which spin orientation (but not magnitude) is fixed and the wavefunction is checked for magnetic instabilities during the course of the geometry optimization.

Once the lowest-energy isomags are identified for the anionic clusters, the vertical detachment energies (VDEs) are calculated; these correspond to transitions to the neutral cluster with a multiplicity of $M \pm 1$. The VDEs are defined as the differences in the single point energies of the anions and neutral clusters, with the latter fixed at the optimized anion geometry. The excited-state energies are calculated using time-dependent density functional theory (TD-DFT), again with the aug-cc-pvdz basis set. Lastly, an adiabatic electron affinity (AEA) for each cluster is estimated by calculating the energy difference between the optimized, lowest-energy isomags of both the anion and neutral. This differs from the VDE calculations in that both the structural parameters and magnetic structure of the neutral cluster are allowed to relax. This allows for the possibility of transitions to additional structural isomers with potentially different multiplicities, a characteristic which is unique to clusters with multiple spin moments.

For calculations on aluminum organometallic clusters, we choose methods that are suitable for modeling the Al-η^5 interaction. Geometry optimizations are performed using DFT with the B3LYP functional[81] and a 6-31G(d,p) basis set. For comparison and assurance of accurate thermodynamic values, we also calculate heats of formation

using the G2 method[82] for a number of the smaller η^5 clusters. B3LYP/6-31G(d,p) gives accurate thermodynamics while still being efficient enough to calculate structures and vibrational properties of the largest cluster (350 atoms). All calculations are again performed with the Gaussian 09 program.[80] For geometry optimization of the largest cluster, $Al_{50}Cp^*_{12}$, a multilayer QM:MM method[83] is used in which the methyl groups on each Cp^* ligand are modeled with Rappe's Universal Force Field (UFF)[84] and remaining atoms are treated with DFT. Layer neutrality is automatically imposed such that the dangling bonds in each layer are passivated with hydrogen. This hybrid approach is only used in finding optimized geometries of $Al_{50}Cp^*_{12}$; thermodynamic calculations are then performed with a full DFT calculation at the B3LYP:UFF geometry. The small structural differences between the QM:MM and full DFT approach have a minimal effect on calculated energy difference or enthalpies of formation. This is because the energy barrier for rotation of the outer methyl groups is extremely small and the contribution of the methyl vibrations to the thermodynamic partition function is negligible.

Energetic properties of the Al-organometallic clusters are calculated using Cheetah 5.0,[85] a chemical equilibrium code developed at Lawrence Livermore National Lab. The heat of combustion, ΔH_c (in kcal/g) for each cluster is found by assuming complete chemical reaction of all aluminum clusters in air . I_{sp}s are also calculated with Cheetah; the materials of interest are assumed to initially burn in a combustion chamber at a pressure of 1000 psi before expanding isentropically through an ideal rocket nozzle and into an ambient pressure environment. Chemical equilibrium is assumed to hold at every point during the expansion process and the products are allowed to evolve as they expand. The BKWS equation of state[86] is used to calculate chemical equilibrium. In all cases the oxidizer/organometallic mixture is optimized until the mixture is approximately oxygen balanced.

Calculations of adsorbed carboxyl-terminated oligomers on Al surfaces are studied with DFT using a combined Gaussian and plane waves method (GPW) as imple-

TABLE 4.1. Elemental assignments for the combined basis sets, BS-I and BS-II. GTH bases are those provided with the cp2k distribution.

Element	BS-I	BS-II
Al	DZVP-GTH	QZV3P-GTH
C,H,O,F	DZVP-MOLOPT-GTH	TZV2PX-MOLOPT-GTH

mented in the Quickstep[87] module of cp2k. The GPW method uses a dual basis: atom-centered Gaussian orbitals represent the wavefunction and the Kohn-Sham matrix, while plane waves represent the electronic density. This combined representation increases computational efficiency, making optimizations of larger systems more tractable. Exchange and correlation are modeled with PBE[77–79] and PBE+vdw, a dispersion-corrected, semiempirical functional of Grimme.[88] As shown in Table 4.1, Al atoms are treated with the GTH-DZVP basis set, while atoms constituting the oligomer chains are represented with the GTH-DZVP-MOLOPT bases, all of which are provided with the cp2k package.

Nanoscale Al particles are modeled with bare Al(111) and Al(100) surfaces. cp2k's implementation does not support **k**-points. Therefore, the Al(111) surface is modeled with a large, 6x6x6 slab (216 atoms) placed in a periodic box of dimensions $a = 17.184$ Å, $b = 14.883$ Å, and $c = 30.00$ Å . A large vacuum of ≈ 15 Å is used in the z direction to ensure no interaction between the bottom and top surfaces of the periodic images. The Al(100) surface is built from a 3x3x3 supercell and contains only 108 atoms. The cell dimensions for this slab are $a = 12.15$ Å, $b = 12.15$ Å, and $c = 30.00$ Å. Both surfaces are optimized with atomic positions in the bottom two layers held fixed at their bulk values. A single adsorbate (1/18 ML) is then placed on the surface and the entire system is reoptimized with 4 layers of Al held fixed, i.e., only the adsorbate and top-two Al layers are allowed to relax. The c dimension of the simulation cell is expanded for longer-chain adsorbates, ensuring

at least 10 Å of separation between the adsorbate and the periodic image of the bottom of the slab. Finally, the energies of the adsorbates are found via optimization of isolated molecules placed in a $20 \times 20 \times 20$ Å^3 box. For charged adsorbates (anions), electrostatic interactions between periodic images are decoupled using density derived atomic point charges,[89] and the Poisson equation is solved with a multipole solver.[90]

Adsorption energies are defined by the equation

$$E_a = E_{\text{slab+adsorbate}} - (E_{\text{slab}} + E_{\text{adsorbate}}). \tag{4.12}$$

Hence, negative adsorption energies indicate favorable binding. For comparison and assurance of accurate energies, E_a for propionate chemisorbed on Al(111) is also calculated using BLYP,[91,92] PADE,[93] and an extended basis set (see Table 4.1). Furthermore, optimized geometries and vibrational frequencies for the isolated adsorbate molecules are compared with results from Gaussian 09[80] using B3LYP/TZVP.[81,94] The cp2k frequencies are used to construct the vibrational partition function of each adsorbate in its gaseous and bound states at 298 K; the difference is then added as a thermal correction to E_a, neglecting any contribution from the Al metal.

5. MANGANESE-BASED SUPERHALOGEN OXIDIZERS*

5.1 Geometry and Magnetic Ordering in Anionic $Mn_xO_y^-$ Clusters

The ground state for each manganese oxide cluster is found by calculating cluster energy as a function of spin multiplicity. We calculate all allowed multiplicities for different starting geometries of each cluster to determine the overall lowest-energy configuration. Figures for the corresponding ground-states appear in the following subsections; bond lengths are given in Å, while magnetic moments on the Mn atoms (shown in italics) have units of μ_B. The magnetic moments of O atoms are small relative to those of the manganese, generally on the order of 0.1 μ_B. These contribute little to the net cluster moment and thus are not shown on the figures. As discussed in the following subsections, the presence of the O atoms slightly alters the spin moment on adjacent Mn atoms. The more prominent effect from adding oxygen is a change in the orientation of individual spins.

Cluster geometries are validated by the experimentally measured vertical detachment energies (VDEs). These correspond to the energy difference between the anion and the neutral cluster with the latter fixed at the anion geometry. The anion's electron is ejected via photoionization and the electronic structure rapidly relaxes to a new state. The kinetic energy of the ejected electron (EKE) is measured experimentally via PES, and the electron binding energy (EBE) is derived from knowledge of the incident photon energy via the conservation equation

$$\mathrm{EBE} = h\nu - \mathrm{EKE}, \tag{5.1}$$

where ν is the laser frequency. The resulting binding energies are compared with atomic-level simulations, offering a direct comparison to theoretical calculations of

*Reprinted with permission from "Magnetic structure variation in manganese-oxide clusters" by K. S. Williams et al., The Journal of Chemical Physics **136**, 134315 (2012). Copyright 2012 American Institute of Physics. Direct link: http://dx.doi.org/10.1063/1.3698279.

small atomic clusters. This combined experimental-theoretical approach has been shown to successfully identify the ground state of gas-phase clusters with nearly-degenerate magnetic states.[95]

5.1.1 Mn_3O^-

Mn_3O^- possesses several structural isomers, each with two distinct energy minima corresponding to high- and low-spin multiplicities (denoted FM and fM, respectively). A tetrahedral structure with $M = 7$ is the global minimum. This corresponds to ferrimagnetic ordering in which one Mn atom is aligned anti-parallel to the other two. There is an additional local minimum at $M = 17$ corresponding to ferromagnetic ordering with all spins fully aligned; it lies 0.16 eV higher in energy, and its calculated VDEs are well below the onset of the experimental PES spectra. This is a general trend seen in all four clusters; namely, alternate structures or spin configurations of the anion that lie approximately 0.15 eV or higher than the ground state are not observed experimentally. The high-spin isomers for Mn_3O^- and other clusters are detailed in Appendix I.

The ground-state geometry for Mn_3O^- with M=7 is shown in Figure 5.1(a). The lone oxygen has a small spin magnitude of 0.09 μ_B, while the overall magnetic moment is $S = 6$. We note that the optimized geometry of Mn_3O^- does not retain perfect T_d symmetry; rather the tetrahedron is compressed and the symmetry is reduced to C_s. This is a result of the shortened Mn-O bond length, 1.91 Å, which is smaller than the average Mn-Mn bond distance and approaches the Mn-O bond length of Mn_2O^- (1.80 Å).

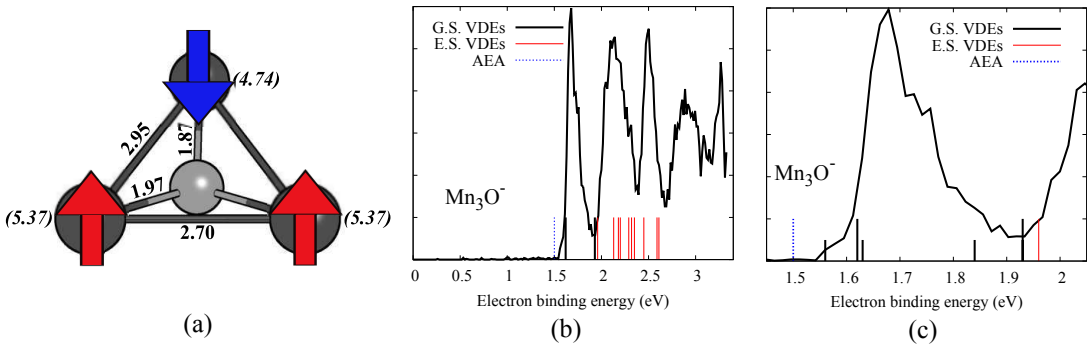

FIG. 5.1. (a) Ground-state structure of Mn_3O^-. (b) Experimental PES for Mn_3O^- (solid line). VDEs for transitions from the ground-state anion to the fixed-geometry, ground-state neutral are shown as black lines, while transitions to the excited states of the fixed-geometry neutral are red. The blue line is the AEA. (c) Zoomed version of (b) which includes additional VDEs for three higher-energy isomags of the neutral cluster (shown as short lines).

In the bare, planar Mn_3 cluster, the preferred magnetic ordering is FM, and the cluster moment is $S = 15$.[23,24,27–29] The addition of oxygen alters the Mn-Mn coupling and stabilizes a ferrimagnetic ground-state with a reduced moment in Mn_3O^-. The average atomic moment, however, is not significantly altered. As shown in Figure 5.1(a), the mean spin moment is 5.16 μ_B, close to the free-atom value of 5 μ_B.

The ground state of Mn_3O^- has exactly one isomag, since there is no preference as to which Mn atom in the plane is anti-parallel. Calculation of the corresponding VDEs is straightforward in this case, as only two vertical transitions have to be considered, 7→6 and 7→8, without regard to which Mn moment is anti-aligned. Figure 5.1(b) shows the calculated VDEs plotted together with the experimental PES for Mn_3O^-. The black lines designate transitions 7→6 and 7→8, where the geometry of the ground state neutral cluster is held fixed at that of the optimized anion. The

TABLE 5.1. Vertical detachment energies for ground-state $M \pm 1$ transitions in $Mn_xO_y^-$ clusters.

Cluster	Transition	VDE (eV)	Exp. (eV)[a]
Mn_3O^-	7→6	1.62	1.68
	7→8	1.93	2.09
$Mn_3O_2^-$	5→4	2.05	2.01
	5→6	1.66	1.65
Mn_4O^-	12→11	1.92	2.05
	12→13	2.48	2.53
$Mn_4O_2^-$	2→1	1.90	1.97
	2→3	2.39	2.29

[a]Experimental values are estimated from the spectral peaks and have an uncertainty of ±0.100 eV.

red lines indicate transitions to the neutral cluster's excited states, and the blue line is the adiabatic electron affinity. The latter is the energy difference between the optimized anion and optimized neutral and serves as a lower bound for the PES data. The VDEs plotted in Figure 5.1(b) are also listed in Table 5.1. The lowest ground state VDE falls very close to the first prominent peak in the experimental spectra; as listed in Table 5.1, our theoretical value differs from experiment by only 0.06 eV. The second ground state VDE falls approximately 0.16 eV lower than experiment. Higher-energy spectral features can be attributed to excited state transitions.

5.1.2 $Mn_3O_2^-$

The $Mn_3O_2^-$ cluster also has multiple structural isomers. We find that a ring structure with $M = 5$ is the global minimum. Shown in Figure 5.2(a), this is a ferrimagnetic cluster with $S = 4$. As was the case for Mn_3O^-, the $Mn_3O_2^-$ cluster has a higher-energy minimum for ferromagnetic ordering at $M = 15$. This structure lies 0.36 eV higher in energy and is shown in Appendix I. The overall cluster moment ($S = 4$) is reduced compared to that of Mn_3O^- ($S = 6$). The average Mn moment is

reduced to 4.77 μ_B, slightly lower than the free-atom value for Mn. Another difference is loss of symmetry and "flattening" of the cluster into a planar C_{2v} configuration.

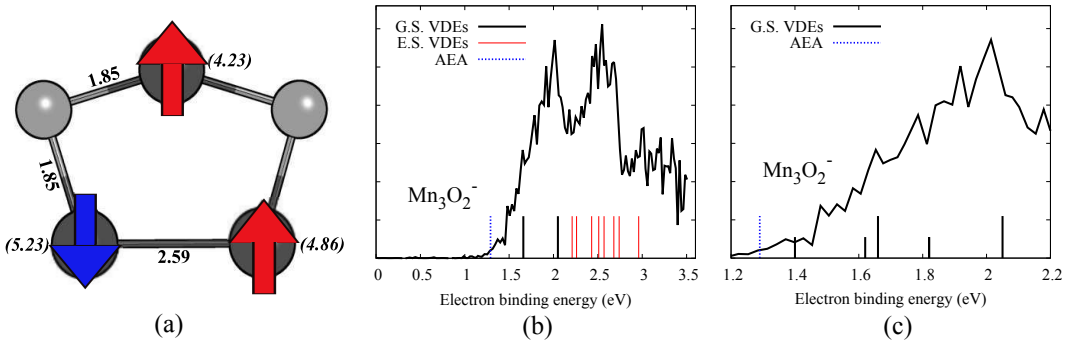

FIG. 5.2. (a) Ground-state structure of $Mn_3O_2^-$. (b) Experimental PES for $Mn_3O_2^-$ (solid line). VDEs for transitions from the ground-state anion to the fixed-geometry, ground-state neutral are shown as black lines, while transitions to the excited states of the fixed-geometry neutral are red. The blue vertical line in the AEA. (c) Zoomed version of (b) which includes additional VDEs corresponding to three higher-energy isomags (shown as short lines).

In the ground-state of $Mn_3O_2^-$, one Mn moment is anti-aligned with the other two. The lowest energy isomag corresponds to an anti-parallel moment on a bottom Mn (see Figure 5.2(a)). The two isomags with the anti-aligned moment residing on a bottom Mn are equivalent in energy, while the isomag with opposite spin on the top Mn atom is 0.25 eV higher in energy. For calculating VDEs, we must therefore consider $M \pm 1$ transitions (5→4 and 5→6) in which the lowest-energy isomag of the anion is used as the starting geometry for the neutral cluster. The experimental PES and calculated VDEs of $Mn_3O_2^-$ are plotted in Figure 5.2(b). The first four excited states of the neutral cluster contribute to the higher-energy peaks.

5.1.3 Mn_4O^-

The lowest-energy cluster of Mn_4O^- is a bipyramid with $M = 12$ and is shown in Figure 5.3(a). It has a ferrimagnetic arrangement of spins with $S = 11$, and the average Mn moment/atom (from Figure 5.3(a)) is 4.97 μ_B. Bare Mn_4 has a tetrahedral structure. Both fM ($S = 10$) (Ref. 24) and FM ($S = 20$) ground states of Mn_4 have been reported,[23,27–29] with the latter having stronger theoretical support. The preferred FM state of Mn_4 is destabilized by the addition of oxygen.

We note that due to the even number of Mn atoms in this cluster, there are two additional local minima which arise from magnetic effects. Namely, there is a minimum for AFM ordering at $M = 2$, in which exactly half of the spins are anti-aligned, and another for FM ordering at $M = 22$, in which all spins are parallel. These alternate spin isomers (given in Appendix I) are higher in energy than the fM cluster by 0.25 and 0.43 eV, respectively. As in Mn_3O^-, the presence of the shortened Mn-O bond distance compresses the bipyramid, reducing it to C_s symmetry.

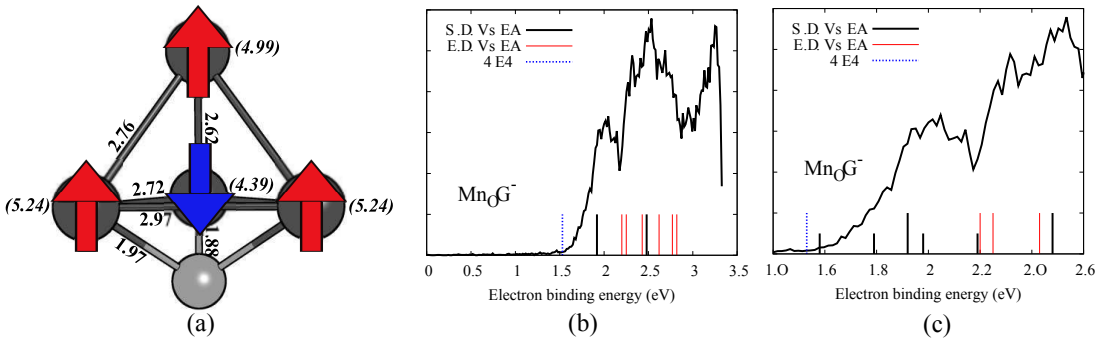

FIG. 5.3. (a) Ground-state structure of Mn_4O^-. (b) Experimental PES for Mn_4O^- (solid line). VDEs for transitions from the ground state anion to the fixed-geometry, ground-state neutral are shown as black lines, while transitions to the excited states of the fixed-geometry neutral are red. The dashed vertical line is the AEA. (c) Zoomed version of (b) which includes the VDEs for four additional non-degenrate isomags (shown as short lines).

For Mn_4O^- in a bipyramid geometry, there are two distinct fM isomags. The ground state configuration with a multiplicity of M=12 corresponds to one of the four Mn moments aligned anti-parallel with the other three. Three of the four isomags contain an anti-aligned Mn moment in the Mn_3 plane. As expected from symmetry, they are equivalent in energy. The fourth isomag has the anti-aligned Mn moment at the apex of the bipyramid. This isomag lies 0.56 eV higher in energy than the in-plane isomags. A separate set of VDEs is calculated for each of the two distinct isomags, and those for the out-of-plane configuration are found to lie below the AEA. Hence, only VDEs for $M \pm 1$ transitions from the in-plane isomag (12→11 and 12→13) are plotted in Figure 5.3(b). The ground state VDEs and transitions to the first three excited states are shown along with the experimental PES in Figure 5.3(b). The ground state VDEs show excellent agreement with the two primary spectral peaks, the adiabatic electron affinity lies directly at the start of the spectra, and the excited

state values fall in the energy-window of the secondary features. Numerical values of these transitions are listed in Table 5.1.

5.1.4 $Mn_4O_2^-$

The final cluster in our study is $Mn_4O_2^-$. With increasing cluster size comes the potential for many more low-lying structures. Optimization yields a global minimum with $M = 2$. Unlike Mn_4O^-, the lowest-energy magnetic configuration is AFM, while the fM ($M = 12$) and FM ($M = 20$) arrangements are higher in energy by 0.63 and 1.20 eV, respectively (see Appendix I). The ground state structure of $Mn_4O_2^-$ (Figure 5.4(a)) is planar and resembles a Mn_2O^- dimer. The Mn-O bond distances, 1.82 Å and 1.84 Å, are close to that in Mn_2O^- (1.80 Å), and the cluster symmetry is C_{2h}. The presence of an additional oxygen reduces the overall cluster moment relative to Mn_4O^-. Nevertheless, the average Mn moment/atom is 4.83 μ_B, which is still close 5 μ_B. The anion with $M = 2$ has two anti-aligned moments and, hence, six possible spin configurations. Only three of these are non-degenerate, and the lowest-energy isomag is shown in Figure 5.4(a).

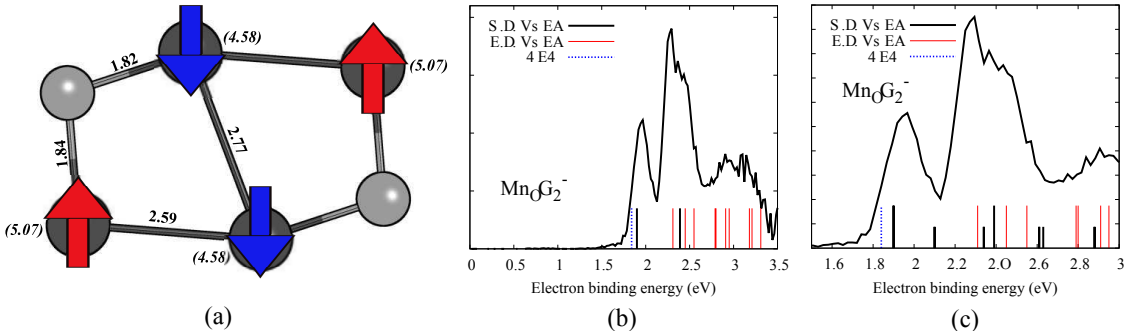

FIG. 5.4. (a) Ground-state structure of $Mn_4O_2^-$. (b) Experimental PES for $Mn_4O_2^-$ (solid line). VDEs for transitions from the ground-state anion to the fixed-geometry, ground-state neutral are shown as black lines, while transitions to the excited states of the fixed-geometry neutral are red. The dashed vertical line is the AEA. (c) Zoomed version of (b) which includes additional VDEs for five higher-energy isomags (shown as short lines).

In calculating the VDEs, we consider the $M \pm 1$ transitions $2 \rightarrow 1$ and $2 \rightarrow 3$. Theoretical VDEs are again plotted with experimental PES in Figure 5.4(b) and are listed in Table 5.1. The first two sharp peaks are in very good agreement with the ground state VDEs. Additional features in the second peak correspond to transitions from the ground state of the anion to the excited states of the neutral, though there are likely other contributions to the spectra at high electron binding energies.

5.2 Neutral Clusters and Adiabatic Electron Affinities

We have also optimized the geometries of the neutral clusters, again stepping through all possible multiplicities. The ground state magnetic ordering of both Mn_3O and Mn_3O_2 are fM with M=6. Mn_4O is also fM with M=11, while Mn_4O_2 is AFM with M=1. Just as with the anionic clusters, the neutral clusters have additional local minima corresponding to higher-energy isomers. The global minimum for each

TABLE 5.2. Adiabatic electron affinity for the transition "relaxed anion→relaxed neutral."

Cluster	Transition	AEA (eV)	Exp. (eV)[a]
Mn_3O	7→6	1.50	1.56
Mn_3O_2	5→6	1.29	1.22
Mn_4O	12→11	1.53	1.42
Mn_4O_2	2→1	1.84	1.56

[a]Experimental values are estimated from the onset of EBE intensity and have an uncertainty of ±0.100 eV.

is of greatest interest, as it allows calculation of the adiabatic electron affinity (AEA). This value can be estimated as the energy difference between the ground state of the anion and the ground state of the optimized neutral cluster. The AEAs for each cluster are shown in Table 5.2. The calculated AEAs correlate well with the onset of spectra features in the PES data.

The explicit consideration of different isomags presented for the anions is repeated for the neutral clusters. During the time-scale of a vertical transition, we expect the electronic state to relax, enabling spins to reorient. Hence, the final spin configuration of the neutral cluster may be different from the anion, regardless of whether its geometry is held fixed or allowed to relax. Very accurate VDEs and AEAs are achieved by applying our computational method to neutral clusters with fixed and relaxed geometries, respectively. The effect of spin relaxation on VDE energies is plotted in Figs. 5.1-5.4, where we include VDEs arising from transitions to higher-energy isomags of the neutral (shown as shortened black lines in subfigure (c)). The structures, multiplicities, and relative energies of these isomags are provided in Appendix I.

Mn_3O has three higher-energy isomags with unique energies (see Appendix I). Transitions to these isomags from the ground state of the anionic cluster have VDEs of 1.56, 1.63, and 1.84 eV. These are plotted together with the lowest-energy isomag

VDEs in Figure 5.1(c). The transition at 1.56 eV corresponds to a slight rise in intensity in the shoulder of the first peak, while the feature at 1.63 eV is very close to the ground state VDE given in Table 5.1. The 1.84 eV correlates well with broadening to the right of the first peak.

Likewise, Mn_3O_2 has three additional non-degenerate isomags (given in Appendix I), which are plotted in Figure 5.2(c). Their VDEs are 1.40, 1.62, and 1.82 eV. All three VDEs are below the apex of the first peak, contributing to low-energy features in the experimental PES spectra. In the Mn_4O cluster, there are four additional isomags (see Appendix I) to consider (Figure 5.3(c)). They correspond to VDEs of 1.58, 1.79, 1.98, and 2.19 eV. The effect of these transitions is a broadening of the low-energy shoulder and splitting of the first peak into three distinguishable sub-peaks. These effects are restricted to the low-energy regime; higher-energy features are still described by transitions to the ground state or excited states only.

Lastly, we find five higher-energy, non-degenerate isomags for Mn_4O_2 (see Appendix I). The additional VDEs (plotted in Figure 5.4(c)) are 2.10, 2.34, 2.61, 2.63, and 2.88 eV. This cluster is different from the other three in that none of the added VDEs lie below the ground-state values given in Table 5.1. Instead, they intermingle with the energies of the excited state VDEs and cause broadening predominately in the second and third peaks. The first peak rises sharply and appears to be dominated by transitions to the neutral ground state only.

For all four clusters considered, additional transitions to higher-energy neutral isomags correlate well with spectral broadening and with the presence of low-energy features at the onset of the spectra. Similar behavior is seen for Mn_2O, where the close energy of FM and AFM spin states causes vertical transitions from both isomers to coexist in the PES spectra.[17] As discussed by Khanna and coworkers, vertical transitions to higher-energy isomers or isomags may occur in the course of the experiment without contributing significantly to the spectra because of lower transition probability. Therefore, the extent of peak broadening depends on transition proba-

bility (which is not considered in this work) and the energy difference between the isomags. Nearly degenerate isomags, as in the case of Mn_3O, produce sharp, narrow peaks, while systems with widely-spaced isomags, such as Mn_4O, exhibit a gradual rise in PES intensity. Careful consideration of geometries and their different isomags is critical for accurate calculations of magnetic clusters.

6. PASSIVATED AL-ORGANOMETALLIC CLUSTERS*

6.1 Structure and Bonding

We first present results on the theoretical structure of aluminum complexes bound to cyclopentadienyl type ligands. In Table 6.1 we list the calculated B3LYP/6-31G(d,p) bond lengths for half-metallocene configurations of Al with Cp and related derivatives. In addition to providing insight into the individual Al-L bonding, these structures also form the protective outer layer on the larger aluminum clusters discussed below. The distance from the Al to the center of the Cp ring (Al-X) is given, along with the C-C bond length in the ring. The C-C bond lengths presented are averaged over all intra-ring carbons. The Al-ring center distances are obtained via perpendicular projection of Al onto the plane of the C_5 ring. The absolute difference between this projection and the ring center is defined as the ring slip. Our calculated slip values are then used to assign hapticities in accordance with the study of main-group half metallocenes by Budzelaar and coworkers[45]: η^5, 0 Å; η^3, 0.8 Å; η^2, 1.0 Å; η^1, $\geq$ 1.2 Å. Our calculated geometries for AlCp are in good agreement with other recent studies of main-group metallocenes, such as that by Rayon and Frenking.[50] In addition, we consider three substituted Cp derivatives; nitro-Cp ($C_5H_4NO_2$), trifluoromethyl-Cp* ($C_5Me_4CF_3$), and pentatrifluoromethyl-Cp* ($C_5[CF_3]_5$). The substituted Cp ligands allow us to examine the M-L bond strength with various electron withdrawing groups that may also serve as oxidizers for the aluminum complexes during thermal decomposition. All substituted Cp ligands result in only slight shifts of the Al (< 0.06 Å) and essentially retain the η^5 configuration of standard AlCp. The Al-ring distance increases slightly with the ad-

*Reprinted with permission from "Structure, thermodynamics, and energy content of aluminum-cyclopentadienyl clusters" by K. S. Williams and J. P. Hooper, The Journal of Physical Chemistry A **115**, 14100 (2011). Copyright 2011 American Chemical Society. Direct link: http://dx.doi.org/10.1021/jp207292t.

TABLE 6.1. Calculated bond lengths and distances of half-metallocene complexes. Average slip and ligand hapticity are calculated by perpendicular projection of Al atoms onto the Cp-type rings. Al-X distances are only calculated for species with η^5 bonding.

Cluster	C-C bond length (Å)	Al-X distance (Å)	Slip (Å)	Hapticity
AlCp	1.420	2.064	0.002	η^5
Ref. 54	1.409	2.039		
Ref. 55	1.420	2.037		
Ref. 50	1.428	2.059		
Ref. 45		2.06		
Ref. 56		2.05		
$AlCp^*$	1.429	2.021	0.000	η^5
Ref. 55	1.498	1.989		
Ref. 96[a]	1.414	2.063		
$AlC_5H_4NO_2$	1.417	2.116	0.003	η^5
$AlC_5Me_4CF_3$	1.428	2.053	0.058	η^5
$AlC_5[CF_3]_5$	1.425	2.216	0.031	η^5

[a]Experimental data.

dition of electron withdrawing groups to the Cp ring; further discussion of the M-L bond changes in these substituted complexes is given below.

We next consider larger clusters composed of an AlCp or $AlCp^*$ shell surrounding an aluminum core. As our ultimate interest is in materials with a significant mass fraction of combustible aluminum, our focus is on the larger, experimentally observed $Al_{50}Cp^*_{12}$ cluster and related compounds that help to clarify its properties. Table 6.2 contains averaged bond lengths and distances for each optimized structure along with previous experimental and theoretical values where available. Figures 6.1, 6.2, and 6.3 show the calculated geometries of the complexes. Of the compounds listed, only $Al_4Cp^*_4$, $AlCp_3$, $AlCp^*_3$, and $Al_{50}Cp^*_{12}$ have characterized solid-state structures. $Al_8Cp^*_4$ is observed in laser desorption mass spectrometry of solid-state $Al_4Cp^*_4$ and represents an intermediate between the tetramer and the large Al_{50} complex.[97] The remaining compounds in Table 6.2 are part of a reaction

scheme proposed by Schnöckel and coworkers to explain the formation and stability of the large aluminum clusters.[57] All of our calculated values agree with available previous results to within 0.1 Å. Furthermore, the QM:MM multilayer calculation on the largest cluster does quite well in reproducing the geometry obtained using full B3LYP; the C-C intra-ring distances are identical, and the Al-X distance is within 0.06 Å. The calculated Al-ring distances in $Al_{50}Cp^*_{12}$ are slightly larger than experiment due to the lack of a condensed phase environment in the calculation. The hapticity of the M-L bonds in these compounds is generally η^5, with two exceptions. The first is the $AlCp_3$ and $AlCp^*_3$ systems, which contain trivalent aluminum and exhibit significant steric interaction between the ligands (see Figure 6.2). The second is the $Al_{50}Cp_{12}$ cluster with its unmethylated ligands, in which eight of the twelve binding ligands shift to an η^1 position (Figure 6.3). In systems with mixed hapticities, all bonding configurations are listed in Table 6.2.

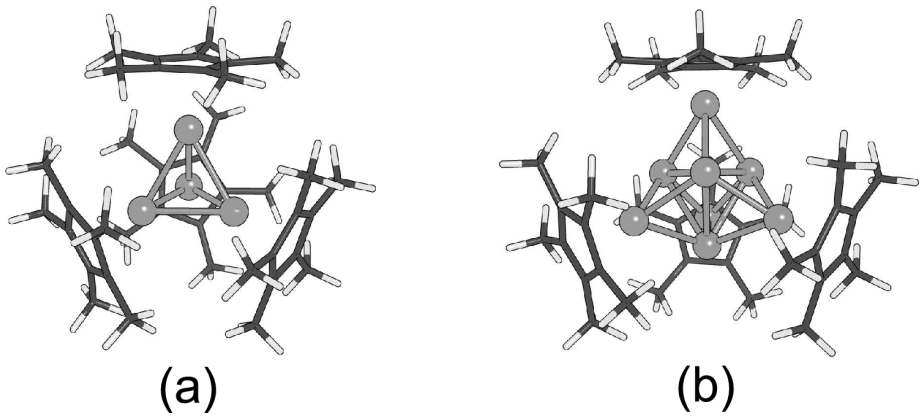

FIG. 6.1. Calculated structures of (a) $Al_4Cp^*_4$ and (b) $Al_8Cp^*_4$.

In Table 6.3 we list average cluster spacings, with the larger clusters broken up into cages to examine how the bond lengths change in the interior regions. The interior Al_8 core of the $Al_8Cp_4/Al_8Cp^*_4$ clusters is broken into two cages: an innermost tetrahedral Al_4 shell and the four exterior Al_4 units that cap its faces. Bond lengths

TABLE 6.2. Calculated average bond lengths and distances of larger Al-Cp clusters.

Cluster	C-C bond length (Å)	Al-X distance (Å)	Slip (Å)	Hapticity
$AlCp_3$	1.424	–	1.083	η^2
			1.546	η^1
			1.738	η^1
$AlCp_3^*$	1.439	–	0.958	η^2
			2.168	η^1
			2.318	η^1
Al_4Cp_4	1.420	2.072	0.003	η^5
Ref. 54	1.408	2.056		
Ref. 55	1.408			
Ref. 56		2.06		
Ref. 53	1.429	2.052		
$Al_4Cp_4^*$	1.428	2.073	0.033	η^5
Ref. 53[a]	1.437	2.059		
Ref. 52[a]		2.015		
Al_8Cp_4	1.421	2.000	0.006	η^5
$Al_8Cp_4^*$	1.432	1.956	0.005	η^5
$Al_{50}Cp_{12}$	1.442	–	1.231	η^1
	1.437	1.992	0.00	η^5
$Al_{50}Cp_{12}^*$	1.429	2.064	0.209	η^5
QM:MM[b]	1.429	2.121		
Ref. 36[a]	1.421	1.981		

[a]Experimental data.

[b]QM:MM refers to geometry optimization with the multilayer method B3LYP/6-31g(d,p):UFF.

TABLE 6.3. Average distances between Al atoms located in the interior cages of the clusters. Experimental values given in italics.

Cluster	Cage	Al-Al distance (Å)
Al_4	Al_4	2.795
Al_4Cp_4	Al_4	2.764
$Al_4Cp^*_4$	Al_4	2.869 (*2.767*)[a]
Al_8Cp_4	Al_4 shell	2.788
	Al_4 caps	2.675
$Al_8Cp^*_4$	Al_4 shell	2.805
	Al_4 caps	2.673
$Al_{50}Cp_{12}$	Al_8 shell	2.69
	Al_{30}-Al_{12}	2.812 (η^1) 3.041 (η^5)
	Diameter	15.314
$Al_{50}Cp^*_{12}$	Al_8 shell	2.690 (*2.664*)[a]
	Al_{30}-Al_{12}	2.947 (*2.867*)[a]
	Diameter	15.241 (*14.896*)[a]

[a]Reference 36.

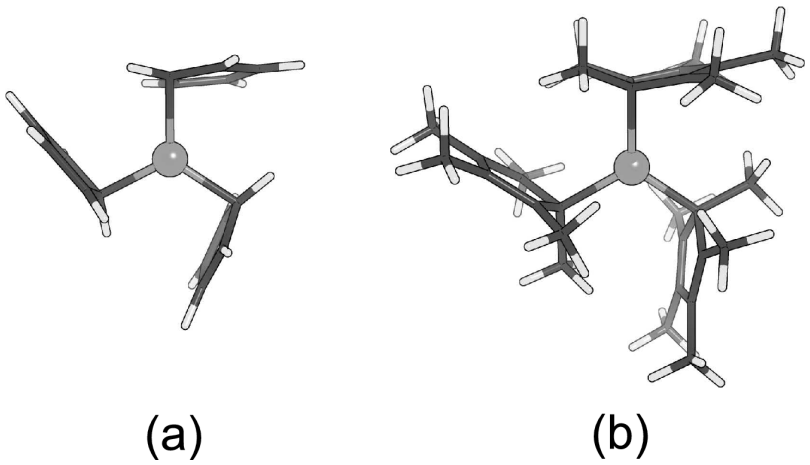

FIG. 6.2. Comparison of groundstate geometries of (a) $AlCp_3$ and (b) $AlCp^*_3$. The symmetry of the Cp^* ring is broken in (b), as the methyl groups bend out of the ring plane due to the significant steric hindrance.

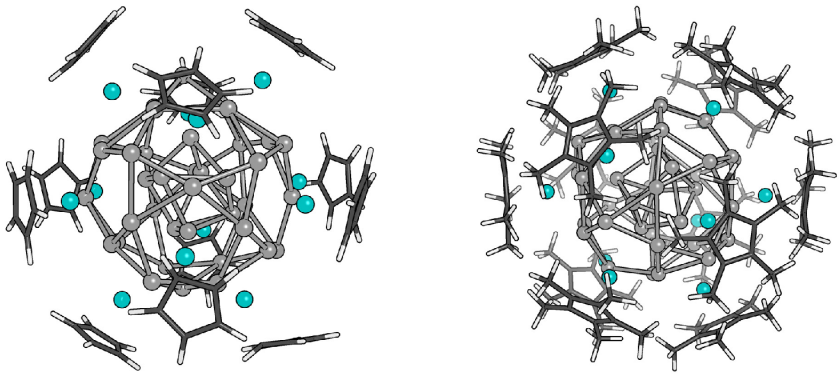

FIG. 6.3. Calculated structures of $Al_{50}Cp_{12}$ (left) and $Al_{50}Cp^*_{12}$ (right). Surface aluminum atoms directly involved in organometallic bonding are shown in teal.

in the innermost Al_4 shells are longer than in the Al_4 exterior tetrahedral caps, regardless of the choice of ligand. The effect of substituting Cp^* for Cp is the same as in the smaller Al_4 cluster; Cp^* slightly increases the average Al-Al bond length in the innermost shell.

The large $Al_{50}Cp^*_{12}$ cluster has been discussed in a number of papers by Schnöckel and coworkers.[36,40] Our calculated structure for this compound is given in Figure 6.3, along with the theoretical geometry of the unmethylated (and experimentally unobserved) analog $Al_{50}Cp_{12}$. Both compounds are divided into the following pieces: an inner Al_8 shell, an exterior Al_{12} shell which is shown in teal and consists of the Al atoms bound directly to ligands, and a final Al_{30} shell between these. As noted above, eight of the twelve ligands in the $Al_{50}Cp_{12}$ system change hapticity (shown in Figure 6.4). Bonds in the Al_8 interior shells are shorter than those connecting the Al_{30} and Al_{12} shells, which is opposite the behavior seen in the smaller Al_4 and Al_8 clusters. All of our calculated averages agree with experimental results for the $Al_{50}Cp^*_{12}$ solid state structure, including the effective cluster diameter. This is defined as twice the radius, with the radius being the average distance from the cluster center to the plane of the Cp^* ring. The innermost Al_8 cluster of $Al_{50}Cp^*_{12}$ is shown in Figure 6.5, along with the Al_8 core of $Al_8Cp^*_4$ and an isolated Al_8 cluster. The latter is in agreement with previous calculations of small aluminum clusters by Rao and Jena.[98] Al atoms in both of the organometallic clusters (b & c) arrange differently than in the bare cluster; the interior Al core of $Al_{50}Cp_{12}$ is similar to that in the methylated version (c) as well, and both have significantly lowered symmetry compared to an isolated cluster (a). Very recent work by Schnöckel and coworkers provides some additional discussion on the asymmetry of the Al_8 core in relation to recently synthesized organometallic gold clusters.[99]

We next consider in more detail the nature of the metal-ligand bond in Al-Cp complexes. It is instructive to examine the simple AlCp half-metallocene, as all the Al-Cp bonds in larger systems considered here display similar features. While AlCp ostensibly follows an octet rule (5 e^- from Cp and 3 e^- from Al), electron counting heuristics are generally a poor guide to main-group metallocene compounds.[44] Instead, we consider directly the bonding molecular orbitals (MOs) and fragment interaction. Similar to previous treatments, we separate the system into Al^+ and Cp^-

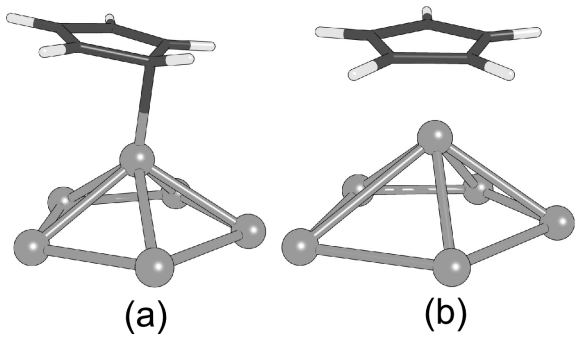

FIG. 6.4. The two bonding motifs at the $Al_{50}Cp_{12}$ surface; (a) η^1 and (b) η^5.

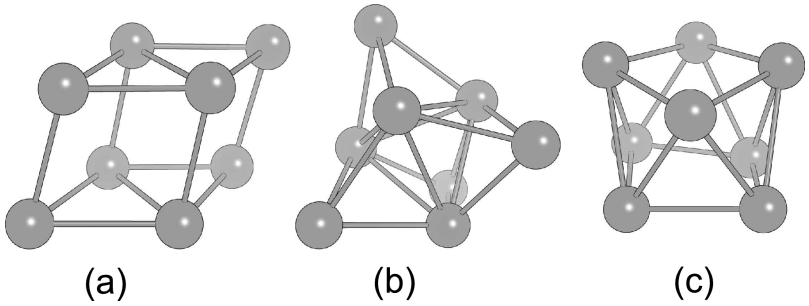

FIG. 6.5. (a) The groundstate geometry of the neutral, bare Al_8 cluster; (b) the Al_8 core of $Al_8Cp^*_4$; (c) the distorted Al_8 core of $Al_{50}Cp^*_{12}$.

fragments. This is consistent with the energy decomposition analysis of Rayon and Frenking[50] and the study of Budzelaar and coworkers[45] examining the basic AlCp half-metallocene; both conclude that the character of the AlCp bond is predominantly ionic. It is also consistent with the NBO partial charges observed on all our η^5 compounds (see below for more discussion).

Four orbitals, three of which are shown in Figure 6.6, comprise the majority of the bonding character in AlCp. The a_1 Cp orbital bonds with one *sp* from the aluminum, with the non-bonded lone-pair residing in the remaining *sp*, which is

also the HOMO. The two filled e_1 orbitals on Cp form two degenerate bonding orbitals with two unfilled aluminum p orbitals. The surface Al-ligand units in larger clusters also bond via analogous MOs; an example is shown for the Al_4Cp_4 system in Figure 6.7, in which favorable overlap of the Al sp orbitals gives rise to a weak bonding in the inner aluminum tetrahedron.

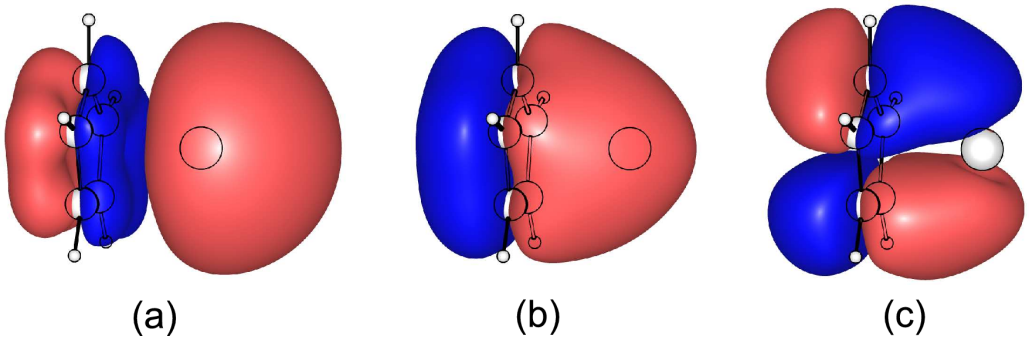

FIG. 6.6. Three relevant bonding MOs for AlCp: (a) the HOMO, which consists of the non-bonding interaction between the Cp a_1 and the Al sp; (b) the HOMO-7, showing the Cp a_1 bonding interaction with Al sp; (c) The HOMO-1, showing overlap between the Al p and the Cp e_1.

To get a quantitative sense of the contribution from different orbitals, we perform a charge decomposition analysis (CDA)[100] to examine the charge donation from the ligand to the Al^+. CDA constructs the wave function of the M-L compound in terms of the linear combination of the donor and acceptor fragment orbitals. Each molecule is decomposed into closed-shell fragments corresponding to the Al^+ (denoted M) and the ligand anion (denoted L).

The bonding in each orbital can be characterized by three terms: L $\rightarrow$ M charge donation, M $\rightarrow$ L back donation, and charge polarization (or mixing of the occupied orbitals of both M and L). The results of CDA analysis on five Al metallocenes with various functional groups on the Cp ligand are given in Table 6.4. The columns of Table 6.4 contain the relative amount of donation (d) and charge repulsion (r), or

TABLE 6.4. CDA results for the bonding orbitals of half-sandwich Al metallocenes with various Cp derivatives. The columns are forward electron donation (d) and charge repulsion (r).

	AlCp		AlCp*		$AlC_5H_4NO_2$		$AlC_5Me_4CF_3$		$AlC_5[CF_3]_5$	
Orbital	d	r	d	r	d	r	d	r	d	r
Al sp non-bonded	0.359	-1.655	0.388	-1.736	0.312	-1.571	0.357	-1.675	0.205	-1.424
Cp $e_1 \cdots$ Al p_x	0.530	-0.004	0.455	-0.004	0.481	-0.003	0.427	-0.004	0.316	-0.002
Cp $e_1 \cdots$ Al p_y	0.531	-0.004	0.455	-0.004	0.397	-0.012	0.432	-0.022	0.328	-0.002
Cp $a_1 \cdots$ Al sp	0.187	0.552	0.087	0.214	0.188	0.483	0.086	0.173	0.125	0.348
Total (all orbitals)	1.892	-1.046	1.876	-1.146	1.643	-1.002	1.773	-1.119	1.347	-0.922

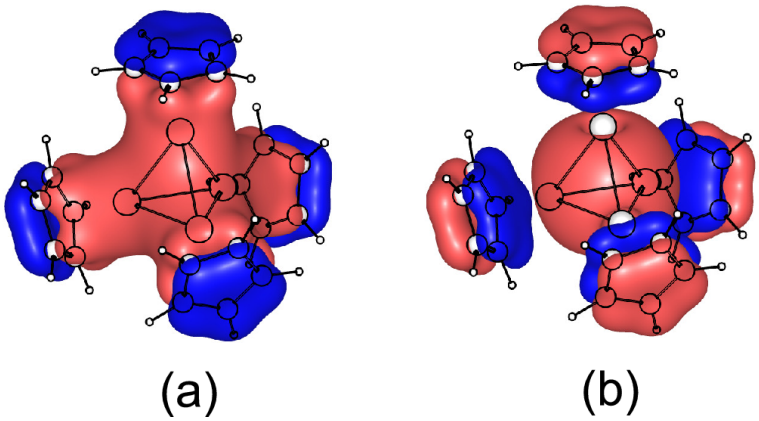

FIG. 6.7. Bonding MOs for Al_4Cp_4, showing favorable overlap of the half-metallocene MOs leading to bonding in the interior Al tetramer.

polarization, in each molecule. There are small negative values (on the order of -0.15) for the back donation, which likely arise from small repulsion effects that are also included in the methodology for calculating this term.[100] In the ionic configuration studied, we expect no true back-bonding such as occurs in typical transition metal metallocenes; thus, this quantity is not listed in Table 6.4. Actual charge values from the CDA analysis are not important,[100] and we focus instead on the relative amounts of forward donation and repulsion.

The CDA analysis suggests that the bonding character can be viewed as a balance between forward donation into the aluminum p orbitals and repulsion from polarization effects. In the simple case of AlCp, the former arises primarily from donation from the Cp e_1 to Al p and the latter mainly from repulsion between the Al lone pair and the Cp a_1. All other functionalized AlCp complexes are also dominated by orbitals that are analogous to the four bonding orbitals of bare AlCp. Table 6.4 lists the contributions from each of these orbitals as well as the total values of donation and repulsion.

For all variants listed in Table 6.4, the primary repulsive contribution arises from the HOMO, which contains the nonbonding Al *sp*. In the CDA analysis, negative values of r generally correspond to charge moving away from the bonding region between the donor and acceptor fragments. Similarly, a positive sign indicates an accumulation of charge in the same region. Approximately 50-55% of the total charge donated from the ligand to the metal is from orbitals analogous to the Cp e_1. The Al *sp* with a bonding overlap with the Cp a_1 generally contains a small amount of forward donation and a positive repulsion term. For the compounds with methyl type groups off the ligand ($AlCp^*$ and the fluorinated variants), there is also a small contribution from the sp^3 orbitals on the methyl carbons.

Comparing $AlCp^*$ to AlCp, we note that the presence of the additional methyl groups lowers the forward donation from the e_1 orbitals, though there is additional donation from the methyl carbons as mentioned previously. There is a slight increase in repulsive polarization with the non-bonding Al *sp*, but overall there is little difference between Cp and Cp^* in terms of donor/acceptor interactions. The remaining Cp derivatives all contain electron withdrawing groups, which lower both the donation and repulsion terms and also result in slightly increased Al-ring bond lengths as compared to Cp and Cp^* (see Table 6.1). The reduction in forward donation is the more dominant effect based on the CDA analysis. The effects of the substituents on the bond strength can also be qualitatively understood in terms of forward donation and repulsion. In $AlC_5[CF_3]_5$, for example, the electron withdrawing groups reduce both the forward donation and the repulsive polarization. These effects largely balance, giving an aluminum-ligand bond strength very similar to that of the basic AlCp system.

For making comparisons among the different molecules and clusters, the natural bond orbital (NBO) partial charges are given in Table 6.5. Also included in Table 6.5 are the NBO charges normalized to the value for AlCp. Partial charges are not generally good indicators of valence,[44] but we do see a general trend that

TABLE 6.5. NBO partial charges on the Al atoms bound to ligand groups and HOMO-LUMO gaps for all clusters. Charges for clusters with multiple Al atoms are averaged over all Al atoms participating in metal-ligand bonds (i.e., 4 atoms for $Al_4Cp^*_4$, 4 for $Al_8Cp^*_4$, and 12 for $Al_{50}Cp^*_{12}$).

Molecule	q (NBO)	q / q(AlCp)	Gap (eV)
AlCp	0.630[a]	1.00	5.72
$AlCp^*$	0.657	1.04	5.49
$AlC_5H_4NO_2$	0.700	1.11	4.46
$AlC_5Me_4CF_3$	0.689	1.09	5.57
$AlC_5[CF_3]_5$	0.774	1.23	6.14
$AlCp_3$	1.870	2.97	4.21
$AlCp^*_3$	1.908	3.03	4.61
Al_4Cp_4	0.591	0.94	4.61
$Al_4Cp^*_4$	0.641	1.02	4.36
Al_8Cp_4	0.693	1.10	2.99
$Al_8Cp^*_4$	0.760	1.21	3.12
$Al_{50}Cp_{12}$	0.724 (η^1)	1.15 (η^1)	1.43
	0.901 (η^5)	1.43 (η^5)	
$Al_{50}Cp^*_{12}$	0.913	1.45	1.57

[a]A previous NBO atomic partial charge of 0.61 was reported (Refs. 50 and 51).

the trivalent $AlCp_3$ complexes have a partial charge three times that of the isolated metallocene, and the Al atoms bound to Cp/Cp^* in the Al_{50} clusters have an intermediate charge between these. The HOMO-LUMO gap is also listed in Table 6.5, and we observe a steady decrease in the gap energy with increasing cluster size. $Al_4Cp^*_4$ has a value typical of insulators at 4.36 eV. Increasing the cluster size to 8 Al atoms decreases the HOMO-LUMO gap to 3.12 eV, and the largest Al_{50} systems are approaching semiconducting values at 1.43 and 1.57 eV. Very recently Lopez-Acevedo and coworkers[101] and Clayborne and coworkers[102] have reported on aluminum as well as gold and gallium clusters, in the context of superatom models. Their partial charges and HOMO-LUMO gaps are consistent with the results presented here.

To analyze the relative bonding strength and possible unimolecular decomposition pathways in the systems, we next consider the bond dissociation energies (BDEs), defined as the reaction energy D_e for homolytic cleavage of the listed bond. The BDE adjusted with a zero-point correction (D_0) and the Gibbs free energy change of the reaction ΔG^0 at 298K and 1 atm are also listed. BDEs for the half metallocene complexes are given in Table 6.6 and those of larger clusters are given in Table 6.7. The substituted Cp derivatives all lower the BDE as compared to AlCp, though the largest effect (for the Cp^* with a single methyl replaced by a fluoro group) only reduces the bond strength by 13%. Possible substitutions with oxidizing groups thus does not radically change the basic monovalent bond with aluminum, but naturally there may be significant differences in terms of solvent effects or unintended oxidation of the aluminum clusters.

We next discuss the Al_4 clusters shown in Table 6.7. The BDE associated with removing one Cp ligand from Al_4Cp_4 is 62.60 kcal/mol, while the tetramerization energy is 16.09 kcal/mol. This implies that the M-L bond is much stronger than the Al-Al bonds, as would be expected. The same is true for $Al_4Cp^*_4$, where the M-L BDE of 44.89 kcal/mol is much higher than the tetramerization energy of 9.09 kcal/mol. Previous calculations by Huber and Schnöckel using BP86 and an SVP ba-

TABLE 6.6. Bond dissociation energies for several reactions involving half-metallocene complexes. D_e is calculated using only the DFT electronic energies, while D_0 includes a zero-point correction. ΔG^0 is defined as the Gibbs free energy of the reaction at 298 K and 1 atm.

Eq.	BDE reaction	D_e (kcal/mol)	D_0 (kcal/mol)	ΔG^0 (kcal/mol)
I	$Al_4 \longrightarrow 4Al\cdot$	107.30	105.89	88.11
II	$AlCp \longrightarrow Al\cdot + Cp\cdot$	85.87	82.47	73.83
III	$AlCp^* \longrightarrow Al\cdot + [Cp^*]\cdot$	76.81	74.13	65.58
IV	$AlC_5H_4NO_2 \longrightarrow Al\cdot + [C_5H_4NO_2]\cdot$	81.53	79.08	70.36
V	$AlC_5Me_4CF_3 \longrightarrow Al\cdot + [C_5Me_4CF_3]\cdot$	74.53	72.25	62.54
VI	$AlC_5[CF_3]_5 \longrightarrow Al\cdot + [C_5[CF_3]_5]\cdot$	84.60	82.65	72.98

TABLE 6.7. Bond dissociation energies for several reactions involving aluminum- cyclopentadienyl complexes and clusters.

Eq.	BDE reaction	D_e (kcal/mol)	D_0 (kcal/mol)	ΔG^0 (kcal/mol)
VII	$AlCp_3 \longrightarrow Cp_2Al\cdot + Cp\cdot$	61.02	57.50	43.58
VIII	$AlCp^*_3 \longrightarrow Cp^*_2Al\cdot + [Cp^*]\cdot$	28.59	24.96	10.07
IX	$Al_4Cp_4 \longrightarrow Cp_3Al_4\cdot + Cp\cdot$	62.60	59.67	48.91
X	$Al_4Cp^*_4 \longrightarrow Cp^*_3Al_4\cdot + [Cp^*]\cdot$	44.89	41.30	24.75
XI	$Al_4Cp_4 \longrightarrow 4AlCp$	16.09	15.04	-17.75
XII	$Al_4Cp^*_4 \longrightarrow 4AlCp^*$	9.09	7.39	-35.14
XIII	$Al_8Cp_4 \longrightarrow Cp_3Al_8\cdot + Cp\cdot$	54.88	51.58	39.08
XIV	$Al_8Cp_4 \longrightarrow Cp_3Al_7 + AlCp$	32.37	31.03	17.36
XV	$Al_8Cp^*_4 \longrightarrow Cp^*_3Al_8\cdot + [Cp^*]\cdot$	47.52	44.47	28.49
XVI	$Al_8Cp^*_4 \longrightarrow Cp^*_3Al_7 + AlCp^*$	37.39	37.69	18.43
XVII	$Al_{50}Cp_{12} \longrightarrow Cp_{11}Al_{50}\cdot + [Cp]\cdot$	53.76	–	–
XVIII	$Al_{50}Cp_{12} \longrightarrow Cp_{11}Al_{49}\cdot + AlCp$	28.61	–	–
XIX	$Al_{50}Cp^*_{12} \longrightarrow Cp^*_{11}Al_{50}\cdot + [Cp^*]\cdot$	79.72	–	–
XX	$Al_{50}Cp^*_{12} \longrightarrow Cp^*_{11}Al_{49}\cdot + AlCp^*$	58.30	–	–

sis set also showed that Al_4Cp_4 is more stable against decomposition into monomers than $Al_4Cp^*_4$.[53] The experimentally estimated value for the tetramerization energy in solution based on ^{27}Al NMR is approximately 36 kcal/mol;[52] we note that the gas phase energy barrier is expected to be lower than the condensed phase value due to solvent and steric effects; thus, it is difficult to directly compare tetramerization energies with the NMR estimate.

We note that no stable structure was found computationally for Al_3Cp_3 following removal of a full AlCp unit. The favored decomposition pathway will be dissociation into four AlCp or AlCp* monomers. This is further supported by the ΔG^0 values given in column four of Table 6.7. ΔG^0 is negative for Eqs. XI and XII, indicating that the barrier to decomposition of the isolated cluster at ambient conditions is minimal. We thus expect that $Al_4Cp^*_4$ will depend very heavily on steric interactions with the solvent or adjacent clusters for its stability.

We next consider M-L bond strength in the larger Al_8 clusters. The trends are similar; namely, the BDE to remove one Cp ligand from Al_8Cp_4 is 54.88 kcal/mol, while the BDE for removal of an entire AlCp monomer is 32.37 kcal/mol. The relative difference between the two is not as large as in the Al_4Cp_4 cluster, but the trend is the same. Also, the M-L BDE of $Al_8Cp^*_4$ is 47.52 kcal/mol, which is again slightly larger than the monomer BDE of 37.39 kcal/mol. For the largest cluster, $Al_{50}Cp^*_{12}$, we consider only D_e for computational efficiency. The BDE for the M-M bond between Al atoms in the Al_{38} shell and the Al_{12} shell is only 58.30 kcal/mol compared with the M-L bond BDE of 79.72 kcal/mol.

Lastly, we comment on the general behavior of the M-L bond. First, the strength of the M-L BDE of surface AlCp units remains generally constant with cluster size. In fact, the BDE associated with breaking the η^5 bond in AlCp* is 76.81 kcal/mol, which is almost equal to the M-L BDE in the largest cluster, at 79.72 kcal/mol. Thus while the M-L bond is slightly weaker in the smaller Al_4 and Al_8 clusters, it has a strength in the largest cluster comparable to that of the monomer. The M-L bond is

generally stronger than other aluminum bonding, and it is likely that for all clusters larger than the tetramer the initial unimolecular thermal decomposition step is the removal of AlCp or AlCp* units. Second, functionalizing the Cp ligand reduces the M-L bond strength in comparison to Cp, regardless of cluster size or bond type (η^5 or η^1). The effect is smaller in the half-metallocenes, but in the larger clusters the M-L bonds with Cp* are approximately 33% weaker than those with Cp.

6.2 Steric Hindrance

We next briefly consider the steric interactions between the ligand groups in the various clusters. We expect that the ligand bulkiness will play a key role in determining the stability of these compounds against oxidation at atmospheric conditions. It also will have a significant effect on the packing density (and hence the combustion energy density) of these clusters in the solid state, as well as altering the interaction with solvents during crystallization.

To assess the ligand bulkiness and the energy barriers governing steric hindrance between the ligands, we calculate the total energy versus ring slip in the Cp/Cp* clusters. The coordinate for ring slip (Ref. 45) is the same as that defined in the previous section. Each slip step corresponds to a 0.5 Å movement of the ligand along the ring slip coordinate, while all other atoms are kept fixed. The 0 Å step begins with the B3LYP optimized geometry, and the energies of subsequent steps result from single-point calculations on the slipped systems. Figure 6.8 shows energy versus ring slip for the smaller clusters. The methyl groups provide a significant increase in repulsion between adjacent ligands as compared to the non-methylated Cp. The lone AlCp monomer shows significantly higher energy increases with Cp ligand slip as compared to Al_4Cp_4 and Al_8Cp_4 due to a lower M-L bond strength and charge migration to the central Al core in the larger clusters.

The ring slip for the large Al_{50} clusters is shown in Figure 6.9. For the unmethylated $Al_{50}Cp_{12}$, we consider two structures; first, the cluster in which all ligand groups

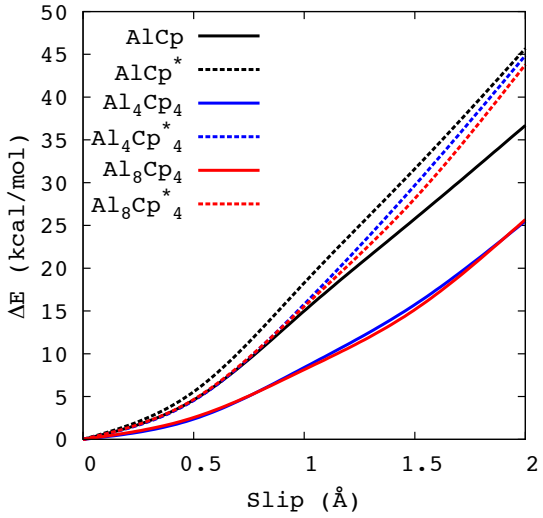

FIG. 6.8. The energy change for smaller clusters as a function of slipping the Cp ligand perpendicular to the Al-η^5 axis.

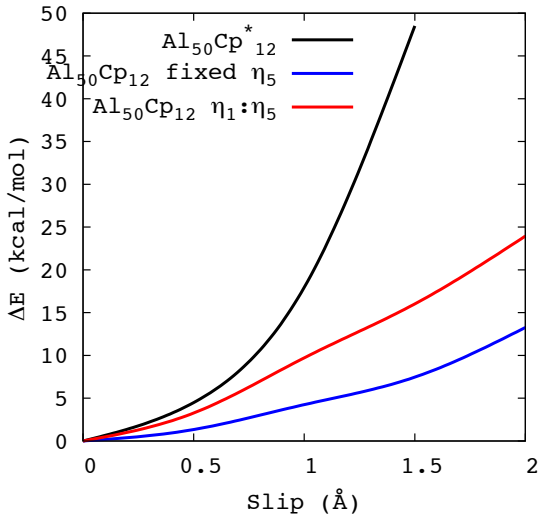

FIG. 6.9. The energy change for ring slippage in the large Al_{50} clusters.

retain an η^5 bonding as in $Al_{50}Cp^*_{12}$ (denoted as "fixed η_5"), and second the fully relaxed geometry in which eight of the ligands slip to an η^1 configuration (denoted "$\eta_1 : \eta_5$"). The slip values in the latter case are for one of the four ligands remaining in an η^5 bonding. As expected, the large methylated cluster shows significant steric hindrance with slippage, well above that of the unmethylated clusters. Allowing the $Al_{50}Cp_{12}$ ligands to relax into η^1 configurations increases the steric hindrance, suggesting that the mixture of hapticities observed in $Al_{50}Cp_{12}$ may arise largely from ligand steric effects.

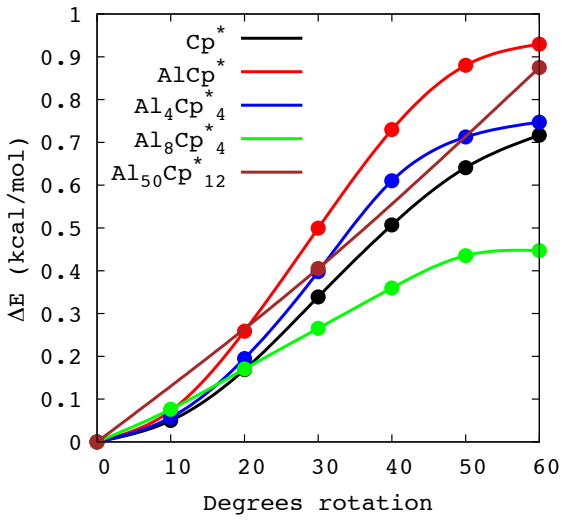

FIG. 6.10. Energy barrier to methyl group rotation on the Cp* ligands of several Al-η^5 clusters.

The methyl groups in the Cp* ligands add significant steric interaction during ring slippage, but we expect them to generally behave as weakly hindered rotors in the isolated equilibrium cluster configuration. Figure 6.10 displays the energy barrier required to rotate one methyl group by 60° (half of the symmetry-equivalent rotation of 120°). The points along each curve correspond to B3LYP single-point calculations in which a single methyl group is rotated in 10° steps while all other atoms are again

kept fixed. The hindrance is indeed very low; every cluster, regardless of size, has an energy barrier to methyl rotation that is less than 1 kcal/mol. This insensitivity to methyl position justifies our use of the multilayer QM:MM method for geometry optimization which uses UFF for the methyl groups in the largest cluster. Though these groups should properly be treated as free or hindered rotors, their contribution to the partition function of this large cluster is extremely small and thus for simplicity we continue to treat them as vibrations in the thermochemistry calculations discussed below.

6.3 Thermodynamics

We next consider the thermochemistry of these compounds, with particular focus on their energy content for propellant and energetic material applications. The standard enthalpies of formation, ΔH_f^0, are shown in Table 6.8. For smaller clusters G2 calculations were also run to confirm the validity of the B3LYP/6-31G(d,p) basis set in predicting heats of formation (HOFs). Both the B3LYP and G2 values for AlCp (56.94 kcal/mol and 50.20 kcal/mol, respectively) are close to the previously reported theoretical value of 49.4 kcal/mol.[50] The B3LYP heats of formation generally tend to uniformly be slightly larger than the G2 value, as do the B3LYP calculations taken at the B3LYP:UFF geometry. Further discussion about the accuracy of theoretical HOFs for organometallics is given in Appendix II.

For the largest cluster, $Al_{50}Cp^*_{12}$, we calculated the geometry of the structure by performing a QM:MM calculation using a multilayer ONIOM method as discussed above. The lower ONIOM layer contains the methyl groups treated with UFF, while the Al core and Al-η^5 bonded atoms are treated with B3LYP/6-31G(d,p). Energy differences for the atomization reactions are derived from a full DFT calculation; only the initial geometries are taken from the more computationally efficient QM:MM approach. As discussed above, the overall partition functions are not sensitive to the details of the bulky methyl groups, and separating the system results in significantly

TABLE 6.8. Standard enthalpies of formation calculated using B3LYP/6-31g(d,p), G2, and B3LYP/6-31g(d,p) at the B3LYP:UFF geometry.

Cluster	ΔH_f^0 (kcal/mol)		
	B3LYP	G2	B3LYP:UFF
Al_4 cluster	207.48	178.37	
Cp^-	37.21	34.99	
$[Cp^*]^-$	-5.25		
$AlCp$[a]	56.94	50.20	
$AlCp^*$	17.51	10.70	16.58
$AlC_5H_4NO_2$	54.84		
$AlC_5Me_4CF_3$	-139.13		
$AlC_5[CF_3]_5$	-739.61		
$AlCp_3$	114.72		
$AlCp_3^*$	23.58		
Al_4Cp_4	214.26		
$Al_4Cp_4^*$	61.69		61.68
Al_8Cp_4	341.91		
$Al_8Cp_4^*$	169.62		175.29
$Al_{50}Cp_{12}$	1680		
$Al_{50}Cp_{12}^*$			1426

[a]A previous calculated value of 49.4 kcal/mol is given in Ref. 50.

improved computational times. Similar calculations for $AlCp^*$, $Al_4Cp^*_4$, and $Al_8Cp^*_4$ in Table 6.8 yield results very close to full DFT and G2 calculations.

We next consider a reaction scheme proposed by Schnöckel and coworkers as an explanation for why $Al_4Cp^*_4$ is sufficiently stable to persist in solution and solid state form, but Al_4Cp_4 is not. They hypothesize that the large Al_{50} clusters serve as a barrier state that the tetramers must pass through before decomposition into a pure metallic phase. The presence of this barrier is suggested to "trap" the tetramer complexes on their way to metallization. These authors (Ref. 57) present an energy level diagram in which the energy change for an idealized reaction taking Al_4Cp_4 to $Al_{50}Cp_{12}$ and $AlCp_3$ is slightly negative, whereas the analogous reaction in the methylated system is strongly positive. There is not sufficient information to reproduce previous energy calculations (Ref. 57), as no details are given on the calculated structures, enthalpies of formation, or if the energies are corrected from the bare DFT SCF energy to account for thermal effects. In Table 6.9 we present our values for the reaction enthalpies in the proposed mechanism, along with the previous values (Ref. 57). ΔH^0_{rxn} is defined as

$$\Delta H^0_{rxn} = \Delta H^0_f(\text{products}) - \Delta H^0_f(\text{reactants}). \tag{6.1}$$

All values of ΔH^0_f for the gaseous components (denoted as (g)) are taken from Table 6.8, and equations involving solid aluminum (denoted Al(s)) are adjusted by an amount equal to the standard enthalpy of vaporization of Al.

A visual diagram of our calculated enthalpies of reaction is given in Figure 6.11. The structure of our energy diagram is mirrored after that proposed by Huber *et al.* (Ref. 57), but we find a different trend for the $Al_{50}Cp_{12}$ cluster. Our calculations give a positive ΔH^0_{rxn} of 163.7 kcal/mol for the disproportionation reaction Al_4Cp_4 (g) $\longrightarrow$ $Al_{50}Cp_{12}$(g) + $AlCp_3$(g). In contrast with previous work, the Al_{50} structures are "barrier" states in both the methylated and unmethylated systems, though we do find that this barrier is lower for the Cp clusters than in the Cp^*. Additionally,

TABLE 6.9. Reactions involved in the proposed stabilization mechanism in Ref. 57.

Reaction	ΔH^0_{rxn}(kcal/mol)	Ref. 57(kcal/mol)
$Al_{50}Cp^*_{12}(g) + 19AlCp^*_3(g) \longrightarrow 46Al(s) + 23AlCp^*_3(g)$	-932.3	-473.9
$17.25Al_4Cp^*_4(g) \longrightarrow Al_{50}Cp^*_{12}(g) + 19AlCp^*_3(g)$	+809.6	+418.3
$17.25Al_4Cp^*_4(g) \longrightarrow 46Al(s) + 23AlCp^*_3(g)$	-122.7	-55.69
$17.25Al_4Cp^*_4(g) \rightleftharpoons 69AlCp^*(g)$	+/-144.0	+/-479.0
$Al_4Cp^*_4(g) + 6AlCp^*\ (g) \longrightarrow Al_8Cp^*_4(g) + 2AlCp^*_3(g)$	+50.03	
$Al_{50}Cp_{12}(g) + 19AlCp_3(g) \longrightarrow 46Al(s) + 23AlCp_3(g)$	-822.0	-582.2
$17.25Al_4Cp_4\ (g) \longrightarrow Al_{50}Cp_{12}(g) + 19AlCp_3(g)$	+163.7	-1.195
$17.25Al_4Cp_4(g) \longrightarrow 46Al(s) + 23AlCp_3(g)$	-658.3	-583.4
$17.25Al_4Cp_4(g) \rightleftharpoons 69AlCp(g)$	+/-232.9	+/-638.6
$Al_4Cp_4(g) + 6AlCp\ (g) \longrightarrow Al_8Cp_4\ (g) + 2AlCp_3(g)$	+15.45	

reactions that take the tetramers to the corresponding Al_8 and $AlCp_3$ compounds are positive for both Cp and Cp* ligands. These reactions are not shown in Figure 6.11 or previous work (Ref. 57), but they provide further evidence that if one considers the larger clusters to be barrier states to metallization, then they provide a positive energy barrier for both Cp and Cp* based compounds.

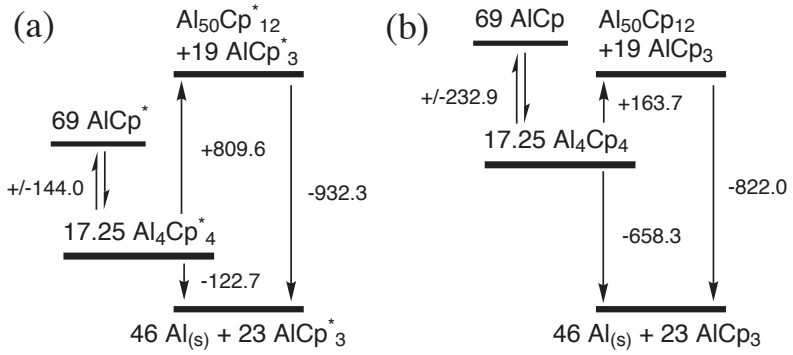

FIG. 6.11. Enthalpies of reaction in kcal/mol for the proposed[57] barrier mechanism with (a) Cp* and (b) Cp ligands.

In our work we observe significant relaxation of the ligands in the $Al_{50}Cp_{12}$ complex, and it is possible that this is the origin of our disagreement with the previous report, which gives no information on the calculated structure or thermodynamics of $Al_{50}Cp_{12}$. As a check, we have also calculated enthalpies of formation using BP86 with an SVP basis set, similar to the methodology used in previous work.[57] The calculated enthalpies of formation for AlCp and AlCp* with this method are 2.63 and -79.6 kcal/mol respectively; these differ significantly from G2 and literature values as well as our method, and this may also account for disagreement with previous calculations. The computational scheme used here shows good agreement with G2 results for smaller clusters, and we expect that the heats of formation will generally be accurate if the cluster geometry is correct. The large idealized reactions in this diagram certainly amplify small changes in the calculated enthalpies of formation

of the materials, but overall the results calculated with our computational methodology do not support the hypothesis of the Al_{50} compound serving as a barrier to immediate metallization of the tetramer. The differences between the Cp and Cp^* complexes may instead simply arise from the stabilizing effect of the Cp^* methyl groups, which provide a significantly larger steric hindrance in condensed phase environments. We note that in many cases (see Table 6.7), the Cp variations of a given structure have larger intrinsic bond strengths than those with Cp^*. The free energy barriers to decomposition of the Al_4Cp_4 and $Al_4Cp^*_4$ tetramers into monomeric units are both calculated to be negative at ambient conditions, but experimentally the former (unmethylated) decomposes spontaneously and the latter (methylated) is observed up to temperatures beyond 100° C. This suggests that the steric effects, rather than the innate binding energy of the cluster, are playing a key role in the decomposition. This is consistent with the idea that AlCp or $AlCp^*$ removal is the initial decomposition step and that steric hindrance from the ligand is an important limiting mechanism for monomer detachment. We also note that the tetramer $Al_4(C_5Me_4H)_4$, in which each Cp ligand has four methyl groups instead of five as in Cp^*, has also been experimentally observed in solid state form, further suggesting the necessity of strong steric hindrance for cluster stability.[53]

6.4 Combustion Properties

To evaluate the potential for using these clusters as novel fuel additives or energetic materials, we use the above thermodynamic data to estimate some typical energetic properties. In this section, we focus on two of the clusters in our study that have been successfully synthesized experimentally in small quantities, $Al_4Cp^*_4$ and $Al_{50}Cp^*_{12}$. The heat of combustion, ΔH_c (in kcal/g) for each cluster is calculated using Cheetah 5.0,[85] with the B3LYP heat of formation from Table 6.8 supplied as input. This value is then converted to a volumetric heat of combustion using the experimental density of the molecular crystal.[52,36]

TABLE 6.10. Heat of combustion, both by volume and by mass, for two aluminum organometallic clusters compared with solid Al and two standard energetic materials.

Component	ΔH_c (kcal/cm^3)	ΔH_c (kcal/g)	ρ (g/cc)
Al	19.99	7.40	2.701
PBX[a]	7.07	4.25	1.664
RDX	3.82	2.11	1.810
$Al_4Cp^*_4$	10.51	9.80	1.072
$Al_{50}Cp^*_{12}$	11.48	9.05	1.269

[a]The PBX compound here represents a simplified aluminized explosive mix of 64% RDX, 20% Al, and the remainder a combination of binder and plasticizer, by weight.

Volumetric heats of combustions for each cluster are shown in Table 6.10, along with values for metallic Al and two explosives, RDX and a representative aluminized explosive formulation denoted PBX. The latter is a mix of 64% RDX, 20% Al, and the remainder a combination of polymeric binder and plasticizers. Despite low densities, the volumetric heats of combustion of the organometallic materials are high, approaching 60% that of pure aluminum due to their high enthalpies of formation, strained aluminum cores, and surrounding hydrogen-rich ligands. This suggests that these materials are very promising as novel fuels or propellants in terms of their raw energy density, if they can be made sufficiently air and temperature stable. We note that a simple analysis of the heat of combustion ignores the differences in the decomposition kinetics of the organometallic aluminum complexes versus standard aluminum powders, which naturally will be very significant. If decomposition proceeds readily through the loss of surface $AlCp^*$ layers as discussed above, we expect that the exposed interior core would react on timescales far shorter than the diffusion-limited combustion of large aluminum particles.

We next consider the specific impulse I_{sp} of idealized formulations of oxidizers with aluminum-cyclopentadienyl compounds to evaluate their potential use in solid

TABLE 6.11. Specific impulse of several idealized fuel/oxidizer mixtures. Each formulation contains a solid fuel (either metallic Al or an Al-based cluster) and is approximately oxygen balanced using AP as an oxidizer.

Mix Ratio (%Vol)	I_{sp} (sec)
20 Al / 80 AP	246
20 $Al_4Cp_4^*$ / 80 AP	252
40 $Al_{50}Cp_{12}^*$ / 60 AP	266
20 Al / 70 AP / 10 HTPB	258
20 $Al_{50}Cp_{12}^*$ / 70 AP / 10 HTPB	260

rocket motors. The I_{sp} values given here represent the change in impulse per propellant mass, normalized with the gravitational constant so that the final units are in seconds. In all cases the oxidizer/organometallic mixture was optimized until the mixture was approximately oxygen balanced; the final compositions are show in Table 6.11. The value for a traditional ammonium perchlorate (AP) / aluminum mixture is 246 s, and the organometallic/AP mixtures fall slightly higher than this. A similar trend is observed in a formulation with the common hydroxyl-terminated polybutadiene (HTPB) polymeric binder, where the organometallic provides a comparable I_{sp} to an AP/Al mixture in this simple approximation. Thus, in terms of raw energy content, the organometallic/oxidizer formulations are calculated to provide similar or perhaps slightly superior I_{sp} values in solid rocket motors as compared to high-performance AP/Al mixtures. The significant expected differences in the decomposition kinetics and aluminum oxidation between the organometallics and bulk aluminum are ignored in this analysis; based on the cluster binding energies discussed above, these materials may decompose rapidly enough that the propellant surface area in the motor could be reduced. This might allow, for example, compact end-burner geometries with no central core through the propellant grain.

7. CARBOXYL-TERMINATED POLYMER COATINGS

7.1 Oligomer Geometries and Method Validation

The optimized geometries of perfluorotetradecanoic acid and its anion are shown in Figs. 7.1 and 7.2. We find that optimization of these long-chain oligomers results in a distorted backbone; the sp^3 hybridization of C is retained, but the dihedral is not preserved along the entire polymer chain. This flexibility is expected in linear polymers with backbones C_n, $n > 10$. For this reason, more simplified adsorption schemes are considered using shorter-chain alkanoic acids: formic acid, HCOOH, propanoic acid, CH_3CH_2COOH, and their anions, $HCOO^-$ and $CH_3CH_2COO^-$. Furthermore, the effect of functional group electronegativity is modeled with pentafluoro-propanoic acid, CF_3CF_2COOH, and its anion, $CF_3CF_2COO^-$. The optimized geometries of all three acids and their anions are given in Tables 7.1 and 7.2.

FIG. 7.1. Optimized geometry of perfluorotetradecanoic acid.

TABLE 7.1. Optimized geometries of (a) formic acid, (b) propanoic acid, and (c) pentafluoro-propanoic acid. Mulliken charges are shown for C and O.

(a)	(b)	(c)
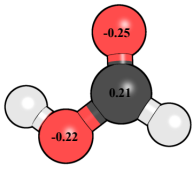	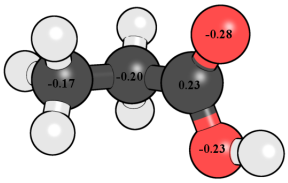	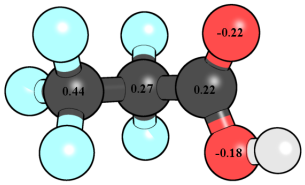

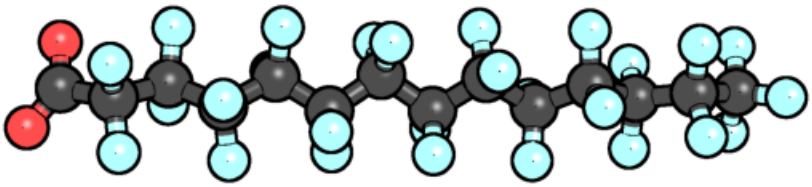

FIG. 7.2. Optimized geometry of perfluorotetradecanoate anion.

Adsorption energies for propionate and pentafluoro-propionate adsorbed in a bridge motif are used to validate the chosen functional/basis set combination. Table 7.3 shows the adsorption energy calculated with three different functionals (PBE, BLYP, and PADE) and two basis sets.[1] Details for the chosen basis sets are given in Table 4.1. We find that PADE, which is akin to LDA, overestimates the bond strengths relative to PBE. BLYP and the increased basis set lower E_a, but both of these methods are more computational costly. Hence, we employ PBE for all remaining calculations.

[1]We were not able to obtain BLYP results for pentafluoro-propionate because of convergence issues with the SCF energy.

TABLE 7.2. Optimized geometries of the (a) formate, (b) propionate, and (c) pentafluoro-propionate anions. Mulliken charges are shown for C and O.

(a)	(b)	(c)
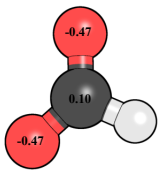	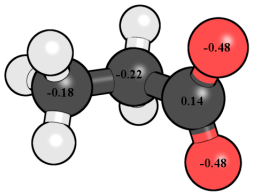	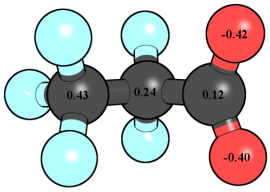

TABLE 7.3. Adsorption energies (in kcal/mol) of propionate and pentafluoro-propionate in a bridge motif on Al(111). Anion energies were calculated with a periodic Poisson solver (PBC) and with a multipole solver (NPBC).

		propionate		pentafluoro-propionate	
functional	basis set	PBC	NPBC	PBC	NPBC
PBE	BS-I	-15.35	-35.61	14.64	-1.31
	BS-II	-16.95	-37.24	10.53	-6.00
BLYP	BS-I	-23.76	-43.50	–	–
PADE	BS-I	-26.67	-46.99	0.12	-15.97

TABLE 7.4. Adsorption energies (in kcal/mol) of propionate anion in a bridge motif using different box sizes and Poisson solvers for the reference anion.

box size (Å^3)	Poisson *periodic*		Poisson *multipole*	
	PBE	PBE+vdw	PBE	PBE+vdw
$20 \times 20 \times 20$	-18.14	-26.77	-39.89	-48.52
$30 \times 30 \times 30$	-24.72	-33.35	-39.89	-48.52
$40 \times 40 \times 40$	-28.40	-37.03	-39.96	-48.58
$50 \times 50 \times 50$	-30.62	-39.25	-39.93	-48.55

A similar adsorption energy comparison is presented in Table 7.4, where DFT energies for the reference anion are calculated in different size simulation boxes. For each box size, the anionic energies are calculated with two different Poisson solvers for the electrostatics: *periodic* corresponds to periodic boundary conditions on both the simulation cell and the electrostatics solver, while the *multipole* solver is used with a non-periodic simulation box. We see that using a multipole solver for the anion decouples the electrostatics, and the DFT energy of an anion calculated in this way extrapolates to that of an infinite simulation box. This validates that adsorption energies calculated with this method are independent of box size.

7.2 Adsorption Geometries and Energies

To establish the preferred binding motif, we consider the three motifs proposed by Jouet *et al.* in their experimental work on nano-aluminum coated with perfluorotetradecanoic acid.[10] Specifically, we model monodentate and bidentate adsorption, in which either one or two O atoms binds directly to a single Al atom, and a bridge configuration in which two O atoms bind to separate Al atoms. We also investigate non-dissociative adsorption in which the hydroxyl (O-H) bond is preserved, and the carbonyl (C=O) oxygen binds to a single Al atom on the surface.

The first system we consider is a simple propanoic acid molecule chemisorbed onto Al(111). Monodentate, bidentate, and bridge motifs are shown in Figs. 7.3–7.5, while non-dissociative adsorption is presented in Figure 7.6. Mulliken charges are shown on each figure, while detailed geometrical data and adsorption energies are contained in Table 7.5. The angle, θ in Table 7.5 is defined as the angle between the Al surface plane and the line which passes though the terminal polymer carbon (see Figure 7.7). For the bridge motif, the acid molecule adsorbs onto two surface sites, and the line therefore bisects two Al atoms (Figure 7.7(a)). Optimized values of θ for the considered motifs fall in a narrow range from $\approx 65 - 73°$, while θ for

formic acid approaches 90°. This is evident from the optimized geometries shown in Figs. 7.8 and 7.9.

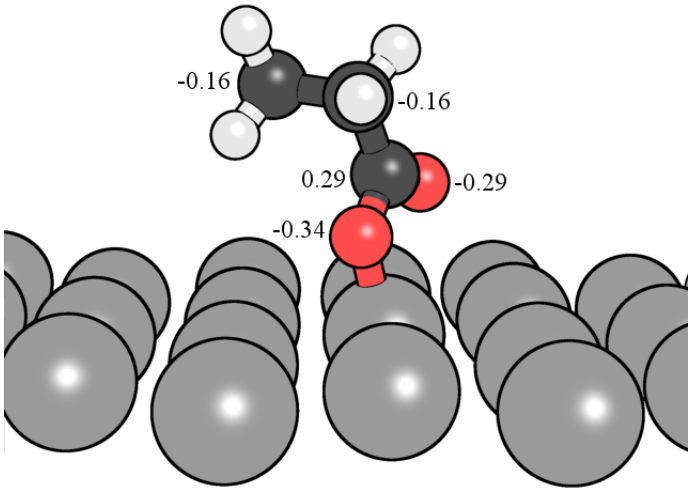

FIG. 7.3. Propionate anion adsorbed onto Al(111) in a monodentate motif. Mulliken partial charges are shown for O and C atoms.

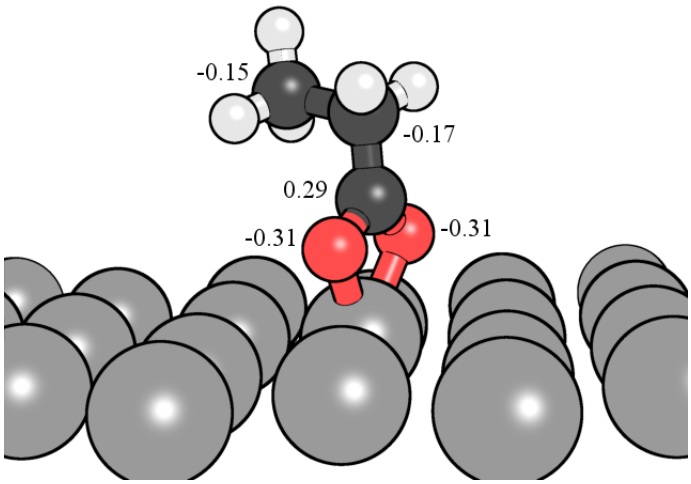

FIG. 7.4. Propionate anion adsorbed onto Al(111) in a bidentate motif. Mulliken partial charges are shown for O and C atoms.

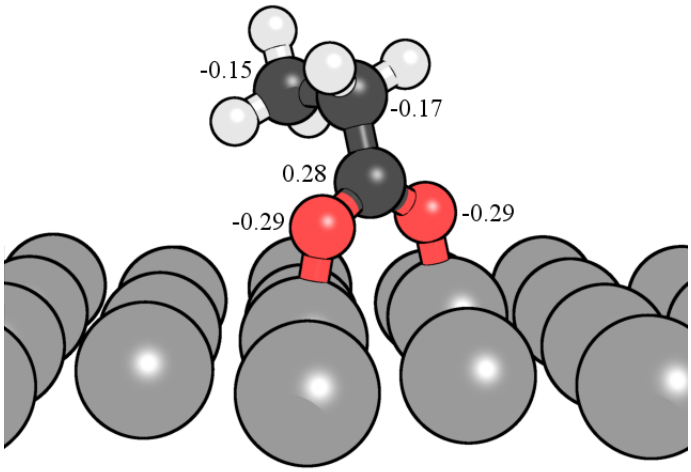

FIG. 7.5. Propionate anion adsorbed onto Al(111) in a bridge motif. Mulliken partial charges are shown for O and C atoms.

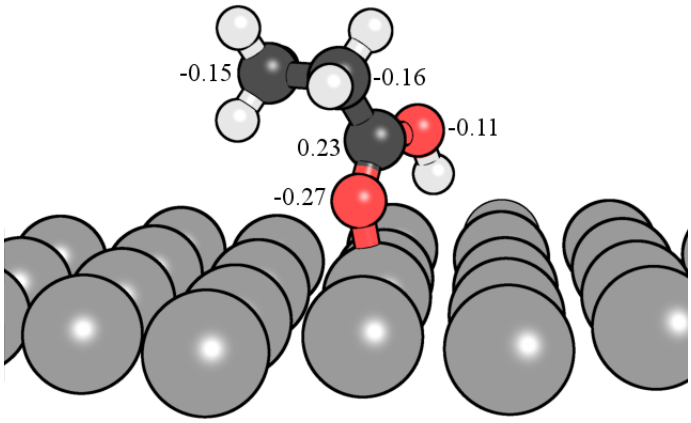

FIG. 7.6. Non-dissociative adsorption of propanoic acid onto Al(111). Mulliken partial charges are shown for O and C atoms.

TABLE 7.5. Relevant bond distances, angles, and adsorption energies (in kcal/mol) for the four unique adsorption motifs of propanoic acid on Al(111). vdw corrections are calculated using the DFT-D3 method, and E_a (298K) includes thermal corrections. All data are compared with formic acid in similar binding motifs (last two rows).

motif	Al-O (Å)	O-O (Å)	∠OCO	θ	E_a (PBE)	E_a (PBE+vdw)	E_a (298K)
monodentate	1.838	2.256	121.2	66.63	-16.25	–	–
bidentate	2.026	2.176	113.7	73.24	-14.83	–	–
bridge	1.883	2.253	121.7	64.96	-35.61	-44.24	-42.87
non-diss.	1.895	2.256	121.8	64.68	-32.35	-44.57	-44.02
bridge ($HCOO^-$)	1.916	2.271	125.3	87.46	-23.82	-24.90	-24.37
non-diss. (HCOOH)	1.996	2.277	125.7	84.93	-23.12	-29.06	-29.12

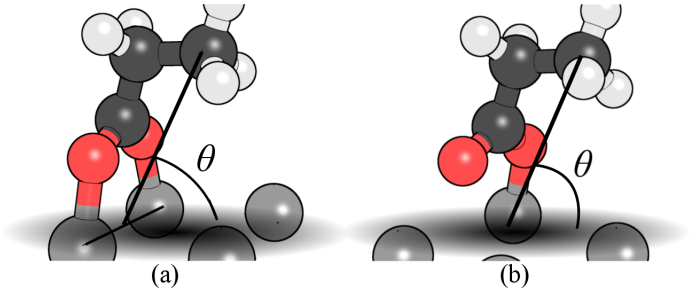

FIG. 7.7. Model for the definition of θ: in the bridge motif (a), the line through the terminal carbon of the propionate anion bisects two Al atoms on the surface, while motifs in which the anion binds to a single Al atom (monodentate, bidentate, and non-dissociative) are defined by (b).

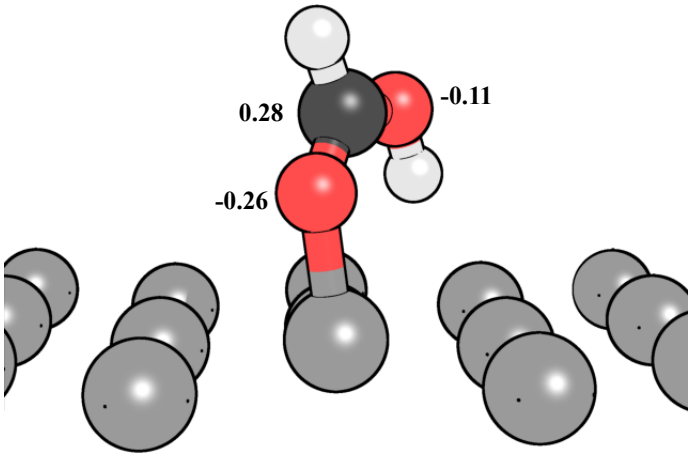

FIG. 7.8. Non-dissociative bonding of formic acid on Al(111). Mulliken partial charges are shown for O and C atoms.

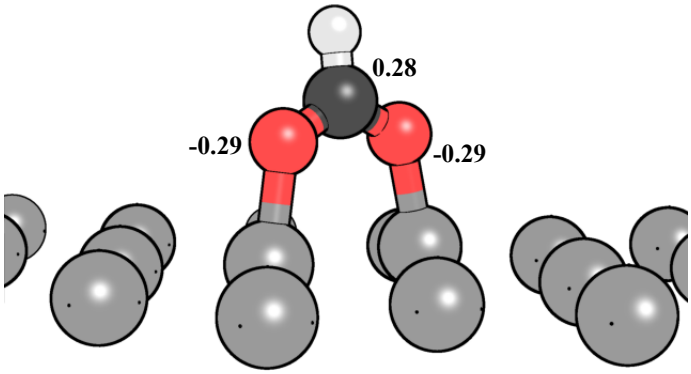

FIG. 7.9. Formate anion adsorbed onto Al(111) in a bridge motif. Mulliken partial charges are shown for O and C atoms.

Analysis of the optimized PBE geometries and calculation of their corresponding adsorption energies indicates that all possible binding motifs on Al(111) are energetically favorable (i.e., all have negative adsorption energies). Bidentate adsorption is the weakest at -14.83 kcal/mol, while the bridging arrangement is the strongest, with E_a=-35.61. Non-dissociative binding is comparable in strength, and these two motifs are further investigated with DFT-D3. Comparison of the geometry data given in Table 7.6 with that in Table 7.5 indicates that incorporating vdw corrections does not drive optimization of the adsorbed systems into different energy minima. Hence, we can confidently compare the energies of the two methods, and we observe that including vdw corrections lowers E_a by $\approx$ 10 kcal/mol.

With comparable E_a for the bridge and non-dissociative arrangements, we cannot argue from adsorption energies alone that one type of chemisorption will be favored over the other. A similar conclusion is made for formic acid, for which bonding in the non-dissociative arrangement is stronger than the bridge motif by only 5

TABLE 7.6. Relevant geometrical data for each adsorption motif on Al(111) optimized with PBE+vdw.

motif	Al-O (Å)	O-O (Å)	∠OCO	θ
bridge	1.886	2.252	121.5	65.40
non-dissociative	1.905	2.253	121.8	64.64
bridge (formate)	1.922	2.276	125.7	88.01
non-diss. (formic acid)	1.979	2.275	125.3	87.04

TABLE 7.7. Relevant bond distances, angles, and adsorption energies for the four adsorption motifs of propanoic acid on Al(100).

motif	Al-O (Å)	O-O (Å)	∠OCO	θ	E_a (kcal/mol)
monodentate	1.813	2.270	123.4	63.91	-3.23
bidentate	2.047	2.187	115.1	75.45	-5.09
bridge	1.899	2.262	122.9	78.28	-19.93
non-dissociative	1.935	2.259	122.4	64.62	-15.29

kcal/mol. We also find that thermal corrections to E_a are small for these alkanoic acids, reducing the total adsorption energy at 298 K by no more than 3.0%.

The next system we consider is propanoic acid chemisorbed onto Al(100). Monodentate, bidentate, and bridge motifs are shown in Figs. 7.10–7.12, while non-dissociative adsorption is presented in Figure 7.13. Again, detailed geometrical data and adsorption energies are contained in Table 7.7. On Al(100), the bridge motif is preferred by about 4.5 kcal/mol, while all binding arrangements are considerably weaker than on Al(111). The magnitudes of E_a for the monodentate and bidentate configurations (-3.23 and -5.09 kcal/mol, respectively) indicate very weak physisorption. Hence, chemisorption of carboxylate-terminated polymer anions is energetically preferred in a bridging motif, both on Al(111) and Al(100).

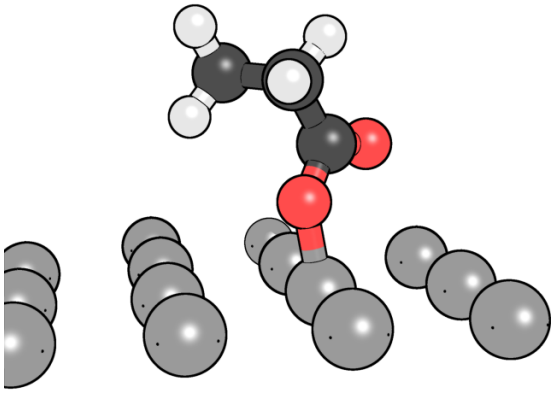

FIG. 7.10. Propionate anion adsorbed onto Al(100) in a monodentate motif.

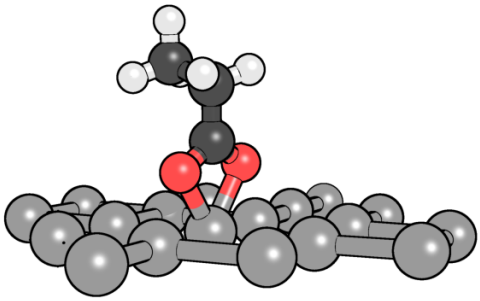

FIG. 7.11. Propionate anion adsorbed onto Al(100) in a bidentate motif.

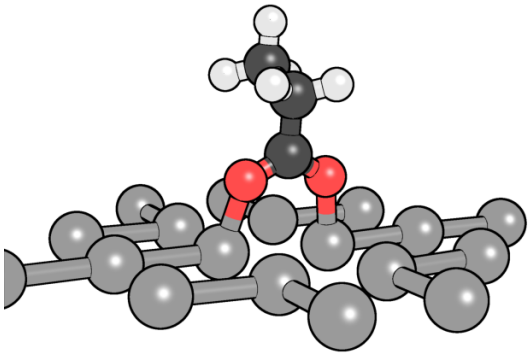

FIG. 7.12. Propionate anion adsorbed onto Al(100) in a bridge motif.

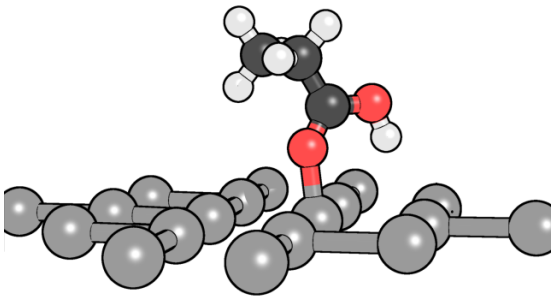

FIG. 7.13. Non-dissociative adsorption of propanoic acid onto Al(100).

7.3 Effect of Chain Length, Functional Group, Contact Angle, and Surface Coverage

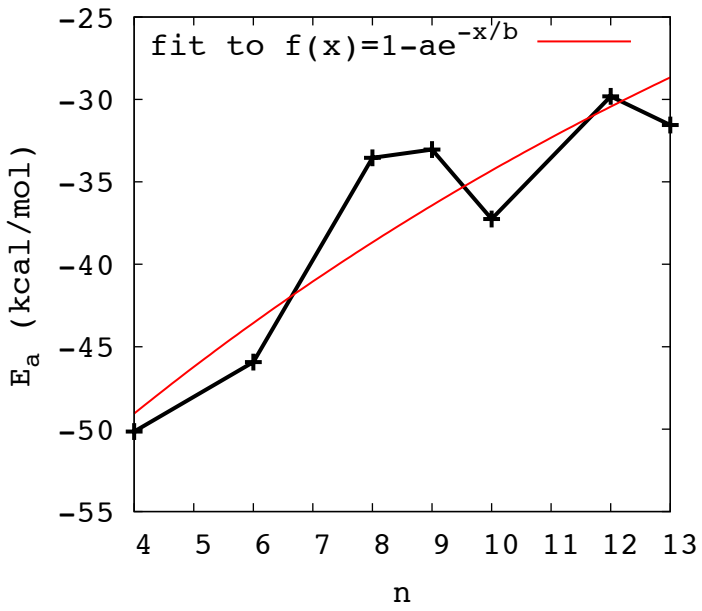

FIG. 7.14. Adsorption energy of carboxyl-terminated oligomers, $C_nH_{2n+1}COOH$, as a function of backbone length, n. Note that $n = 13$ corresponds to perfluorotetradecanoic acid. The data were fit to a function of exponential recovery $f(x) = 1 - ae^{-x/b}$ with fitting parameters $a = 63.1619$ and $b = 17.1983$.

For alkanoate oligomers, $C_nH_{2n+1}COO^-$, the effect of chain length n on E_a is shown in Figure 7.14. We observe that increasing the length of the backbone causes a slight reduction in E_a, and the trend can be described by fitting to a function for exponential recovery, $f(x) = 1 - ae^{-x/b}$. The fitting gives $b \approx 17$, with an RMS of 3.520. This indicates that E_a is essentially independent of n for very long alkanoic polymer chains (n≥17).

To assess the effect of functional group on E_a, bonding motifs for fluorinated chains were studied with pentafluoro-propanoic acid. The geometries and E_a's are

presented in Table 7.8. We see that functionalization with fluorine has a large influence on the adsorption energy. Specifically, adsorption of propionate in either a monodentate or bidentate configuration is no longer energetically preferred ($E_a > 0$). Clearly, bridge bonding of the anion will be energetically preferred, but E_a for pentafluoro-propionate (-11.03 kcal/mol) is not as strong as that for propionate (-44.24 kcal/mol) or formate (-24.90 kcal/mol). Hence, the repulsive effects of the fluorine functional groups actually weakens adsorption of the COO^- moiety on the surface. Furthermore, thermal corrections are quite large for both the bridge and non-dissociative motifs, reducing E_a at 298 K by 36.5% and 8.6%, respectively. This is because the C-F modes are shifted to lower frequencies relative to the C-H modes in standard alkanes; subsequently, more of these modes contribute to the vibrational partition function at room temperature.

Adsorption energy is also a function of contact angle, θ. We see from Figs. 7.15 and 7.16 that the optimal contact angles for propionate and pentafluoro-propionate adsorbed in bridging configurations range from $65 - 85°$. This is consistent with Brown's observation that the adsorbed configuration of alkanoates should be symmetrical and that the carboxylate plane should make a high contact angle with, but not necessarily be perpendicular to the surface.[67,68] Variations in E_a with θ around the minimum of Figure 7.16 can be attributed to changes in the optimized structure of the adsorbate in its bound configuration versus its gas-phase geometry. This is evidenced by the blue curve in Figure 7.16, where E_{molecule} is replaced with the single-point energy of the adsorbate fixed in its bound position. Preventing the adsorbate molecule from relaxing removes the anomalous variations in E_a close to the minimum.

TABLE 7.8. Relevant bond distances, angles, and adsorption energies for the four unique adsorption motifs of pentafluoro-propanoic acid on Al(111). vdw corrections are calculated using the DFT-D3 method, and E_a (298K) includes thermal corrections.

motif	Al-O (Å)	O-O (Å)	∠ OCO	θ	E_a (PBE)	E_a (PBE+vdw)	E_a (298K)
monodentate	1.847	2.254	125.1	54.37	14.26	–	–
bidentate	2.112	2.210	119.6	59.64	21.69	–	–
bridge	1.913	2.265	126.1	63.42	-1.31	-11.03	-7.00
non-diss.	1.933	2.281	127.1	64.97	-23.19	-33.11	-30.26

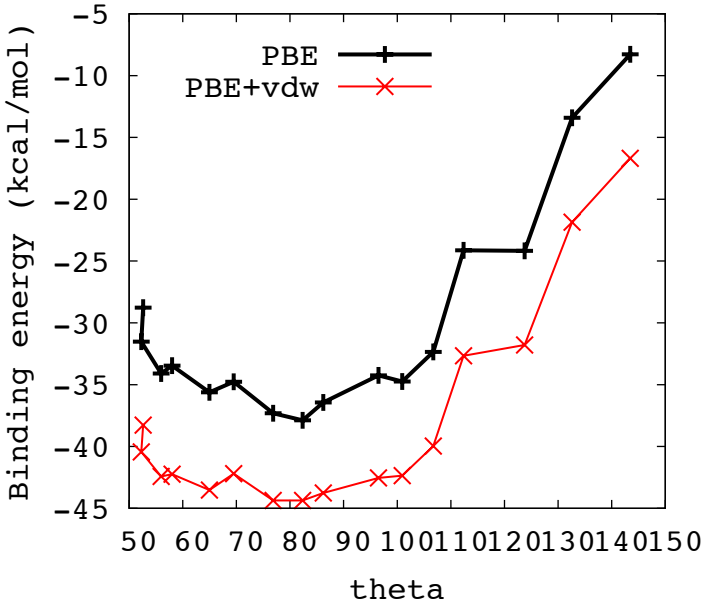

FIG. 7.15. Adsorption energy vs. theta from a scan of molecule-surface contact angle in the bridge adsorption motif. PBE+vdw energies were calculated at the PBE optimized geometries.

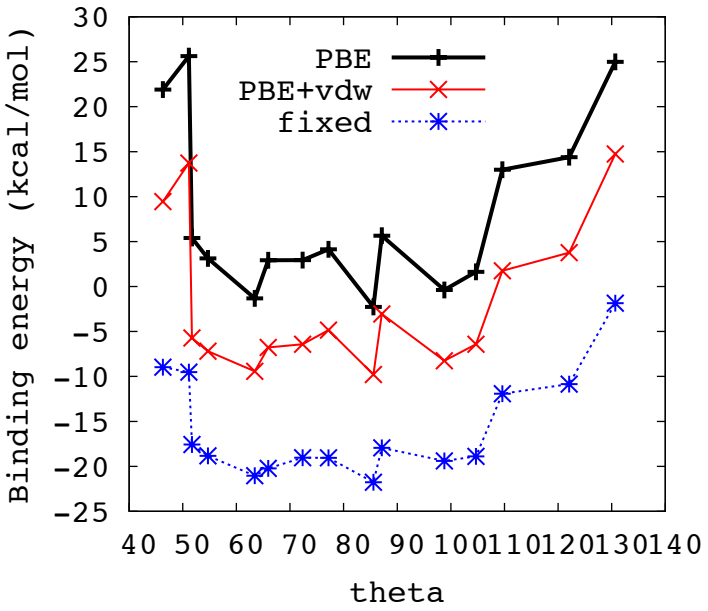

FIG. 7.16. Adsorption energy vs. theta from a scan of molecule-surface contact angle in the bridge adsorption motif of pentafluoro-propanoic acid. PBE+vdw energies were calculated at the PBE optimized geometries.

Figure 7.17 shows the trend in E_a with monolayer concentration. E_a decreases linearly as additional oligomers are added to available surface sites, and the data is well described by a linear trendline (RMS = 0.258). In our model, a fully passivated Al(111) surface (ML=1) would have 18 oligomer chains. From the fit in Figure 7.17, we estimate the adsorption energy for a full monolayer of propionate is -59.03 kcal/mol. However, this estimate does not take into account changes in chain geometry or contact angle that may occur at larger surface coverages. These will be especially important for highly-dispersive polymers with large electrostatic or vdw forces between chains.

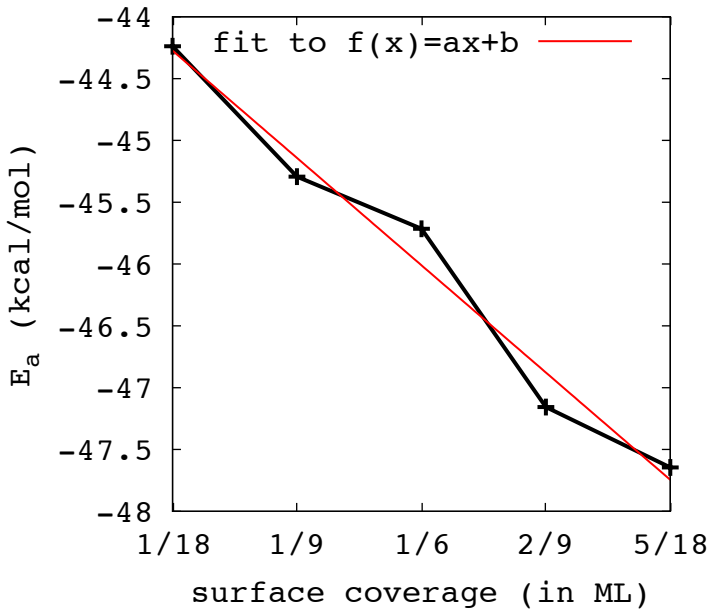

FIG. 7.17. Adsorption energy of a propionate monolayer on Al(111) for different surface coverages, in terms of monolayers (MLs). The data were fit to a linear trendline $f(x) = ax + b$ with fitting parameters $a = -15.6204$ and $b = -43.4062$.

7.4 Vibrational Analysis

In this section, we present vibrational analysis data for each alkanoic acid molecule and its anion, both in the gas phase and in their respective binding configurations. Table 7.9 contains frequencies for the ν(OH) and ν(CO) stretching modes of the COOH moiety. cp2k frequencies for the isolated molecules are compared to those calculated with Gaussian09, and percent differences between the two are only 2.5−4.0%. For every oligomer—regardless of chain length or functional group—the frequencies of both modes are reduced when bound to Al(111). Table 7.10 contains frequencies for the symmetric, ν_s(OCO) and asymmetric, ν_a(OCO) stretching modes of COO^-. Again, the cp2k and Gaussian09 frequencies agree well, with percent differences of

TABLE 7.9. Vibrational mode analysis of selected acid molecules using cp2k and Gaussian09. All frequencies are reported in cm^{-1}. Each molecule is analyzed in its gas phase, as well as in its adsorbed configuration on Al(111).

molecule/motif	ν(OH)			ν(CO)		
	cp2k	G09	Ref.	cp2k	G09	Ref.
formic acid	3613	3717		1767	1820	
HCOOH/Al(111)	3311			1602		
propanoic acid	3887	3739	3817[a]	1755	1815	1868[a]
CH_3CH_2COOH/Al(111)	3328			1554		
pentafluoro-propanoic acid	3632	3731		1797	1859	
CF_3CF_2COOH/Al(111)	3193			1633		
perfluorotetradecanoic acid	3638	3746	3076[b]	1826	1874	1754[b]

[a]Reference 103.
[b]Reference 10.

$0.5 - 4.0\%$. The frequency trends for bound oligomers, however, are different for the COO^- moieties. Specifically, we find that ν_a(OCO) is uniformly reduced for bound oligomers of all lengths, but ν_s(OCO) is decreased for $HCOO^-$/Al(111) and increased for the $CH_3CH_2COO^-$/Al(111) and $CF_3CF_2COO^-$/Al(111) systems. We note that the frequency trends in Tables 7.9 and 7.10 for alkanoates adsorbed on Al(111) are different from those on alumina; for example, on amorphous Al_2O_3 thin films, ν_a(OCO) is independent of chain length, while ν_s(OCO) decreases for longer oligomers.[68] Hence, we suspect that absorption of atomic C, O or H into adjacent interstitial sites—as would occur during thermal decomposition—will affect the experimental IR data.

In the previous sections, we calculated E_a for three different motifs: monodentate, bridging, and bidentate. Crowell noted that the adsorption configuration can be determined experimentally by measuring the frequency splitting between the symmetric and asymmetric carbonyl stretching modes.[63,64] The approximate magnitude of these splittings is given in Table 7.11. The frequency splittings from our work are

TABLE 7.10. Vibrational mode analysis of selected anions using cp2k and Gaussian09. All frequencies are reported in cm^{-1}. Each molecule is analyzed in its gas phase, as well as in a bridging configuration on Al(111).

molecule/motif	ν_s(OCO)			ν_a(OCO)			ν_a(OCO)−ν_s(OCO)		
	cp2k	G09	Ref.	cp2k	G09	Ref.	cp2k	G09	Ref.
formate anion	1317	1343	1352[a]	1665	1689	1584[a]	348	346	232
			1366[b]			1613[b]			247
$HCOO^-$/Al(111)	1308		1380[a]	1474		1575[a]	166		195
propionate anion	1353	1345	1429[c]	1632	1669	1565[c]	279	324	136
$CH_3CH_2COO^-$/Al(111)	1400			1440			40		
pentafluoro-propionate anion	1323	1359		1720	1771		397	412	
$CF_3CF_2COO^-$/Al(111)	1438			1551			113		
perfluorotetradecanoate anion	1393	1372		1758	1828		365	456	
$C_{13}F_{27}COO^-$/Al(111)			1482[d]			1667[d]			185

[a]Reference 63.
[b]Referece 104.
[c]Reference 105.
[d]Reference 10.

TABLE 7.11. Approximate frequency splittings (in cm^{-1}) associated with different carboxylate, COO^- binding motifs.

motif	ν_a(OCO)$-\nu_s$(OCO)
monodentate	300
bridging	200
bidentate	80

in shown in the last three columns of Table 7.10. Splittings for the isolated molecules are overestimated relative to the experimental values, and we attribute this to solvent effects. The ν_a(OCO)$-\nu_s$(OCO) splittings for the bound systems are 166, 40, and 113 cm^{-1}, which agree modestly with the guidelines given in Table 7.11.

Lastly, we comment on our vibrational analysis of perfluorotetradecanoic acid and $C_{13}F_{27}COO^-$/Al(111) relative to that given by Jouet (Ref. 10). First, Jouet claims to detect ν(OH) stretches at 2920 and 3076 cm^{-1}, which are both well below our calculated values. For all alkanoic acids, we calculate ν(OH) to be 3600-3800 cm^{-1}. Considering previous observations for formic and acetic acids,[63–65] we propose that the IR features at 2920 and 3076 cm^{-1} (Ref. 10) were incorrectly assigned. Rather than being O-H stretches, these may actually be resulting from weak H-bonding between COOH groups on adjacent perfluorotetradecanoic acid molecules in solution.

Furthermore, Jouet's experimental ν_a(OCO)$-\nu_s$(OCO) splitting is 185 cm^{-1}, which he uses to argue bridge bonding of COO^- moieties on the Al particle surface. Our calculated E_a values for a shortened chain, $CF_3CF_2COO^-$/Al(111), do support bridge bonding as the energetically preferred motif. However, Jouet estimates the metallic core of the nanoparticles to be 5 nm in diameter, whereas the particle size with the highest number concentration is 67 nm. If those estimates are correct, the particles are coated with over 60 nm of polymer. This is clearly much larger than a single monolayer because the end-to-end length of $C_{13}F_{27}COOH$ is only

2 nm. Hence, only a very small concentration of polymer is actually chemisorbed onto the Al surface, while the majority is likely physisorbed as a covalent polymer network.

8. SUMMARY

This dissertation project has evaluated the potential performance of novel, molecular-scale additives for solid rocket motor propellant formulations. The materials of interest have included manganese oxides and aluminum clusters with protective organic layers. First-principles calculations were used to assess structure, thermodynamics, and energy content, with a particular focus on their possible role as rapidly combusting fuels.

Ground-state geometries and magnetic structures for all Mn_xO_y: $x = 2, 3, 4, y = 1, 2$ clusters were calculated and validated experimentally by comparison with the experimental photoelectron spectra (PES). Good agreement was observed between the ground-state VDEs of the lowest-energy cluster geometries and the prominent PES features, with no energy shift required to match the main spectral peaks. The addition of oxygen reduces the net magnetic moment and stabilizes different magnetic ground-states compared to Mn_3 and Mn_4. Calculations of transitions from the anion to excited states of the neutral show reasonable agreement with higher-order and secondary peaks in the structure. For all systems considered, only a single magnetic isomer appears to be observed in the experimental PES, though transitions to various isomags of this single isomer do appear to contribute significantly.

The calculated EAs range from 1.29–1.84 eV, as shown in Table 5.2. The EA for three of the four clusters does exceed that of the O atom (1.472 eV), but these are relatively low compared with the 4-6 eV EAs calculated for $Mn_xCl_y^-$ clusters[16] and the 3-5 eV EAs of common propellant oxidizers (see Table 3.1). This means that the MnO clusters presented here cannot be classified as traditional super-halogens. Furthermore, experimental synthesis of high oxygen-balanced clusters was unsuccessful. Hence, while MnO clusters possess spin-dependent properties that may be attractive in other magnetic applications, their use as solid propellant additives is limited.

We have studied a range of aluminum-cyclopentadienyl cluster compounds using density functional theory to determine their suitability for use as novel fuels or propellants. The structure and bonding of these clusters was studied in detail, and the organometallic Al-ligand bonds are generally 55-85 kcal/mol and are much stronger than Al-Al interactions. This suggests that thermal decomposition in these clusters will proceed via the loss of surface metal-ligand units, exposing the interior aluminum core. Free energy barriers for removal of these AlCp or $AlCp^*$ units are quite low for some of the experimentally observed clusters, indicating that steric effects from the ligand are playing a dominant role in the cluster stability. The energy density of the large clusters, as gauged by their volumetric heat of combustion, is calculated to be nearly 60% that of pure aluminum. These organometallic cluster systems may provide a route to extremely rapid aluminum combustion for use in new fuels and solid rocket propellants.

We have used DFT as implemented in cp2k to investigate the bonding and surface effects in aluminum nanoparticles covered with fluorinated carbon chains. Al particles were modeled with bare Al(111) and Al(100) surfaces. Surface passivation was studied by constructing small monolayers (1/18 ML) of fluorinated chains with different length backbones. The preferred bonding motif for the COOH moiety of a single alkanoate chain is a bridging configuration with both O atoms bound to separate Al surface sites. This is also the preferred motif on Al(100), but adsorption energies are weaker due to increased Al-Al interatomic distance on the surface. By calculating adsorption energies for four different motifs, it was found that non-dissociative bonding of both formic acid and propanoic acid is energetically favorable, though experimental work has established the relative ease of O-H bond scission on bare Al surfaces. Our results suggest that alkanoic oligomers will chemisorb on Al(111) and weakly physisorb on Al(100). Furthermore, adsorption energies are highly sensitive to the chemistry of the polymer functional groups. Substituting F for H along the C backbone weakens adsorption in every motif, and the bridge configuration is the only

energetically preferred ($E_a < 0$) scheme for pentafluoro-propionate. Thermal corrections derived from the adsorbate partition function suggest that E_a for fluorinated oligomers will be reduced by over 30% at 298 K.

Our calculated E_a values support the bridge bonding scheme proposed by Jouet.[10] We find that E_a varies slightly with chain length, and E_a vs. n data for chain lengths $n = 4, 6, 8, 9, 10, 12, 13$ is fit modestly by an equation for exponential recovery. The fitting parameter $n_{\text{sat}} \approx 17$ indicates that E_a is essentially independent of chain length for fatty acids with $n \geq 17$. The slight weakening of E_a for longer chains is counterbalanced by the increasing thermal stability, as determined in experimental studies of melting point and glass transition vs. chain length.[106] We further assert that the monolayers reported in previous works (Refs. 10, 34, 74) are most likely multilayer structures, with only a small fraction of COO^- moieties bound directly to Al surface sites. Additional polymer chains likely retain their COOH terminal groups and form an amorphous (possibility semi-crystalline) polymer shell around the bound monolayer. Hence, the thermal stability is likely influenced both by E_a and T_M (and T_g for semi-crystalline polymers), the latter of which will dominate for large surface coverages. T_M for perfluoro$-n-$alkanoic acids is higher than that of saturated $n-$alkanoic acids, and longer chains have enhanced thermal stability, viz. $T_M \propto n$.[106] This could explain why Jouet successfully passivated nano-sized Al particles with $C_nH_{2n+1}COOH$ having $n = 13$ but not $n = 8$ or 10.[10]

The proposed failure mechanism for carboxylate-terminated polymer coatings on Al nanoclusters will be melting of the polymer and eventual desorption of oligomer chains. At high polymer concentrations, we expect the coating to have a multilayer structure. Recall that surface coatings of formic and acetic acids have three characteristic temperatures: condensation around 120-130 K, acid desorption at 160-170 K, and destruction of the alkanoate layer between 500-700 K.[63,64] Perfluorotetradecanoic acid has a $T_g \approx 80°C$ and a $T_M \approx 135°C$.[106] Therefore, any perfluoro-polymer which is physisorbed onto the alkanoate monolayer will melt first, and the chemisorbed

layer will desorb at higher temperatures. This desorption process is consistent with TGA analysis of heated nano-Al coated with $C_{13}F_{27}COOH$, which revealed steady weight loss upon heating from 100°C until full destruction of the polymer coating by 400°C.[59]

The final contribution of this dissertation is an understanding of the molecular- and atomistic-level engineering design principles to consider when selecting new, high-performance solid propellant materials. Oxidizers must have high kinetic barriers and possess stable solid phases at room temperature. Oxidation potential, which is roughly correlated with electron affinity, should be maximized, while also taking into account the potential toxicity of combustion product gases. Passivating agents for nanoscale Al should have high thermal stability and strong interactions with the surface. Since thermal decomposition of nitrocellulose has an activation energy of 45 kcal/mol, the performance of passivating agents in aluminized composite propellants can be gauged by comparing surface bonding with this value. In this dissertation, we have therefore shown that Al-organometallic clusters are more thermally stable than DB formulations, with Al-ligand bonds on the order of 55-85 kcal/mol. Alkanoic acid polymers, on the other hand, adsorb onto Al(111) with energies of 10-45 kcal/mol. Even with their relatively weak surface interactions, long-chain fluoro-polymers can still serve as good passivation materials because of their elevated melting temperatures relative to standard fatty acid chains. As described in Chapters 1 and 2, smart propellant design is a complex process which involves understanding the physics and chemistry of a material across a long range of length scales. Hence, the engineering design guidelines presented in this dissertation are restricted to properties which can be studied effectively with first principles methods.

REFERENCES

[1] Committee on Materials Research for Defense After Next, Materials research to meet 21st century defense needs, Technical report, National Research Council, 2003.

[2] F. A. Warren, *Rocket Propellants*, (Reinhold Publishing Corporation, New York, 1958).

[3] J. Taylor, *Solid Propellent and Exothermic Compositions*, (Interscience Publishers, Inc., New York, 1959).

[4] K. Hartman and S. Morrow, Solid propellants, Technical report, Alliant Techsytems, 2001.

[5] I. Glassman, *Metal Combustion Processes*, (American Rocket Society Preprint, New York, 1959).

[6] I. Glassman, A. M. Mellor, H. F. Sullivan, and N. M. Laurendeau, AGARD Conference Proceedings **52**, 19 (1970).

[7] V. Vilyunov and V. Zarko, *Ignition of Solids*, (Elsevier Science Publishers, 1989).

[8] M. W. Beckstead, B. R. Newbold, and C. Waroquet, Proc. 37th JANNAF Combustion Meeting **1**, 492 (2000).

[9] M. W. Beckstead, A summary of aluminum combustion, Technical report, Brigham Young University, 2002.

[10] R. J. Jouet et al., Chem. Mater. **17**, 2987 (2005).

[11] P. W. M. Jacobs and H. M. Whitehead, Chemical Reviews **69**, 551 (1969).

[12] I. P. S. Kapoor, P. Srivastava, and G. Singh, Propellants Explosives Pyrotechnics **34**, 351 (2009).

[13] B. K. Rao and P. Jena, Materials Research Society Symposium Proceedings **800**, 265 (2003).

[14] Nist chemistry webbook, nist standard reference database number 69, June 2005.

[15] G. L. Gutsev and A. I. Boldyrev, Chem. Phys. **56**, 277 (1981).

[16] M. M. Wu et al., Angew. Chem. Int. Ed. **50**, 2568 (2011).

[17] S. N. Khanna, P. Jena, W.-J. Zheng, J. M. Nilles, and K. H. Bowen, Phys. Rev. B **69**, 144418 (2004).

[18] S. Paul and A. Misra, J. Mol. Structure: THEOCHEM **907**, 35 (2009).

[19] N. O. Jones et al., Phys. Rev. B **70**, 134422 (2004).

[20] S. K. Nayak and P. Jena, J. American Chemical Society **121**, 644 (1999).

[21] M. J. Han, T. Ozaki, and J. Yu, J. Chem. Phys. **23**, 034306 (2005).

[22] K. S. Williams et al., The Journal of Chemical Physics **136**, 134315 (2012).

[23] S. Nayak and P. Jena, Chemical Physics Letters **289**, 473 (1998).

[24] M. Qing-Min, X. Zun, L. Ying, and L. You-Cheng, Chin. Phys. Lett. **24**, 1908 (2007).

[25] M. Pederson, F. Reuse, and S. N. Khanna, Phys. Rev. B **58**, 5632 (1998).

[26] J. Mejía-López, A. H. Romero, M. E. Garcia, and J. L. Morán-López, Phys. Rev. B **78**, 134405 (2008).

[27] S. K. Nayak, B. K. Rao, and P. Jena, J. Phys.: Condens. Matter **10**, 10863 (1998).

[28] P. Bobadova-Parvanova, K. A. Jackson, S. Srinivas, and M. Horoi, J. Chem. Phys. **122**, 014310 (2005).

[29] J. Jellinek et al., Phys. Rev. B **74**, 153401 (2006).

[30] S. N. Khanna, B. Rao, P. Jena, and M. Knickelbein, Chemical Physics Letters **378**, 374 (2003).

[31] B. K. Rao and P. Jena, Phys. Rev. Lett. **89**, 185504 (2002).

[32] W. K. Lewis et al., J. Phys. Chem. C **114**, 6377 (2010).

[33] S. W. Chung et al., Langmuiur **25**, 8883 (2009).

[34] M. J. Meziani et al., ACS Appl. Mater. Interfaces **1**, 703 (2009).

[35] K. S. Williams and J. P. Hooper, The Journal of Physical Chemistry A **115**, 14100 (2011).

[36] J. Vollet, J. R. Hartig, and H. Schnöckel, Angewandte Chemie International Edition **43**, 3186 (2004).

[37] H. Schnöckel and H. Köhnlein, Polyhedron **21**, 489 (2002).

[38] C. Dohmeier, D. Loos, and H. Schnöckel, Angewandte Chemie International Edition in English **35**, 129 (1996).

[39] A. Schnepf and H. Schnöckel, Angewandte Chemie International Edition **41**, 3532 (2002).

[40] H. Schnöckel, Chemical Reviews **110**, 4125 (2010).

[41] J. M. O'Connor and C. P. Casey, Chemical Reviews **87**, 307 (1987).

[42] P. Jutzi, Chemical Reviews **86**, 983 (1986).

[43] P. Jutzi and N. Burford, Chemical Reviews **99**, 969 (1999).

[44] M. A. Beswick, J. S. Palmer, and D. S. Wright, Chemical Society Reviews **27**, 225 (1998).

[45] P. H. M. Budzelaar, J. J. Engelberts, and J. H. van Lenthe, Organometallics **22**, 1562 (2003).

[46] N. T. Anh, M. Elian, and R. Hoffmann, Journal of the American Chemical Society **100**, 110 (1978).

[47] R. Burgert and H. Schnöckel, Chemical Communications **18**, 2075 (2008).

[48] H. Schnöckel, Dalton Transactions **19**, 3131 (2005).

[49] D. Bono, J. Hartig, M. Huber, H. Schnöckel, and L. Jongh, Journal of Cluster Science **18**, 319 (2007).

[50] V. M. Rayón and G. Frenking, Chemistry - A European Journal **8**, 4693 (2002).

[51] G. Frenking et al., Coordination Chemistry Reviews **238-239**, 55 (2003).

[52] C. Dohmeier, C. Robl, M. Tacke, and H. Schnöckel, Angewandte Chemie International Edition in English **30**, 564 (1991).

[53] M. Huber and H. Schnöckel, Inorganica Chimica Acta **361**, 457 (2008).

[54] R. Ahlrichs, M. Ehrig, and H. Horn, Chemical Physics Letters **183**, 227 (1991).

[55] J. Gauss, U. Schneider, R. Ahlrichs, C. Dohmeier, and H. Schnöckel, Journal of the American Chemical Society **115**, 2402 (1993).

[56] F. Alary et al., Journal of the American Chemical Society **125**, 11051 (2003).

[57] M. Huber, P. Henke, and H. Schnöckel, Chemistry - A European Journal **15**, 12180 (2009).

[58] S. Jadhav, Central European Journal of Chemistry **9**, 369 (2011), 10.2478/s11532-011-0024-8.

[59] R. J. Jouet, J. R. Carney, R. H. Granholm, H. W. Sandusky, and A. D. Warren, Materials Science and Technology **22**, 422 (2006).

[60] Z. Ma and F. Zaera, Surface Science Reports **61**, 229 (2006).

[61] I. P. Batra and L. Kleinman, Journal of Electron Spectroscopy and Related Phenomena **33**, 175 (1984).

[62] J. R. Jr., R. Hance, and J. White, Surface Science **100**, 388 (1980).

[63] J. E. Crowell, J. G. Chen, and J. T. Yates, Journal of Chemical Physics **85**, 3111 (1986).

[64] J. Crowell, J. Chen, and J. J.T. Yates, Journal of Electron Spectroscopy and Related Phenomena **39**, 97 (1986).

[65] J. Chen, J. Crowell, and J. J.T. Yates, Surface Science **172**, 733 (1986).

[66] J. Zhong and J. B. Adams, Journal of Physical Chemistry C **111**, 7366 (2007).

[67] N. M. D. Brown, R. B. Floyd, and D. G. Walmsley, J. Chem. Soc., Faraday Trans. 2 **75**, 17 (1979).

[68] N. M. D. Brown, R. B. Floyd, and D. G. Walmsley, J. Chem. Soc., Faraday Trans. 2 **75**, 261 (1979).

[69] F. Boerio and S. Chen, Journal of Colloid and Interface Science **73**, 176 (1980).

[70] D. L. Allara and R. G. Nuzzo, Langmuir **1**, 45 (1985).

[71] D. L. Allara and R. G. Nuzzo, Langmuir **1**, 52 (1985).

[72] Y. T. Tao, Journal of the American Chemical Society **115**, 4350 (1993).

[73] M. S. Lim et al., Langmuir **23**, 2444 (2007).

[74] B. Dikici, S. W. Dean, M. L. Pantoya, V. I. Levitas, and R. J. Jouet, Energy Fuels **23**, 4231 (2009).

[75] P. Hohenberg and W. Kohn, Physical Review **136**, B864 (1964).

[76] W. Kohn and L. J. Sham, Physical Review **140**, A1133 (1965).

[77] J. P. Perdew, K. Burke, and M. Ernzerhof, Physical Review Letters **77**, 3865 (1996).

[78] J. P. Perdew, K. Burke, and M. Ernzerhof, Physical Review Letters **78**, 1396 (1997).

[79] Y. K. Zhang and W. T. Yang, Physical Review Letters **80**, 890 (1998).

[80] M. J. Frisch et al., Gaussian 09 Revision A.1, Gaussian Inc. Wallingford CT 2009.

[81] A. D. Becke, J. Chem. Phys. **98**, 5648 (1993).

[82] L. A. Curtiss, K. Raghavachari, G. W. Trucks, and J. A. Pople, The Journal of Chemical Physics **94**, 7221 (1991).

[83] S. Dapprich, I. Komromi, K. S. Byun, K. Morokuma, and M. J. Frisch, Journal of Molecular Structure (Theochem) , 1 (1999).

[84] A. K. Rappe, C. J. Casewit, K. S. Colwell, W. A. G. III, and W. M. Skiff, Journal of the American Chemical Society , 10024 (1992).

[85] S. Bastea et al., Cheetah 5 user's manual, Technical report, Lawrence Livermore National Lab, 2007.

[86] C. Mader, Detonation properties of condensed explosives computed using the becker-kistiakowsky-wilson equation of state, Technical Report LA-2900, Los Alamos National Laboratory, 1963.

[87] J. VandeVondele et al., Computer Physics Communications **167**, 103 (2005).

[88] S. Grimme, Journal of Computational Chemistry **27**, 1787 (2006).

[89] P. E. Blochl, The Journal of Chemical Physics **103**, 7422 (1995).

[90] L. Genovese, T. Deutsch, A. Neelov, S. Goedecker, and G. Beylkin, The Journal of Chemical Physics **125**, 074105 (2006).

[91] A. D. Becke, Phys. Rev. A **38**, 3098 (1988).

[92] C. Lee, W. Yang, and R. G. Parr, Phys. Rev. B **37**, 785 (1988).

[93] S. Goedecker, M. Teter, and J. Hutter, Phys. Rev. B **54**, 1703 (1996).

[94] A. Schaefer, C. Huber, and R. Ahlrichs, J. Chem. Phys. **100**, 5829 (1994).

[95] G. L. Gutsev, S. N. Khanna, and P. Jena, Phys. Rev. B **62**, 1604 (2000).

[96] A. Haaland et al., Organometallics **14**, 3116 (1995).

[97] K. K., R. Burgert, G. Stösser, and H. Schnöckel, European Journal of Mass Spectrometry **11**, 469 (2005).

[98] B. K. Rao and P. Jena, The Journal of Chemical Physics **111**, 1890 (1999).

[99] H. Schnöckel, A. Schnepf, R. L. Whetten, C. Schenk, and P. Henke, Z. Anorg. Allg. Chem. **637**, 15 (2011).

[100] S. Dapprich and G. Frenking, The Journal of Physical Chemistry **99**, 9352 (1995).

[101] O. Lopez-Acevedo, P. A. Clayborne, and H. Hakkinen, Phys. Rev. B **84**, 035434 (2011).

[102] P. Clayborne, O. Lopez-Acevedo, R. L. Whetten, H. Grönbeck, and H. Häkkinen, J. Chem. Phys. **135**, 094701 (2011).

[103] A. Vicente et al., Physical Chemistry Chemical Physics **11**, 5729 (2009).

[104] J. Donaldson, J. Knifton, and S. Ross, Spectrochimica Acta **20**, 847 (1964).

[105] E. Spinner, J. Chem. Soc. , 4217 (1964).

[106] M. Tsuji, T. Inoue, and O. Shibata, Colloids and Surfaces B: Biointerfaces **61**, 61 (2008).

[107] S. G. Lias et al., 1988.

[108] J. Frunzke, M. Lein, and G. Frenking, Organometallics **21**, 3351 (2002).

[109] J. A. M. Simões, Organometallic thermochemistry database, Located within the NIST Chemistry WebBook.

APPENDIX I

Isomers of Anionic Clusters

This appendix contains the optimized geometries for additional, higher-energy isomags of the anionic and neutral Mn_xO_y clusters presented in Chapter 5. The caption below each figure contains the cluster multiplicity and relative energy (relative to stoichiometrically-equivalent clusters presented in the body of Chapter 5.)

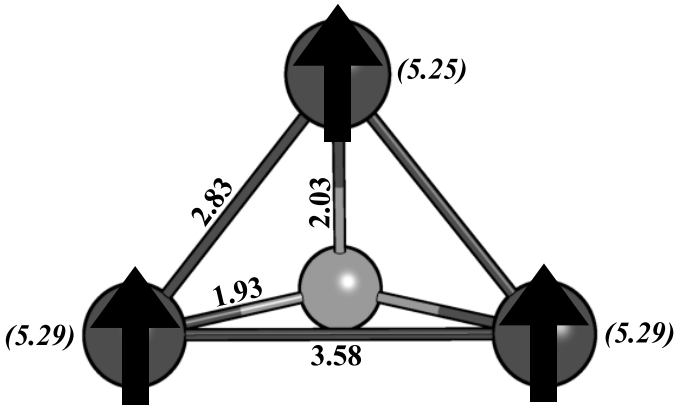

FIG. AI.1. Mn_3O^-, $M = 17$, $\Delta E = 0.16$ eV

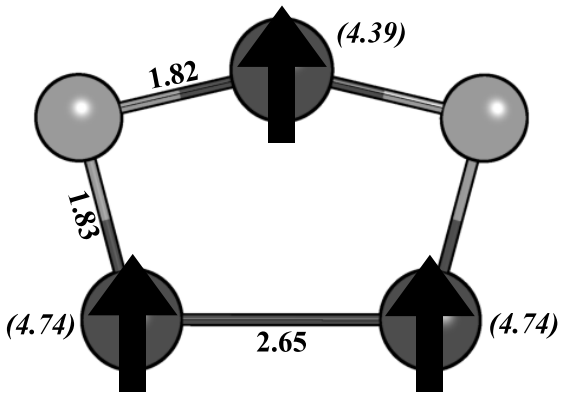

FIG. AI.2. $Mn_3O_2^-$, $M = 15$, $\Delta E = 0.36$ eV

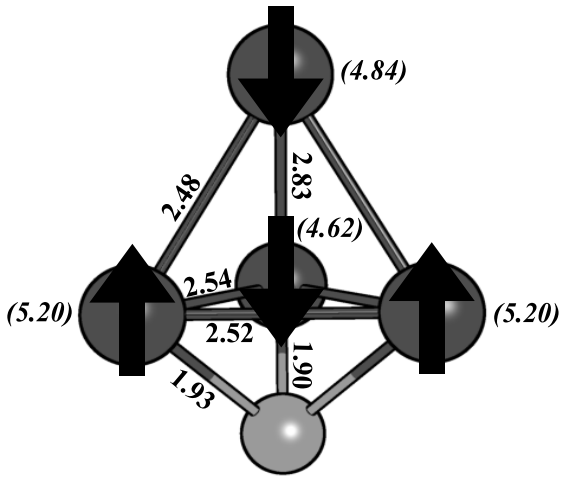

FIG. AI.3. Mn_4O^-, $M = 2$, $\Delta E = 0.25$ eV

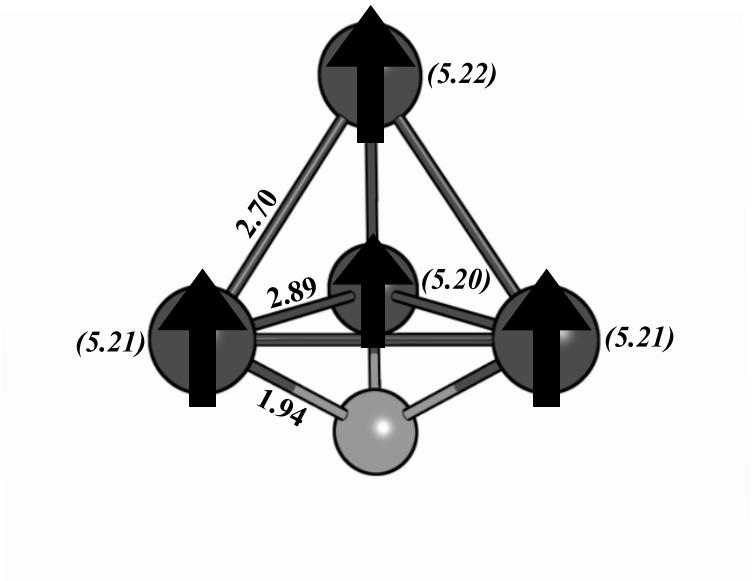

FIG. AI.4. Mn_4O^-, $M = 22$, $\Delta E = 0.43$ eV

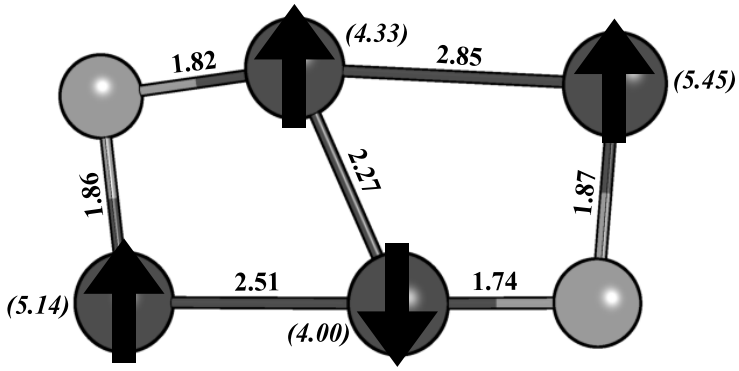

FIG. AI.5. $Mn_4O_2^-$, $M = 12$, $\Delta E = 0.63$ eV

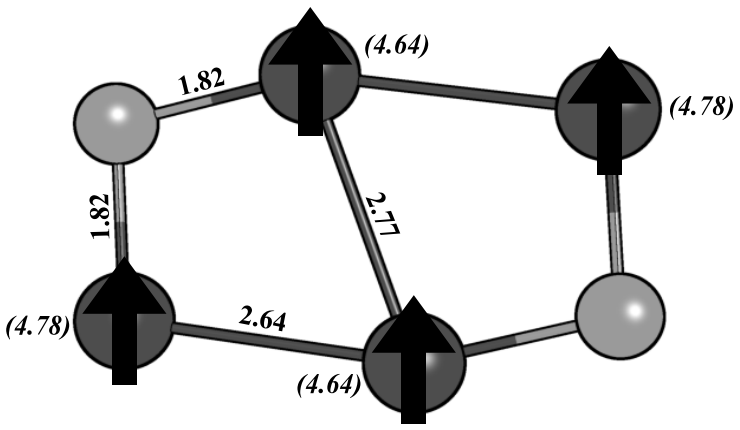

FIG. AI.6. $Mn_4O_2^-$, $M = 20$, $\Delta E = 1.20$ eV

Isomags of Neutral Clusters

Mn_3O

The neutral Mn_3O cluster corresponding to $M - 1 = 6$ has three non-degenerate isomags. The neutral Mn_3O cluster corresponding to $M + 1 = 8$ has two non-degenerate isomags.

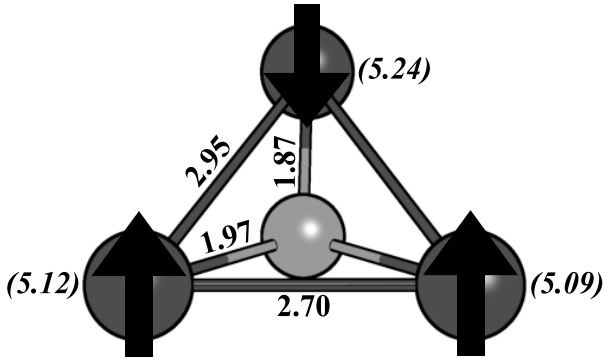

FIG. AI.7. Mn_3O, $M = 6$, $\Delta E = 0.00$ eV

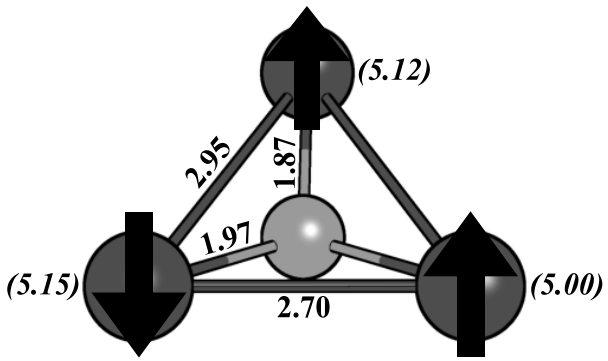

FIG. AI.8. Mn_3O, $M = 6$, $\Delta E = 0.06$ eV

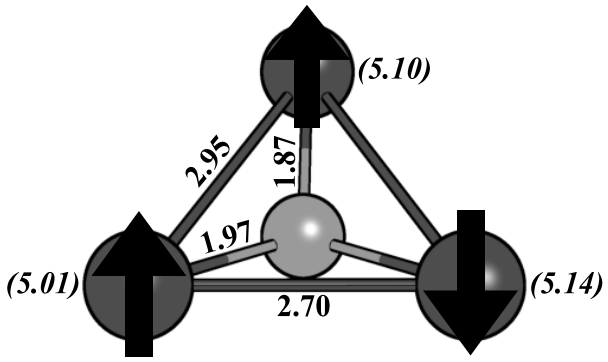

FIG. AI.9. Mn_3O, $M = 6$, $\Delta E = 0.07$ eV

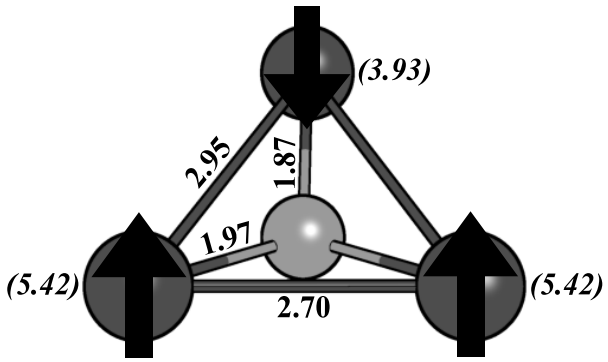

FIG. AI.10. Mn_3O, $M = 8$, $\Delta E = 0.00$ eV

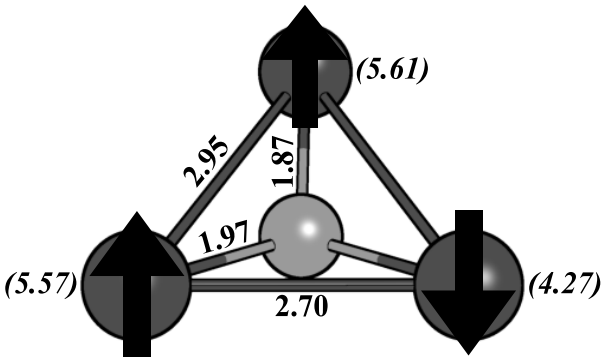

FIG. AI.11. Mn_3O, $M = 8$, $\Delta E = 0.09$ eV

Mn_3O_2

The neutral Mn_3O_2 cluster corresponding to $M - 1 = 4$ has two non-degenerate isomags. The neutral Mn_3O_2 cluster corresponding to $M + 1 = 6$ has three non-degenerate isomags.

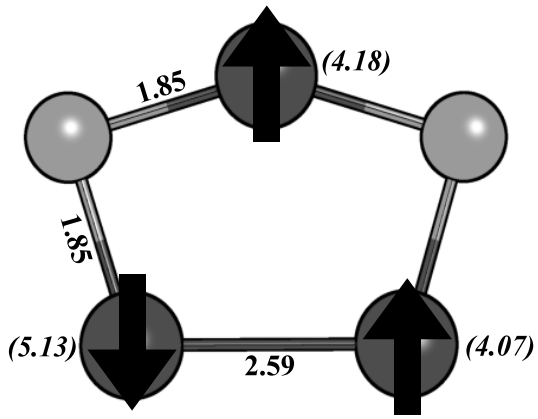

FIG. AI.12. Mn_3O_2, $M = 4$, $\Delta E = 0.00$ eV

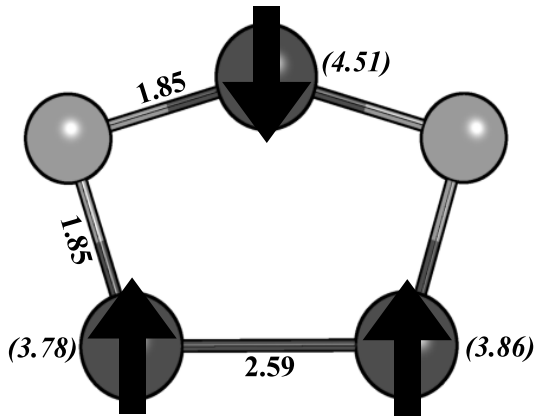

FIG. AI.13. Mn_3O_2, $M = 4$, $\Delta E = 0.22$ eV

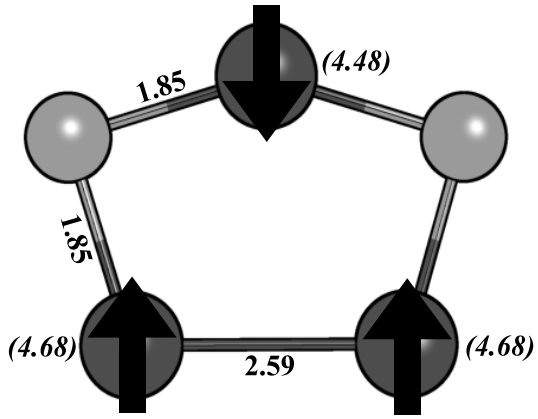

FIG. AI.14. Mn_3O_2, $M = 6$, $\Delta E = 0.00$ eV

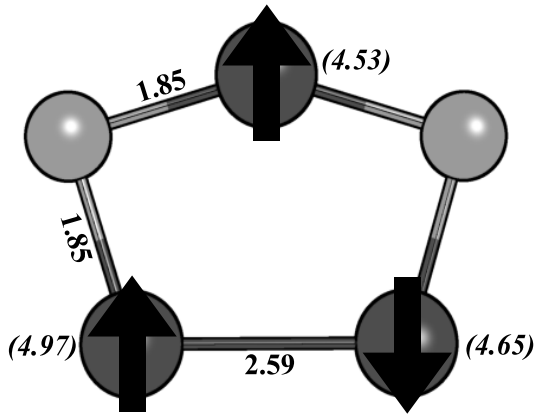

FIG. AI.15. Mn_3O_2, $M = 6$, $\Delta E = 0.21$ eV

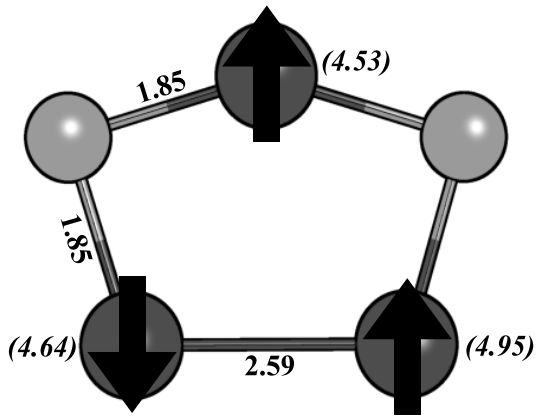

FIG. AI.16. Mn_3O_2, $M = 6$, $\Delta E = 0.26$ eV

Mn_4O

The neutral Mn_4O cluster corresponding to $M-1 = 11$ has three non-degenerate isomags. The neutral Mn_4O cluster corresponding to $M + 1 = 13$ has three non-degenerate isomags.

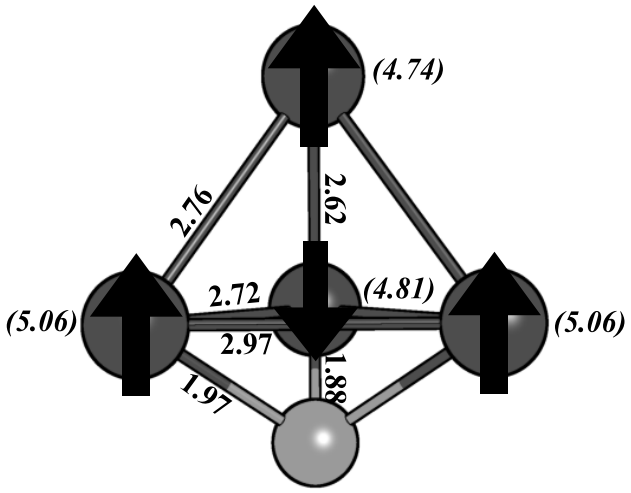

FIG. AI.17. Mn_4O, $M = 11$, $\Delta E = 0.00$ eV

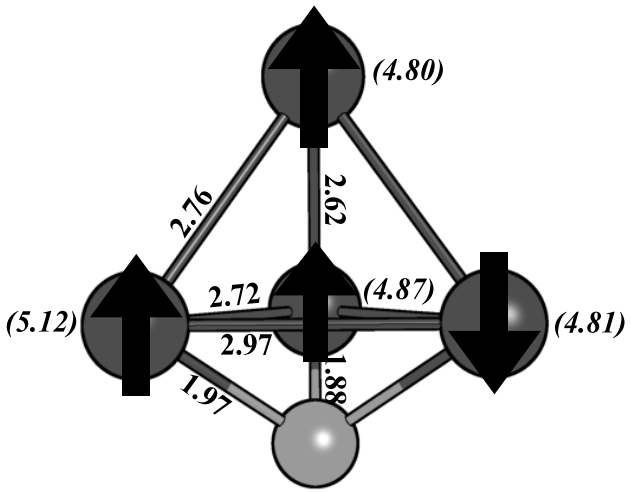

FIG. AI.18. Mn_4O, $M = 11$, $\Delta E = 0.20$ eV

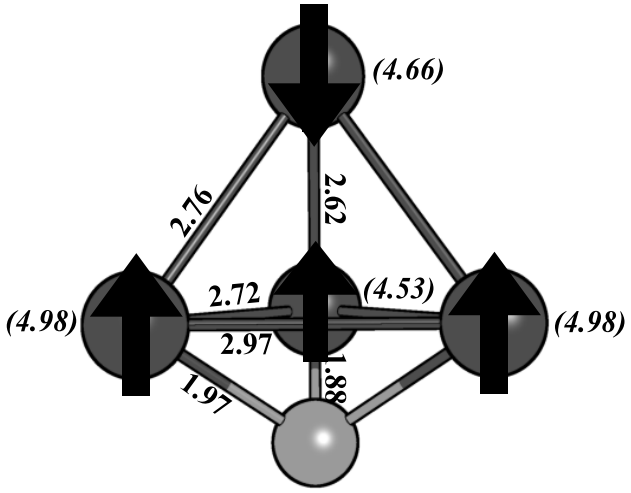

FIG. AI.19. Mn_4O, $M = 11$, $\Delta E = 0.35$ eV

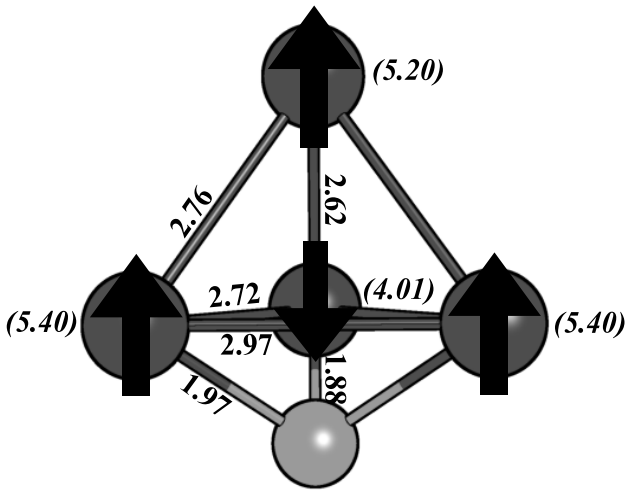

FIG. AI.20. Mn_4O, $M = 13$, $\Delta E = 0.00$ eV

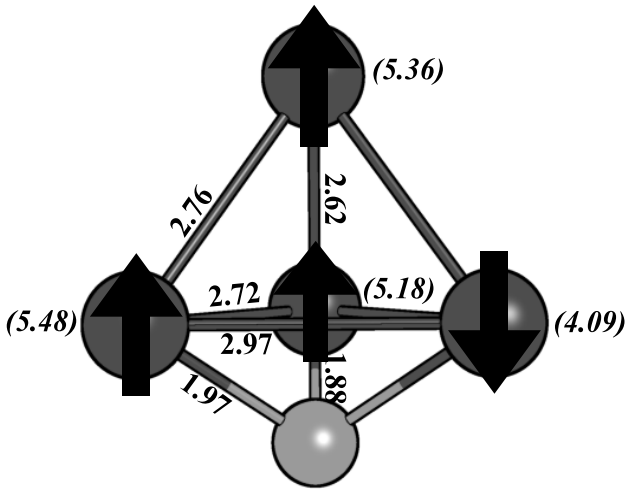

FIG. AI.21. Mn_4O, $M = 13$, $\Delta E = 0.21$ eV

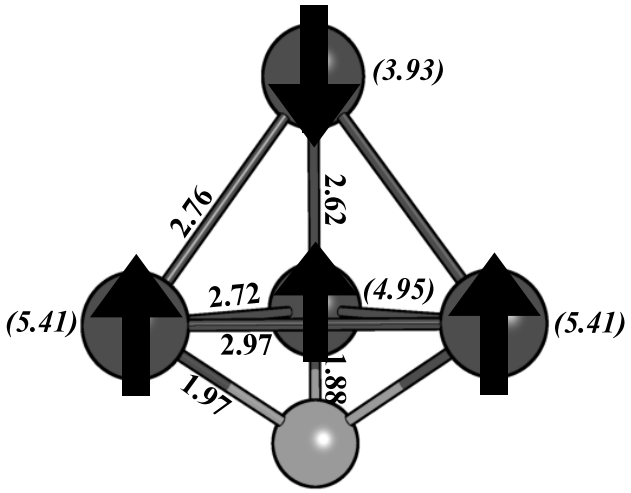

FIG. AI.22. Mn_4O, $M = 13$, $\Delta E = 0.50$ eV

Mn_4O_2

The neutral Mn_4O_2 cluster corresponding to $M-1=1$ has three non-degenerate isomags. The neutral Mn_4O_2 cluster corresponding to $M+1=3$ has four non-degenerate isomags.

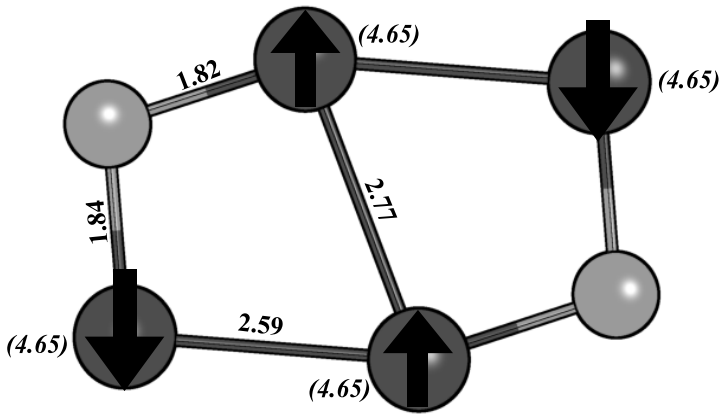

FIG. AI.23. Mn_4O_2, $M=1$, $\Delta E=0.00$ eV

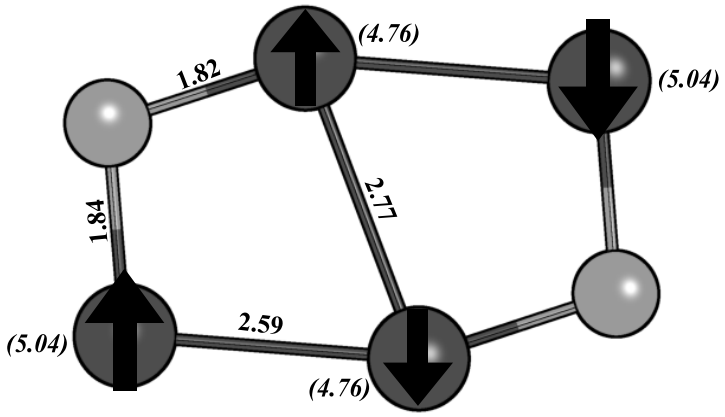

FIG. AI.24. Mn_4O_2, $M = 1$, $\Delta E = 0.20$ eV

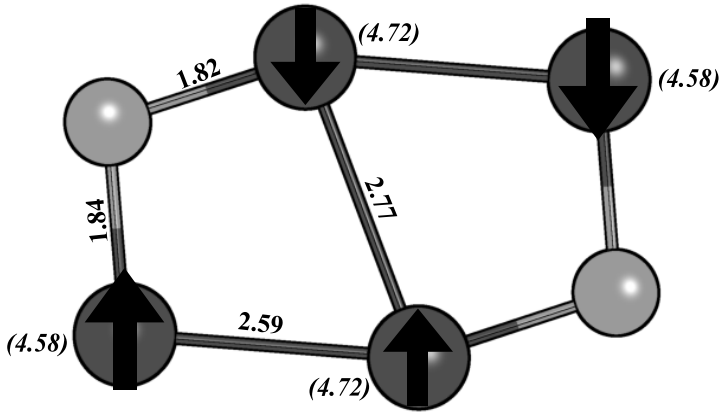

FIG. AI.25. Mn_4O_2, $M = 1$, $\Delta E = 0.44$ eV

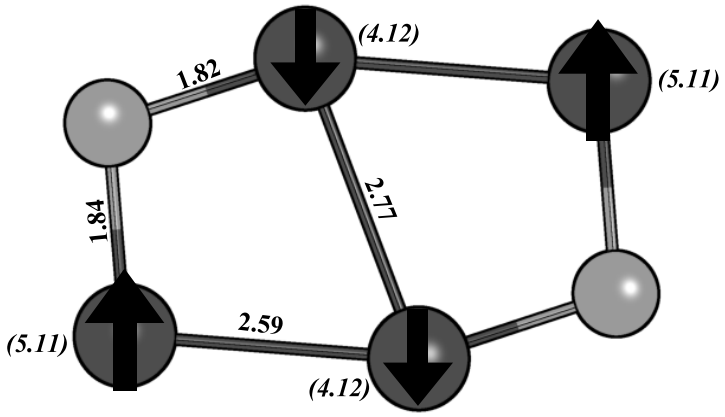

FIG. AI.26. Mn_4O_2, $M = 3$, $\Delta E = 0.00$ eV

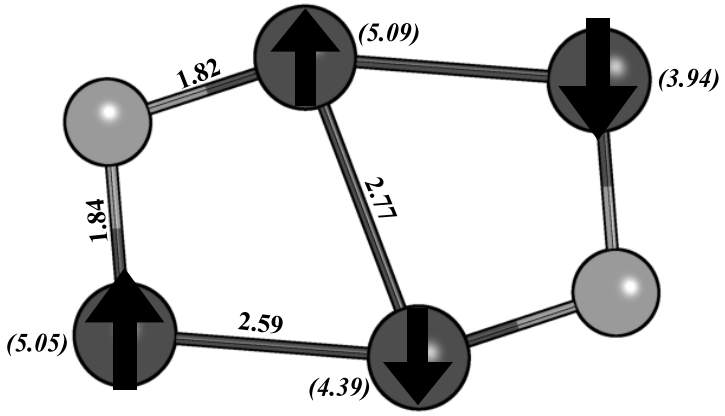

FIG. AI.27. Mn_4O_2, $M = 3$, $\Delta E = 0.23$ eV

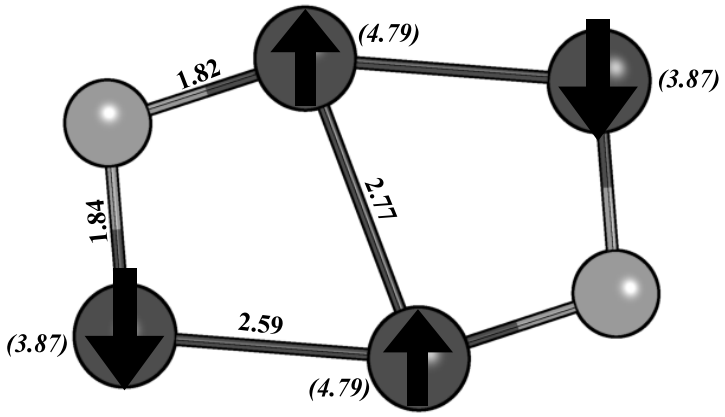

FIG. AI.28. Mn_4O_2, $M = 3$, $\Delta E = 0.25$ eV

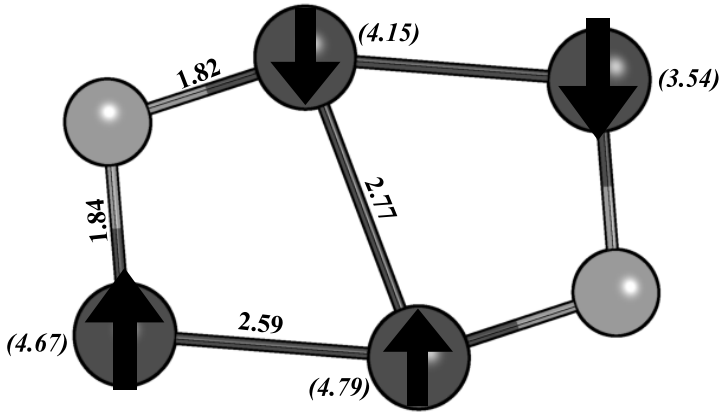

FIG. AI.29. Mn_4O_2, $M = 3$, $\Delta E = 0.49$ eV

APPENDIX II

Thermochemistry of Organometallics

Table AII.1 contains heats of formation (HOFs) for two organometallic, η-5 sandwich complexes: magnesium, $MgCp_2$, and ferrocene, $FeCp_2$. The HOFs calculated with first-principles approaches are compared with experimentally-measured values and reference data given in the Organometallic Thermochemistry Database.[109] The NIST HOF values were recalculated from different experimental studies based on a uniform set of reference data. The relative error between the theoretical and experimental values in Table AII.1 is 0.2–2.5 kJ/mol $\cdot$ atom, which give percent differences in the range of 3.4–19.8%. The reported HOFs of organometallics vary widely because combustion calorimetry of organometallics is not as accurate as that for pure organics due to the formation of non-stoichiometric metal oxides, whose reference heats of formation are unknown experimentally.[109]

TABLE AII.1. A comparison of calculated vs. experimental heats of formation for various organometallic sandwich complexes. The NIST values are recalculated on the basis of a single set of reference experimental data.

complex	ΔH_f^0 (kJ/mol)		
	theoretical	experimental	NIST values[a]
$Mg(Cp)_2$	125.5[b]	129.7±8.4[c]	137.5±4.4
			145.2±3.3
$Fe(Cp)_2$	292.5[d]	242.7±2.9[c]	242.4±2.5
			214.8±5.3
			228.6±4.6
			231.7±4.1

[a]Reference 14.
[b]Reference 50.
[c]Reference 107.
[d]Reference 108.